Mass spectroscopy and coincidence measurements of xenon, argon and mixed argon-water clusters

Nano and Molecular Systems Research Unit

Emilia Heikura

Master's thesis

Degree programme in physics

Faculty of Science
University of Oulu

August 2021

Acknowledgements

I would like to express my gratitude for my supervisors doctoral student Eetu Pelimanni and Academy researcher Minna Patanen for your guidance, experience, and knowledge. I highly value all the time and effort that you have given me concerning my thesis and studies. A special thanks goes to my family and friends for all the support for the times I felt lost during my studies.

Contents

1 Introduction

1.1 What are clusters and why to study them?

The definition of a cluster is not accurate, usually particles containing 2 to 10^7 atoms or molecules are regarded as clusters. It has been said that clusters even form a new state of matter between individual atoms or molecules and bulk. Clusters are referred as nanoparticles due their nanosize structure. One of the main reasons to study clusters is to figure out how quantum properties change as a function of cluster size. In this thesis clusters consisting of 10 to 100 units have been studied. Clusters of sizes from 2 to 10^3 are called microclusters. [1–3]

Clusters are found everywhere in the nature. They are found from atmosphere as well as from cells. To understand the cluster-related phenomena in the nature, it is important to understand the fundamental science related to clusters since properties of clusters differ from individual molecules and macroscopic matter. [1]

Clusters have importance also in the field of technology. Due to their special properties, clusters can be used as components in nanodevices. In some clusters special properties arise from their geometric and electronic structures. In the field of energy materials such as catalysts, solar cells, and thermoelectrics clusters have been studied due to their high surface to bulk ratio and favorable transport properties such as thermal and electric conductivity. [1, 4]

1.2 About clusters

Clusters can be classified by the substance from which they are formed. Homo-atomic clusters are formed from identical atoms only, whereas a homo-molecular cluster consists of only identical molecules. Clusters can be also hetero-atomic or hetero-molecular when they are formed from two or several different substances. In addition, clusters can be formed from mixtures of atoms and molecules. [1]

Clusters can be classified also by the bonds between the atoms or molecules in the cluster. They can be divided into metal, semiconductor, ionic, rare gas, and molecular clusters. Metal clusters are formed from metallic elements so the bonding between the atoms is metallic. Metallic clusters can be formed of one or several different elements. In metallic bonds the outermost valence electrons form a delocalized electronic cloud that binds the atoms [5]. Semiconductor clusters are formed from the same elements used in the solid semiconductors. However, semiconductive and metallic clusters are not necessarily conductive even if the bulk material is. This is due to the fact that especially in small clusters so-called band gap, the energy separation between the top of the valence band and the conduction band, varies as a function of the cluster size. In semiconductive bulk material the band gap between conduction and valence band is small, whereas in insulators the band gap is larger. In conductors the valence band and the conduction band overlap. Therefore, conductive materials lack a band gap. Bonds in semiconductive clusters are very strong covalent bonds. In ionic clusters the bonding is based on the fixed charges of the atoms. [1, 3, 6]

Rare gas clusters are formed from rare gases. Atoms in rare gas clusters are bound together due to the van der Waals dispersion forces acting between them. Dispersion forces arise from the electronic fluctuations in atoms. These fluctuations cause instantaneous dipoles that cause attractions between the atoms. Bonding in molecular clusters can be due to dipole-dipole interactions, van der Waals interactions or hydrogen bonds depending

on the molecule from which the cluster is formed. Dipole-dipole interaction arise from the permanent electronic dipoles in the molecule due to the electronegativity differences between the atoms in the molecule. A hydrogen bond is a bond between a hydrogen atom and an oxygen, nitrogen, or fluorine atom. A hydrogen bond is a special case of dipole-dipole bond due the strength of the bond. [1, 5]

Rare gas clusters are the most studied in the field of cluster science. This is due the fact that they are relatively easy to produce. In addition, the low reactivity of rare gases makes them safe substance to handle. Rare gas clusters are also suitable model systems for metal clusters due to the similar structures and changes in the structure as a function of cluster size. Geometric shell structures are observed in rare gas and metal clusters. [1, 7]

In this thesis the focus is on mass spectroscopy measurements of rare gas clusters and mixed argon-water clusters. Of rare gas clusters argon and xenon clusters were studied in detail. In measurements of mixed argon-water clusters, pure argon, protonated water and mixed argon-water fragments were seen. Ionization causes the protonation of water clusters. Xenon and argon clusters are homo-atomic clusters whereas water clusters are homo-molecular clusters. Protonated water clusters $[H_2O]_N H^+$ and mixed argon-water clusters $Ar_M[H_2O]_N^+$ are both hetero-molecular clusters. N and M indicate the number of atoms or molecules in the cluster.

The unique chemical and physical properties make water interesting substance to study. The importance of water is undisputed for biological processes. Therefore, water clusters are important in the biochemical processes in cells [8]. Water clusters are also studied in context of atmospheric processes such as acid rain formation or air pollution. These processes occur in the surface of water droplets. In addition, water clusters are studied as solvation models [1]. According to study of G. E. Douberly et al. protonated water clusters are used as a model to understand the proton binding in small molecules. Proton transfer is an important chemical process for example in acid-base reactions, electrochemistry [5] and biological reactions such as photosynthesis [9].

2 Theory

2.1 Rare gases

The elements which belong to rare gases or noble gases in periodic system are helium, neon, argon, krypton, xenon, and radon. These elements of Group 18 are colorless and odorless monoatomic gases at room temperature [10]. The combining factor in the structure of noble gases is the closed-shell electron structure. In closed shell electron structure, the valence atomic orbitals are completely occupied [5]. In this thesis noble gas clusters of argon and xenon are studied.

Electron configuration for argon is [Ar]= $1s^2 2s^2 2p^6 3s^2 3p^6$. For simplicity this can be written also as [Ar]=[Ne]$3s^2 3p^6$ where [Ne] describes the configuration of neon. For xenon the electron configuration is $[Xe] = [Ar]3d^{10}4s^2 4p^6 4d^{10}5s^2 5p^6$. This can be written also as [Xe]=$[Kr]4d^{10}5s^2 5p^6$, where [Kr] describes the configuration of krypton. Electron configurations describe how the electron orbitals are occupied in an atom. [5]

Although the valence orbitals in xenon and argon are fully occupied there is a difference between the ionization energy of the argon and xenon atoms [1]. Ionization energy describes the amount of energy needed to remove one electron off the outer shell [5]. The ionization energy for argon is 1520 kJ/mol and for xenon 1170 kJ/mol. Respectively these ionization energies in electron volts are 15.76 eV and 12.13 eV. The higher ionization energy in argon is due the fact that the outermost orbitals are much closer to the nucleus than the outermost orbitals in a xenon atom. The difference between the ionization energies and polarizability affects to the element's ability to form bonds. Therefore, xenon has the ability to form chemical compounds more easily than argon. However, the reactivity of rare gases is low compared to many other elements. [1, 5]

2.2 Bonding in clusters

Bonding in clusters affects the possible structures that a cluster can have. Also, the bonding between building blocks affects the fragmentation processes on clusters. To understand profoundly the bonding in clusters, group theory and molecular orbital theory are used to form bonding models. [1, 11, 12]

2.2.1 Group theory

Group theory is very explanatorily powerful theory used to simplify quantum mechanical calculations and to predict allowed spectroscopic transitions due selection rules. In addition, group theory is used to prognosticate which atomic orbitals can contribute to each molecular orbital in molecular orbital theory. Here we apply group theory to understand the structure and bonding in water molecules. [12]

In group theory, molecules are categorized in symmetry groups according to their symmetry. There are five different symmetry elements and corresponding symmetry operations according to the theory. Symmetry operation is an operation that leaves the object seemingly untouched. A symmetry element is a point, line or plane respect to which the symmetry operation is performed. These five symmetry operations are identity operation E, n-fold rotation C_n, reflection σ, inversion i and n-fold improper rotation S_n. Identity operation does nothing. The object itself is the symmetry element corresponding the identity operation. The n-fold rotation means a rotation around a symmetry axis, where the angle of rotation is $2\pi/n$. Reflections of the object can be found placing mirrors to the symmetry

axis. In inversion each point of the object is taken through the inversion center to the equal distance on the other side. The n-fold improper rotation operation first rotates the object. After rotation, a horizontal reflection is applied to system. Water molecule belongs to point group C_{2v}. The symmetry elements for the group C_{2v} are identity E, rotation C_2, reflection σ_v and reflection $\sigma_{v'}$. The symmetry elements of water molecule are presented in figure 1 to demonstrate the theory applied to molecule. [12]

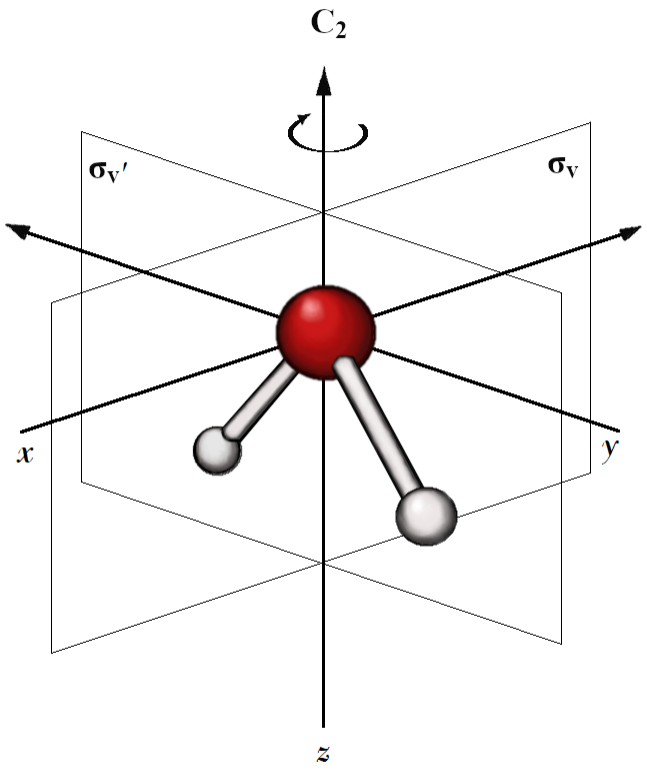

Figure 1: Figure shows the symmetry operations of water molecule. After the operation applied to molecule the result should seem untouched. In the figure C_2 symbolizes the 180° rotation through the z-axis. Symbols σ_v and $\sigma_{v'}$ describe the reflection of the water molecule in xz- and yz-planes respectively. [12, 13]

2.2.2 Molecular orbital theory

Molecular orbital theory is a model to describe the covalent bonding in molecules. Also, the lack of covalent bonding between rare gas atoms can be explained using molecular orbital theory. The theory arises from quantum mechanics and is based on superpositions of atomic orbitals. Molecular orbitals can be described as a linear combination of atomic orbitals. Mathematically this can be presented as in equation 1, where Ψ is the molecular orbital, χ_r is an atomic orbital and c_r is the corresponding coefficient for the atomic orbital χ_r. [12]

$$\Psi = \sum_r c_r \chi_r \tag{1}$$

Even though the summation in equation 1 extends over all the atomic orbitals in the atoms of the molecule, only orbitals with suitable symmetry and energy take part in formation of molecular orbitals. Applying group theory these atomic orbitals can be determined. When the superposition of atomic orbitals interferes constructively, a bonding molecular orbital $\Psi = c_A\chi_A + c_B\chi_B$ is formed. Correspondingly, when the superposition of atomic orbitals is destructive, the formed molecular orbital $\Psi = c_A\chi_A - c_B\chi_B$ is antibonding. Of formed molecular orbitals, the antibonding orbital is a higher-energy orbital, and the bonding orbital is a lower-energy orbital. Due to the antisymmetry between the molecular orbitals the antibonding orbital is more antibonding than the bonding orbital is bonding. The antisymmetry arises from the internuclear repulsion between the atoms. The repulsion pushes both the orbitals higher in energy. An example of molecular orbital energy level diagram is shown in figure 2. [12, 14]

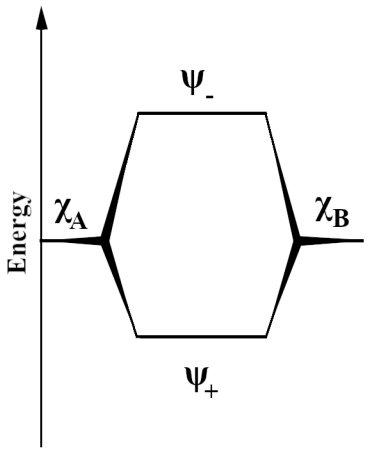

Figure 2: A simple example of molecular orbital energy level diagram is presented above. In the figure χ_A and χ_B describe the homonuclear atomic orbitals of the atoms A and B. Ψ_- is the antibonding orbital when Ψ_+ is the bonding orbital. Asymmetry between the bonding and antibonding orbitals can be seen clearly from the energy level diagram. [12]

Electrons occupy molecular orbitals similar way as they occupy atomic orbitals in atoms: a lower-energy orbital is occupied before a higher-energy orbital and each orbital can be occupied by two electrons of opposite spins. Bonding orbital as a lower-energy orbital is occupied before the higher-energy antibonding orbital. A simple value to describe the strength of the bond is called a bond order b. The bond order describes the net bonding in a diatomic molecule and it is presented in equation 2. Bond order depends only on the numbers of electrons in the bonding and antibonding orbitals. The greater the number of electrons in the bonding orbital the higher the bond order is. High bond order corresponds to higher strength in the bonding and usually to shorter bond lengths compared to a bond between same atoms but with a lower bond order. [12]

$$b = \frac{1}{2}(N - N^*) \tag{2}$$

In equation 2 N is the number of electrons in the bonding molecular orbitals and N^* is the number of atoms in the antibonding orbitals. [14]

2.2.3 Van der Waals bond

Due to the closed-shell electron structure the interactions between rare gas atoms are weak. The closed-shell electron structure of rare gas atoms causes the double occupation of each bonding and antibonding molecular orbitals. Bonding and antibonding orbitals in rare gases are formed when the outermost ns and np atomic orbitals overlap. For argon $n = 3$ and for xenon $n = 5$. Doubly occupied bonding and antibonding orbitals cancel each other out and therefore covalent bonding between rare gas atoms is not possible. The bonds between the atoms in neutral rare gas clusters are Van der Waals bonds. Van der Waals bonds are a result of London forces between atoms or molecules. London forces are also called dispersion forces. These forces arise due to the fluctuations in the electron cloud. These fluctuations cause temporary dipoles in the atoms. The attraction energy in Van der Waals interactions is described in the formula 3. [1]

$$V_L = -\left(\frac{C_6}{r^6} + \frac{C_8}{r^8} + \frac{C_{10}}{r^{10}} + ...\right) \tag{3}$$

In formula 3 r describes the distance between nuclei, and the terms C_n are constants. If the separation is longer than atomic diameter, as it is in case of rare gas clusters, the first term is dominant and therefore an approximation can be made [15]. The approximation is called London formula and is presented in equation 4 [1]. The equation for constant C_6 is shown in formula 5.

$$V_L = -\frac{C_6}{r^6} \tag{4}$$

$$C_6 = \frac{3}{2}\alpha_1\alpha_2\frac{I_1 I_2}{I_1 + I_2} \tag{5}$$

In formula 5 α_1 and α_2 describe atomic polarizabilities, I_1 and I_2 are the ionization energies for two interacting atoms. Atomic polarizability α is the ratio of induced dipole moment $\mathbf{p}$ and electric field $\mathbf{E}$ as presented in formula 6. The electric field in equation 6 is the field to induce the dipole moment in an atom. [14]

$$\alpha = \frac{\mathbf{p}}{\mathbf{E}} \tag{6}$$

If the interacting atoms are identical, ionization energy can be written as $I_1 = I_2 = I$. Also, the same applies for polarizability $\alpha_1 = \alpha_2 = \alpha$. Now the constant C_6 can be presented as in equation 7. [14]

$$C_6 = \frac{3}{4}\alpha^2 I \tag{7}$$

In addition to attractive interactions, there are also repulsions between the atoms. These repulsions arise from the electrostatic interactions between the electrons and protons of different atoms. Moreover, there is quantum mechanical Pauli repulsion between the electrons. Pauli repulsion causes a short-term interaction between interacting atoms and is a result of Pauli exclusion principle. According to exclusion principle the two electrons that occupy one orbital must have opposite spins. [5, 15]

Lennard-Jones potential is used to describe the potential between atoms that are attracted by London forces but have a repulsive interaction due to Pauli exclusion principle [1]. In Lennard-Jones potential function attractive London formula V_L and Pauli repulsion V_P can be written as presented in equations 8 and 9 [1, 16].

$$V_L = -\frac{C_6}{r^6} = -\frac{4\varepsilon\sigma^6}{r^6} = -\frac{2\varepsilon r_0^6}{r^6} \tag{8}$$

$$V_P = \frac{C_{12}}{r^{12}} = \frac{4\varepsilon\sigma^{12}}{r^{12}} = \frac{\varepsilon r_0^{12}}{r^{12}} \tag{9}$$

In equations 8 and 9 σ is the internuclear distance where potential goes to zero, r_0 is the distance at minimum potential and r is the internuclear distance [16]. The depth of the potential well or binding energy is described as ε. For the potential well ε relation $\varepsilon = k_B T$ can be written, where k_B is the Boltzmann's constant and T the temperature below which the dimers can be formed. By combining these potentials into one Lennard-Jones potential, an equation 10 is obtained. [1]

$$V_{ij}(r_{ij}) = \varepsilon \left(\left(\frac{r_0}{r_{ij}} \right)^{12} - 2 \cdot \left(\frac{r_0}{r_{ij}} \right)^{6} \right) \tag{10}$$

In formula 10, V_{ij} is the potential between atoms i and j and r_{ij} is the distance between the atoms. In the figure 3 an example of Lennard-Jones 6-12 potential curve is presented for argon and xenon dimer. Curves in the figure show how the repulsion and attraction between atoms change as a function of internuclear distance. [5]

Often in cluster experiments the neutral clusters are ionized for research purposes. Clusters studied in this thesis are ionized by electron bombardment to study positively charged clusters. The bonding in neutral clusters is different compared to charged rare gas clusters. In neutral rare gas dimer the bonding and antibonding molecular orbitals are doubly occupied $(\sigma_g)^2(\sigma_u^*)^2$ as was discussed before. However, if the cluster is singly charged the occupation in the molecular orbitals change. At the ionization threshold of the cluster, the electron removed from the cluster is removed from the antibonding molecular orbital σ_u. The removal of the electron causes reformation of the interatomic bonding. For charged argon dimer the dissociation energy is 1.5 eV when the dissociation energy for neutral argon dimer is 12 meV. For neutral xenon dimer the dissociation energy is 24 meV and for charged xenon dimer 1.03 eV. [1, 17]

In argon atom all the outer valence orbitals are occupied. This leads to the fact that according to the molecular orbital theory all the molecular orbitals are occupied when a

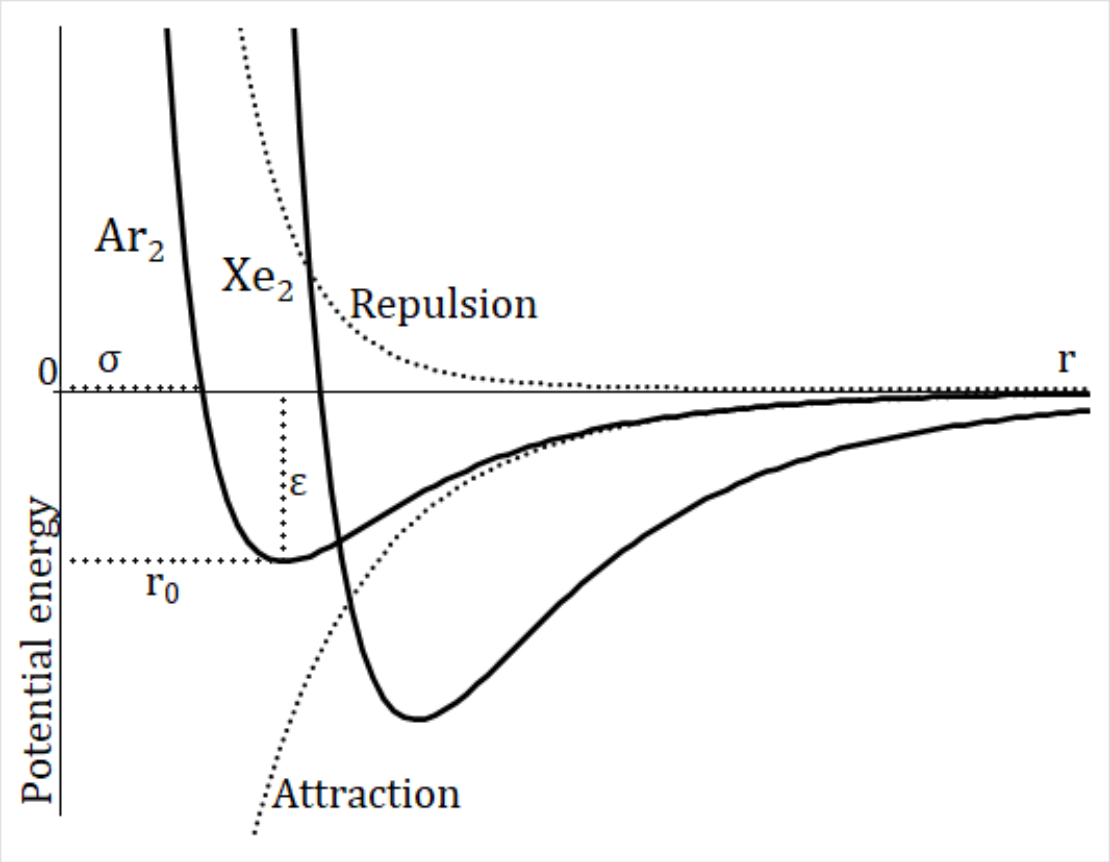

Figure 3: Lennard-Jones potentials for argon and xenon dimers are shown in black, solid curves. For argon dimer repulsion and attraction part of the Lennard-Jones potentials are shown in two dotted lines. The y-axis presents the potential energy V between the atoms, and the x-axis presents the internuclear distance r. When the curve is under zero the attraction term of the Lennard-Jones potential is greater than the repulsion part of the formula. The stability of the bonding increases as a function of the potential well depth ε. When the repulsion part is larger, the curve is above zero and the distance between the atoms is at its smallest. The internuclear distance, when the potential curve is zero, is described as σ. The lowest part of the curve describes the distance r_0 in which the bonding between the atoms is strongest. The longer the distance r between the atoms the weaker the interaction between the atoms is. The depth of the potential well ε is greater in xenon dimer. Therefore, the strength of the bonding is weaker in argon dimer than in xenon. The width of the potential well is wider for xenon dimer which also affects to the stability of the bonding compared to argon dimer. [14]

dimer is formed. Ground state electron configuration of valence orbitals for argon dimer is $(\sigma_{g(3s)})^2(\sigma_{u(3s)})^2(\sigma_{g(3p_z)})^2(\pi_{g(3p_{x,y})})^4(\pi_{u(3p_{x,y})})^4(\sigma_{u(3p_z)})^2$. From the configuration the strength of bonding can be deduced using the bond order presented in equation 2. [14]

$$b_{Ar_2} = \frac{1}{2}(16 - 16) = 0$$

Now the bond order is 0. This means that there is no covalent bonding between argon dimers. However, the situation changes when the argon dimer in ionized. The lowest electronic state for ionized argon dimer molecule is found when the electron is removed from the antibonding molecular orbital $(\sigma_{u(3p_z)})^2$. The molecular orbital configuration for Ar_2^+ is $(\sigma_{g(3s)})^2(\sigma_{u(3s)})^2(\sigma_{g(3p_z)})^2(\pi_{g(3p_{x,y})})^4(\pi_{u(3p_{x,y})})^4(\sigma_{u(3p_z)})^1$ and the bond order for charged argon dimer can be calculated as follows. The bonding in charged argon cluster is mildly covalent. [14]

$$b_{Ar_2^+} = \frac{1}{2}(16 - 15) = \frac{1}{2}$$

In case of xenon clusters the configuration for molecular orbitals is $(\sigma_{g(5s)})^2(\sigma_{u(5s)})^2$ $(\sigma_{g(5p_z)})^2(\pi_{g(5p_{x,y})})^4(\pi_{u(5p_{x,y})})^4(\sigma_{u(5p_z)})^2$. In neutral argon dimer nor in neutral xenon dimer there is no covalent bonding between the atoms. The bond order for xenon can be calculated as for argon. [14]

$$b_{Xe_2} = \frac{1}{2}(16 - 16) = 0$$

The bond order for ionized xenon dimer Xe_2^+ can be calculated as well. The lowest energetic state is found when the electron is ionized from antibonding molecular orbital $(\sigma_{u(5p_z)})^2$. Now the molecular orbitals for xenon can be written as $(\sigma_{g(5s)})^2(\sigma_{u(5s)})^2$ $(\sigma_{g(5p_z)})^2(\pi_{g(5p_{x,y})})^4(\pi_{u(5p_{x,y})})^4(\sigma_{u(5p_z)})^1$, and the bond order for ionized xenon dimer is 1/2. [14]

$$b_{Xe_2^+} = \frac{1}{2}(16 - 15) = \frac{1}{2}$$

2.2.4 Bonding in a water molecule

Water clusters are formed from water molecules. To understand the structure and properties of water clusters it is important to understand the bonding within a water molecule. The bonding in a water molecule affects the bonding between individual water molecules and therefore the bonding in water clusters. By understanding the bonding in water clusters several other properties can be understood. [8, 18]

In molecular orbital theory, group theory is used to understand the bond formation in molecules. The extension of molecular orbital theory can be used to understand the electronic structures in solids. As the cluster size increases, somewhat similar approximations as in solids must be done to understand the electronic structures of clusters. [12]

The symmetry properties of a molecule are used to classify and determine molecular orbitals. Therefore, the group theory is an important part of molecular orbital theory. As was already introduced in section 2.2.1 water molecule belongs to symmetry group C_{2v}. The symmetry operations of water molecule are identity E, rotation C_2 and reflections σ_v and $\sigma_{v'}$. In comparison, rare gas dimer belongs to symmetry group of $D_{\infty h}$. The symmetry operations for the group are identity E, rotations C_∞ and ∞C_2, reflections $\infty\sigma_i$, inversion

i and improper rotations S_∞. Point group $D_{\infty h}$ tells that rare gas dimer is linear and homoatomic. $D_{\infty h}$ point group has infinite amount of reflection planes and C_2 rotation axes. In addition, there are one axis of C_∞ rotations and one axis of S_∞ improper rotations. [12] Here the water molecule alone belongs to symmetry group C_{2v} when the water dimer consists of two molecules each belonging to symmetry group C_{2v}. The symmetry group for linear water dimer shown in figure 6 is C_s. Symmetry operations of C_s symmetry group are identity E and reflection σ_h. The symmetry properties of the molecule or atoms affect significantly to the bonding and possible structures that can be seen in clusters. [12, 13, 19]

Water is a compound that consists of two hydrogen atoms and one oxygen atom. Electron configuration for neutral hydrogen is $[H] = 1s^1$ and the electron configuration for oxygen atom is $[O] = 1s^2 2s^2 2p^4$. From the electron configurations it can be seen that a hydrogen atom has just one proton and one electron, which means that the $1s$ atomic orbital is not fully occupied. Oxygen has eight protons and neutrons in the nucleus and eight electrons in the electron cloud. As can be seen from the electron configuration, oxygen has two electrons missing from the fully occupied $2p$ orbital. [5]

A water molecule is formed when both hydrogen atoms form covalent bonds with an oxygen atom. The valence electrons are shared between atoms forming the bonds, meaning that now both the hydrogens and the oxygen have a closed shell electron configuration in the valence. The bonding in water molecule can be modelled using molecular orbital theory and group theory. The symmetry operations of water molecule are applied individually to atomic orbitals of the atoms that the molecule has formed. This is how the atomic orbitals that contribute to molecular orbitals of water molecule can be determined. A character table describing the symmetry group is presented in the Table 1 [13]. [5, 12]

Table 1. The C_{2v} character table

C_{2v}	E	C_2	σ_v	σ_v'
A_1	1	1	1	1
A_2	1	1	-1	-1
B_1	1	-1	1	-1
B_2	1	-1	-1	1

In formation of molecular orbitals for water, two guidelines must be followed: orbitals of similar orientation can be interacting, and significant interactions can happen only with electrons with energies close to each other. As introduced earlier, water molecule belongs to point group C_{2v}. The symmetries of hydrogen atomic orbitals and oxygen valence orbitals are used to form molecular orbitals for water. To determine which of the orbitals can interact, the symmetries of the atomic orbitals must be determined first. [13]

The consideration of hydrogen $1s$ orbitals cannot be separated. The atomic $1s$ orbitals can have amplitudes of the same or opposite signs. When the waves of the atomic orbitals are constructive, they are in-phase and correspondingly when the waves are destructive, they are out-of-phase. The base that the two $1s$ orbitals of hydrogen form can be presented in 2×2 matrix is $\left(\begin{smallmatrix} 1 & 0 \\ 0 & 1 \end{smallmatrix}\right)$. Using the operations in hydrogen basis the following can be calculated. [13]

$$\hat{E} \begin{pmatrix} 1 & 0 \\ 0 & 1 \end{pmatrix} = \begin{pmatrix} 1 & 0 \\ 0 & 1 \end{pmatrix}$$

$$\hat{C}_2 \begin{pmatrix} 1 & 0 \\ 0 & 1 \end{pmatrix} = \begin{pmatrix} 0 & 1 \\ 1 & 0 \end{pmatrix}$$

$$\hat{\sigma}_v \begin{pmatrix} 1 & 0 \\ 0 & 1 \end{pmatrix} = \begin{pmatrix} 0 & 1 \\ 1 & 0 \end{pmatrix}$$

$$\hat{\sigma}_{v'} \begin{pmatrix} 1 & 0 \\ 0 & 1 \end{pmatrix} = \begin{pmatrix} 1 & 0 \\ 0 & 1 \end{pmatrix}$$

Now reducible presentation for hydrogen $1s$ orbitals can be determined by calculating the character of the symmetry operation from equation 11 [12].

$$\chi(R) = Tr\mathbf{D}(R) \tag{11}$$

In equation 11 R is the symmetry operation and Tr trace of a matrix $\mathbf{D}(R)$. The characters of symmetry operations are:

$$\chi(\hat{E}) = Tr \begin{pmatrix} 1 & 0 \\ 0 & 1 \end{pmatrix} = 2$$

$$\chi(\hat{C}_2) = Tr \begin{pmatrix} 0 & 1 \\ 1 & 0 \end{pmatrix} = 0$$

$$\chi(\hat{\sigma}_v) = Tr \begin{pmatrix} 0 & 1 \\ 1 & 0 \end{pmatrix} = 0$$

$$\chi(\hat{\sigma}_{v'}) = Tr \begin{pmatrix} 1 & 0 \\ 0 & 1 \end{pmatrix} = 2$$

These results are presented in the Table 2 below as reducible representation [13].

Table 2. Reducible representation for hydrogen 1s orbitals

C_{2v}	E	C_2	σ_v	$\sigma_{v'}$
Γ_{H1s}	2	0	0	2

Using the character table and reducible representation the number of times the irreducible representation occurs in reducible representation a_i can be determined. This can be done using equation 12. [12, 13]

$$a_i = \frac{1}{h} \sum (\chi_{(R)} \chi_{(IR)}) \tag{12}$$

In reduction formula h is the group order, $\chi_{(R)}$ is the character for the particular operation in reducible representation when $\chi_{(IR)}$ is the character for the particular operation in irreducible presentation. [12, 13]

$$a_{a_1} = \frac{1}{4}((2 \cdot 1) + (0 \cdot 1) + (0 \cdot 1) + (2 \cdot 1)) = \frac{1}{4} \cdot 4 = 1$$

$$a_{a_2} = \frac{1}{4}((2 \cdot 1) + (0 \cdot 1) + (0 \cdot -1) + (2 \cdot -1)) = 0$$

$$a_{b_1} = \frac{1}{4}((2 \cdot 1) + (0 \cdot -1) + (0 \cdot 1) + (2 \cdot -1)) = 0$$

$$a_{b_2} = \frac{1}{4}((2 \cdot 1) + (0 \cdot -1) + (0 \cdot -1) + (2 \cdot 1)) = 1$$

From above the symmetry labels for hydrogen $1s$ orbitals are a_1+b_2. Representation tells that hydrogen $1s$ orbitals can be combined in two ways that have different symmetries A_1 and B_2. The molecular orbital a_1 is a sum of $1s$ atomic orbitals and is therefore symmetric. Whereas the molecular orbital b_2 is formed as a remainder of the atomic orbitals. The sign of the wavefunction of the molecule orbital b_2 changes in between the hydrogen atoms. In case of oxygen the symmetry labels can be determined straightforwardly from the shapes of the atomic orbitals. The determination is shown graphically for $2p$ orbitals in figure 4. For orbital $2s$ the determination is trivial due to its spherical geometry. If the operation changes the symmetry of the orbital, it is marked as -1 in the table whereas if the orbitals stay unchanged in the operation it is marked as 1. The results are presented as reducible representation of atomic orbitals $2s$ and $2p$ in the Table 3. In addition, the symmetry labels in Table 3 are determined using the character table for point group C_{2v}. [13]

Table 3. Reducible representation for valence orbitals of oxygen

C_{2v}	E	C_2	σ_v	$\sigma_{v'}$	
Γ_{2s}	1	1	1	1	a_1
Γ_{2p_x}	1	-1	1	-1	b_1
Γ_{2p_y}	1	-1	-1	1	b_2
Γ_{2p_z}	1	1	1	1	a_1

The symmetry labels in Table 3 above are determined using the character table for point group C_{2v}. When the symmetry labels have been determined the molecule orbital diagram for water molecule can be formed. The ionization energies for atomic orbitals cannot be neglected. Ionization energy for hydrogen $1s$ orbital is 13.6 eV, when ionization energy for oxygen $2s$ and $2p$ orbitals are 32.4, and 15.9 eV. The ionization energy of oxygen $2s$ orbital differ from the other energies. Therefore, the electrons of $2s$ orbitals do not take part in the bonding. The molecular orbital diagram for water is presented in figure 5. From the diagram, it can be seen, that the symmetries and energies of hydrogen $1s$ orbitals are suitable to form bonds with orbitals of oxygen $2p_y$ and $2p_z$ orbitals. [13]

The bond order in water molecule can be determined using the molecular orbital diagram presented in figure 5 and equation 2 [14].

$$b_{H_2O} = \frac{1}{2}(4 - 0) = 2$$

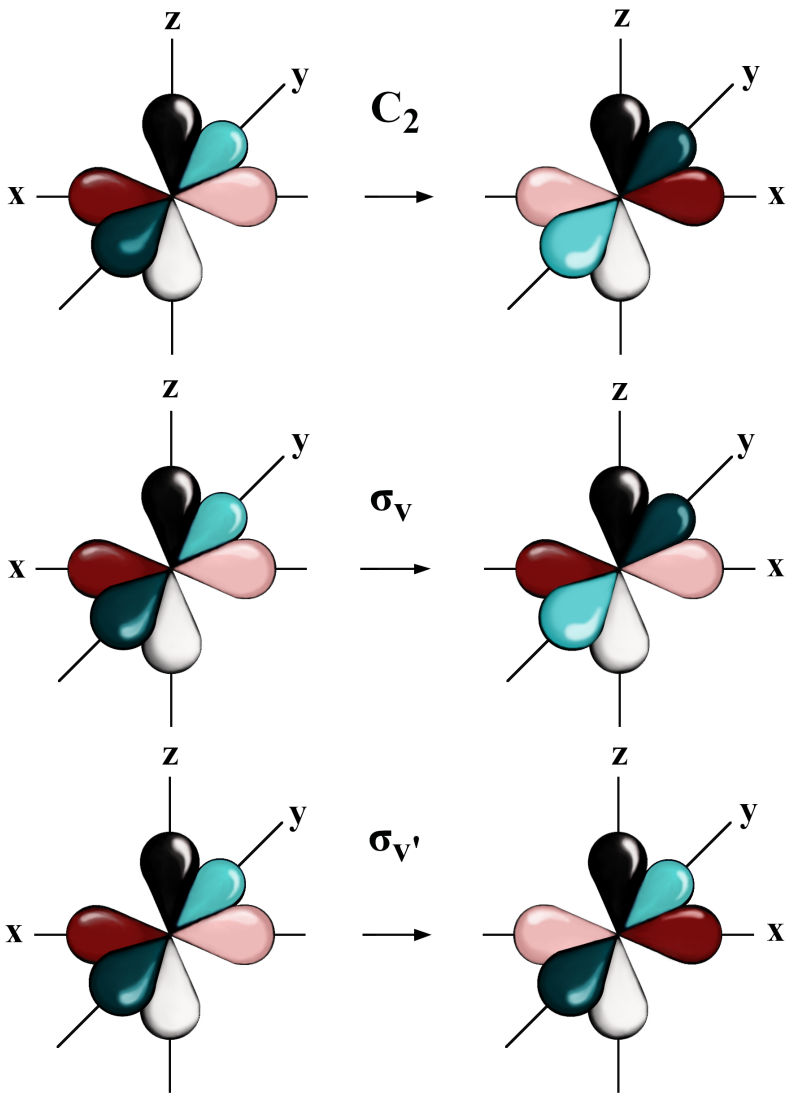

Figure 4: Demonstration how the symmetry operations affect the $2p$ orbitals of oxygen atom. If the symmetry operation does not affect the orbital, it is marked as 1 and if there is a change in the symmetry it is marked as -1 in the Table 3. The operation of symmetry operation E is trivial and is therefore neglected from this figure. [12, 13]

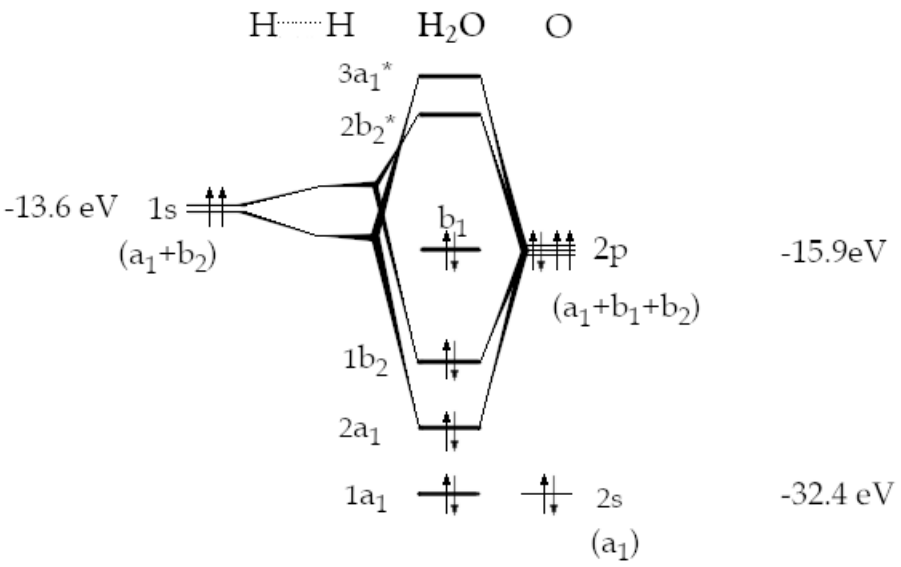

Figure 5: Molecular orbital diagram describes the chemical bonding in water molecule. The energies of the electrons in initial atomic orbitals are marked in the figure. The two electrons from oxygen $2s$ orbital form the molecular orbital $1a_1$. Molecular orbitals $2a_1$ and $1b_2$ are formed from the hydrogen $1s$ atomic orbitals and $2p_y$ and $2p_z$ of oxygen atomic orbitals. $1b_1$ orbital is formed completely from the two electrons from $2p_x$ orbital. The antibonding orbitals $2b_2^*$ and $3a_1^*$ are empty. [13]

The bond order in water molecule between oxygen and hydrogen atoms is 2, which corresponds to a strong bonding. The strength of the bond is reflected also to the average bond length between O-H atoms which is 95.7 pm. The angle between the two hydrogen atoms in water molecule is 104.55°. The dissociation energy of O-H bond in water molecule is 4.76 eV at 0 K temperature. [18]

2.2.5 Hydrogen bond

The bonds between water molecules in water clusters and protonated water clusters are hydrogen bonds. Hydrogen bonds describe an interaction between hydrogen and in this case oxygen atom of separate molecules. The bonding arises from the high electronegativity differences between the atoms of the molecules. Electronegativity is element's property to attract shared electrons. In water molecule the electronegativity difference between hydrogen and oxygen atom is relatively high. An oxygen atom is more electronegative than a hydrogen atom. Therefore, in water molecule the oxygen atom has a negative partial charge

while hydrogen atoms have a positive partial charge. [5, 10]

To describe a hydrogen bond often 10-12 Lennard-Jones potential is used. 10-12 Lennard-Jones potential, written in equation 13, describes the interaction between the heteroatom and the hydrogen. In equation 13 r is the internuclear distance. A and C are constants and can be written as $A = \varepsilon r_m^{12}$ and $C = 2\varepsilon r_m^{10}$. r_m is the distance in which the bond potential is at minimum and ε is the depth of the potential well. [16]

$$v(r) = \frac{A}{r^{12}} - \frac{C}{r^{10}} \tag{13}$$

The energy and the length of the hydrogen bond varies in different situations. The energy minimum for hydrogen bond is -0.15 eV and the bond length is around 2.952 Å between water molecules in a linear water dimer. The distance is measured between the oxygen atoms. In figure 6 the structure of linear water dimer is shown. [18, 20, 21]

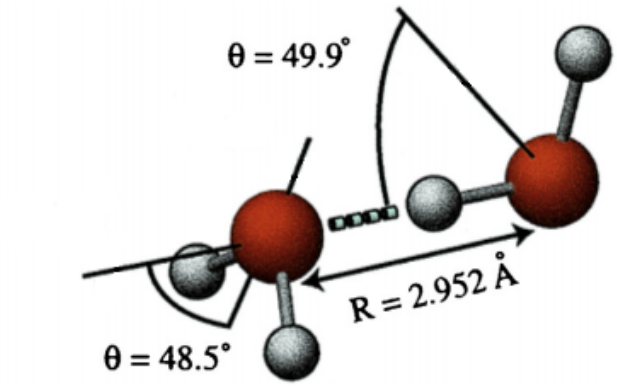

Figure 6: Schematic figure of a linear water dimer. The angles and the bond lengths are marked in the figure. The bond strength in this dimer is 0.15 eV. *Reprinted from Chemical Physics Letters, Vol. 633, Anamika Mukhopadhyay, William T.S. Cole, Richard J. Saykally, The water dimer I: Experimental characterization, Pages 13-26, Copyright (2015), with permission from Elsevier.* [21]

2.3 Cluster structures

The structures of clusters depend on the number of atoms or molecules in the cluster. For smaller clusters, the number of isomers is smaller when for increasing cluster size the number of isomers is naturally larger. Isomers in clusters consists of the same amount of molecules or atoms but the structure of the cluster differs. The second significant factor for structures is whether the cluster is formed from atoms or molecules. The substance in which the cluster is formed affects to the bonding in cluster. In molecular clusters the geometrical structures of the molecules affect to the possible structures in clusters. If the cluster is formed from individual atoms the cluster structure is more organized. [1, 23]

2.3.1 Rare gas clusters

A mass spectra measured for xenon and argon by O. Echt et al. [24] and I. Harris et al. [25] suggest that the intensities of cluster peaks do not decrease smoothly with cluster size. According to their study there are more intensive peaks in cluster sizes corresponding to magic numbers. These magic numbers describe clusters that show geometrically stable structures [1, 18].

In study of C. Amano et al. [26], the relation between interatomic potential and structure of rare gas clusters is studied. According to their study icosahedron structure was the most stable when the potential model applied was Lennard-Jones 12-6 potential. Magic numbers in rare gas clusters correspond to the complete icosahedron shells. Equation 14 presents the magic numbers of icosahedron shell structure. In equation 14 N is the number of atoms or molecules in the cluster and K is the number of complete shells. The outer shells of icosahedron clusters are called Mackay icosahedral. Icosahedron structure model is applied to neutral rare gas clusters. There is no agreement whether the cluster structures are the same for neutral and positively charged clusters. [1, 26]

$$N(K) = \frac{1}{3}(10K^3 + 15K^2 + 11K + 3) \tag{14}$$

According to equation 14 peaks of clusters of N=13, N=55, N=147 and so on should be more intense in the mass spectra. However in xenon cluster spectra presented in by Echt et al. [24] there are also peaks that do not fit into icosahedron structure model straightforwardly. Some magic numbers that lack from the series given by the equation 14 can be explained by combination of an incomplete shell and a previous complete shell. [1]

There are theoretical calculations to model the structure of rare gas clusters when the number of atoms differ from the magic numbers. These additional atoms are located on a three-fold hollow on the faces of the icosahedron. This is called anti-Mackay packing. However, when the number of atoms increases the Mackay icosahedral becomes more favorable again. The reason for rare gas clusters to form icosahedron structures is the low surface energy. In icosahedron structure the number of neighbor atoms in the surface of the cluster is larger compared to other possible clusters structures. Large number of interactions of surface atoms leads to lower surface energy and therefore more stable structure. The maximum amount of interactions between atoms causes the maximum total binding energy. [1, 26]

In study of I. A. Harris et al. [25], the mass spectra of argon shows the same magic numbers as can be seen from the study of O. Echt et al. [24] for xenon. However, Harris presents a model to explain all the intense peaks in the spectra. The empirical model derived by Harris is presented elsewhere [25].

2.3.2 Water clusters and mixed clusters

For protonated water clusters there are three different types of structures. The cluster structures and isomers described are presented in figure 7. At small cluster sizes $N \leq 10$ chain structures are seen. Net structures are common when the cluster size varies around 10 to 20 molecules. When the cluster size is over 20, three-dimensional cage structures are formed. [27]

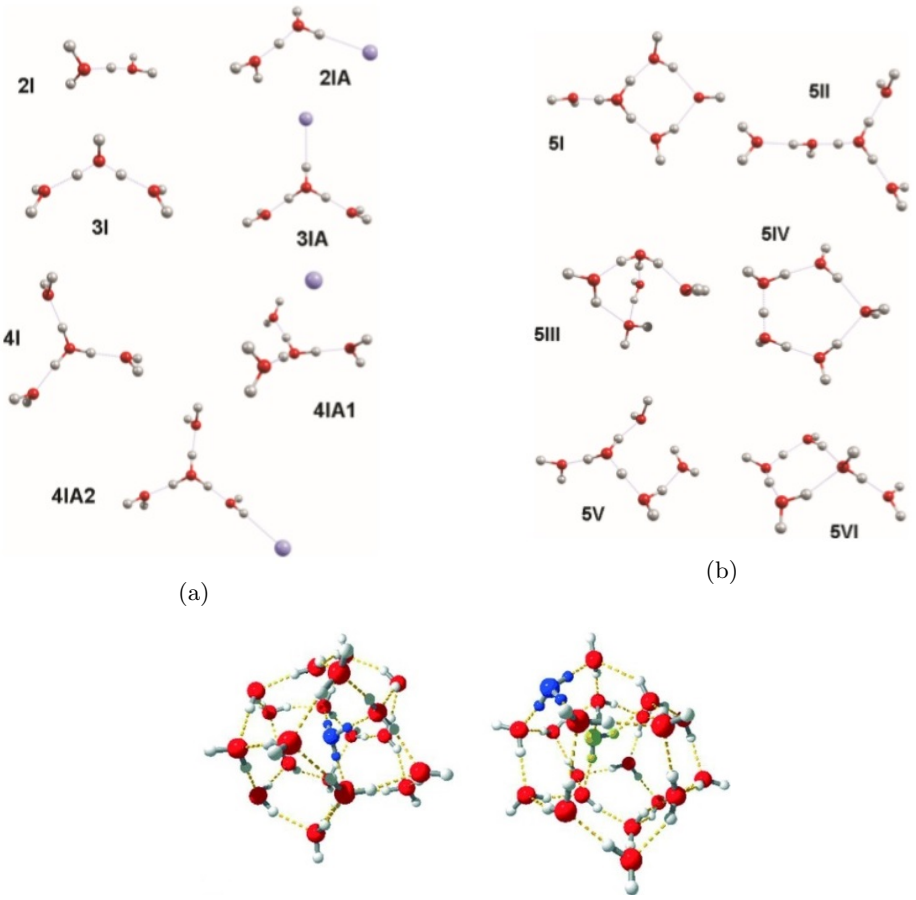

(a)

(b)

(c)

Figure 7: Structures of protonated water and water-argon clusters [9, 27]. In figure 7a the structures of small protonated water clusters with (2IA, 3IA, 4IA1, 4IA2) and without (2I, 3I, 4I) argon are presented in figure. Of mixed 4-mer clusters in figure 7a two isomers are shown. In figure 7b the isomers of 5-mer protonated water clusters are presented. Figure 7c shows the two isomers of $(H_2O)_{21}H^+$ clusters. The cluster size is the smallest magic number to appear in protonated water clusters. The H_3O^+ molecule is marked in blue. *Reprinted (adapted) with permission from American Chemical Society, G. E. Douberly, R. S. Walters, J. Cui, K. D. Jordan, M. A. Duncan, Infrared Spectroscopy of Small Protonated Water Clusters, H+(H2O)n,(n = 2 - 5): Isomers, Argon Tagging and Deuteration, J. Phys. Chem. A, Vol. 114, No. 13, pp. 4570-4579, (2010). Copyright (2010) American Chemical Society.* and *John Wiley and Sons, R. Ludwig, Protonated water clusters: The Third Dimension, ChemPhysChem, Vol. 5, Iss.10, pp. 1495-1497, (2004). Copyright (2004) WILEY-VCH Verlag GmbH and Co. KGaA, Weinheim.* [9, 27]

In the study of G. E. Douberly et al. [9] structures of small protonated water clusters with and without argon are studied. According to their study in protonated water dimer the two water molecules are bonded via an extra proton. In a trimer cluster the two water molecules are attached to a H_3O molecule symmetrically. In 4-mer the fourth water molecule is attached to one hydrogen that was left free in trimer cluster. In mixed argon-water clusters the argon atom in cluster is always attached to one of the outermost hydrogen atoms. There are two isomers in 4-mer mixed clusters. In 5-mer protonated water clusters there are six possible isomers. In net structures water molecules form rings of five or six molecules. The H_3O^+ molecule in net structures is often in the joint of rings in the cluster. In cage structures H_3O^+ molecule can be either in the center of the cage or in the surface as can be seen from the figure 7c. [9, 27]

As in rare gas clusters in protonated water clusters magic sizes can be found. The smallest magic numbers in protonated water clusters occur at cluster sizes of N=21, N=28 and N=30. [1]

2.4 Cluster formation in adiabatic expansion

In this thesis the clusters are formed in expansion of gas through a conical nozzle. A formation of clusters is possible if the thermal energy of the gas is lower than the binding energy in a dimer. The acquired thermodynamic non-equilibrium, for cluster formation, is created is when the gas expanses from high gas pressure into the vacuum. A dimer, the smallest possible cluster, is formed in a three-body collision. In the three-body collision energy is released in bond formation. The cluster formation is presented in equation 15 where A describes an atom or a molecule and B is the third partner that is needed to preserve energy and momentum. The third particle B removes an excess energy (E) and therefore stabilizes the formed dimer. In reaction equation 15 kinetic energy is $E_2 > E_1$. [1, 22]

$$A + A + B(E_1) \rightarrow A_2 + B(E_2) \tag{15}$$

Furthermore, collisions between smaller clusters can lead to formation of larger clusters as presented below, where N and M describe the number of atoms or molecules in the cluster. [1]

$$A_N + A_M + B \rightarrow A_{N+M} + B$$

There are also different models proposed for cluster formation. In these models a cluster can be formed in a two-body collision creating a temporary unstable cluster. The excess energy released in bond formation is dissipated by inelastic collisions with a third particle. [28, 29]

2.5 Cluster sizes and size models

2.5.1 Rare gas clusters

For argon and xenon, a size model for clusters produced via adiabatic expansion has been proposed by U. Buck and R. Krohne [30]. In adiabatic expansion always a distribution of different-size clusters is formed and therefore the model by U. Buck and R. Krohne describes the mean cluster sizes $\langle N \rangle$. The width of the distribution is approximated to be $\Delta N = \langle N \rangle / 2$. In the model, a scaling parameter Γ^* introduced by O. F. Hagena [31] is used. The scaling parameter is experimentally determined, and it depends on expansion

pressure p_0, nozzle temperature T_0 and equivalent diameter of the nozzle d_{eq}. In addition, K_{ch} is a constant derived for different elements. Equation for scaling parameter is presented in formula 16. [30]

$$\Gamma^* = \frac{p_0 \cdot d_{eq}^{0.85}}{T_0^{2.2875}} K_{ch} \tag{16}$$

The size model created by U. Buck and R. Krohne is produced by bombarding argon clusters by helium atoms and then measuring the angular dependency of the scattered helium atoms. Angular distributions were measured as a function of stagnation pressure and nozzle size. This study led to three different empirical formulas for different experimental situations. When $\Gamma^* \leq 350$ formula 17 should be used according to the size model. Values for the coefficients are $a_0 = 2.23$ $a_1 = 7.00 \times 10^{-3}$ $a_2 = 8.30 \times 10^{-5}$ and $a_3 = 2.55 \times 10^{-7}$. [30]

$$\langle N \rangle = a_0 + a_1 \Gamma * + a_2 (\Gamma^*)^2 + a_3 (\Gamma^*)^3 \tag{17}$$

When $350 \leq \Gamma^* \leq 1800$ formulae 18 and 19 should be used. Formula 18 is produced by U. Buck and R. Krohne, but the formula 19 is from the O. F. Hagena's model [31, 32]. U. Buck and R. Krohne suggests that formula 18 is to be used for cluster sizes $\langle N \rangle = 6$ to $\langle N \rangle = 90$. Formula 19 is for bigger cluster sizes. [30]

$$\langle N \rangle = 38.4 \left(\frac{\Gamma^*}{1000} \right)^{1.64} \tag{18}$$

$$\langle N \rangle = 33 \left(\frac{\Gamma^*}{1000} \right)^{2.35} \tag{19}$$

When $\Gamma^* \geq 1800$ U. Buck and R. Krohne suggest that formula 20 should be used. In formula 20 the values for coefficients are $b_0 = -12.83$ and $b_1 = 3.51$. [30]

$$\langle N \rangle = exp(b_0 + b_1 (ln \Gamma^*)^{0.8}) \tag{20}$$

The size model presented here is not necessary very accurate. For instance, there may be some inaccuracies especially in the results where the used formula changes. However, the model is useful to derive an approximation of the cluster sizes.

2.5.2 Water clusters

In the article *Fragmentation and reliable size distributions of large ammonia and water clusters* by C. Bobbert et al. [23] a size model for neutral water clusters is derived. Even though the model presented here is not particularly generated for mixed argon water experiments it may give some idea of the size distributions of generated clusters. The size model is formed by modifying O. F. Hagena's [31, 32] scaling law. According to the model a key parameter is presented to describe the flow in expansion through the nozzle in which the clustering occurs. The scaling parameter is presented in equation 21.

$$\begin{aligned} \Gamma &= n_0 d^q T_0^{sq - f/2} \\ s &= (f-2)/4 \end{aligned} \tag{21}$$

In equation 21 n_0 is source density, T_0 nozzle temperature and d diameter of the nozzle. Parameter q $(0 < q \leq 1)$ describes the speed of the flow. For larger diameter nozzles

the flow is slower. In scaling parameter f is the number of energetically active degrees of freedom. Parameter f appears in s, which is the axially symmetric flow. For water there are 3 translational and 3 rotational degrees of freedom. Therefore, for water $f = 6$. The value for parameter s is calculated as $s = (f - 2)/4 = (6 - 2)/4 = 1$. Now the scaling parameter can be written as $\Gamma = n_0 d_{eq}^q T_0^{q-3}$. [23]

To expand the expression of the key parameter for different gases a reduced scaling parameter must be derived. Reduced scaling parameter is presented in equation 23. [23]

$$\Gamma^* = \Gamma / K_{ch} \tag{22}$$

In equation 23, parameter K_{ch} depends on two constants r_{ch} and T_{ch}. Values for water are determined to be $r_{ch} = 3.19\mathring{A}$ and $T_{ch} = 5684K$. [23]

$$K_{ch} = r_{ch}^{q-3} T_{ch}^{q-3} \tag{23}$$

After determination of the reduced scaling law the mean cluster sizes $\langle N \rangle$ for water clusters can be calculated from equation 24.

$$\langle N \rangle = D \left(\frac{\Gamma^*}{1000} \right)^a \tag{24}$$

In equation 24, D and a are constants determined for water as 11.60 and 1.886, respectively. In addition, value for q is 0.634. [23]

2.6 Ionization and fragmentation of clusters

In this thesis the studied clusters are ionized by electron impact. As an ionization method, electron ionization is a high fragmentation method [33]. Collision between a high energy electron and a cluster causes the cluster to get ionized and to break up to smaller fragments [34]. The energy of the ionizing electron must be higher than the ionization energy [33]. There are several different ionization channels for electron impact ionization in production of positive ions. The ionization process is very fast since the ejected electron leaves the atom within 10^{-16} seconds. The possible dissociation of a cluster occurs after the ionization. The ionization and fragmentation processes can be described in reaction equations where AB describes the cluster, e is ionizing electron, e_s is the scattered electron, and e_e is the electron ejected from the cluster. A cluster can be singly, doubly, or multiply ionized and the processes are shown in reaction equation 25, 26, and 27. [34]

$$AB + e \rightarrow AB^+ + e_e + e_s \tag{25}$$

$$AB + e \rightarrow AB^{2+} + 2e_e + e_s \tag{26}$$

$$AB + e \rightarrow AB^{z+} + e_s + z \cdot e_e \tag{27}$$

The ionization may lead to a fragmentation in which the initial cluster dissociates into two or more fragments. Possible fragmentation processes are described in reaction equations 28 and 29 for singly ionized cluster. In the fragmentation process described in equation 28 a positively charged and neutral fragment is formed whereas in process in equation 29 one positively and one negatively charged fragment is formed. [34]

$$AB + e \rightarrow A^+ + B + e_s + e_e \tag{28}$$

$$AB + e \rightarrow A^+ + B^- + e_s \tag{29}$$

Correspondingly, doubly charged clusters can be decomposed in two different ways described in reaction equations 30 and 31. In equation 30 doubly ionized cluster decomposes into two singly charged fragments when in equation 31 cluster decomposes into one doubly charged fragment and one neutral fragment. However, several studies show that doubly ionized cluster decomposing to two singly charged fragment is much more abundant process. [34]

$$AB^{2+} \rightarrow A^+ + B^+ \tag{30}$$

$$AB^{2+} \rightarrow A^{2+} + B \tag{31}$$

Ionization reactions can be classified into direct and indirect ionization processes. Direct ionization processes are single ionization, double ionization, multiple ionization, dissociative ionization and ion pair formation. The indirect processes are Auger process, autoionization, and fragmentation. These ionization processes can be described in reaction equations where AB describes the cluster, e is ionizing electron, e_s is the scattered electron, and e_e is the electron ejected from the cluster. In single ionization process the ionizing electron removes one electron. The reaction equation for single ionization is written as in equation 25. [34]

If the energy of the ionizing electron is high enough to ionize the electron from the inner shell, the ionization process is called core shell ionization [34]. However, the high ionization energy does not necessarily mean that the inner shell is ionized. It is possible that the ionization cross section may be higher for example for valence electrons [35]. Inner shell ionization is different from the single ionization due subsequent electron transitions that core shell ionization may cause. Inner shell ionization causes a core-hole into the ionized atom and is therefore called a core-excited state. The two different stabilization mechanism for excited-core-holes are fluorescence and Auger effect. Fluorescence occurs when the core hole is filled by an outer shell electron and the energy is released by electromagnetic radiation in the transition. In Auger decay, the energy released in filling the core hole, is given to other outer shell electron. This so-called Auger electron is ejected from the system. Fluorescence is more typical decay process for heavier elements and deep levels while the Auger decay is preferable for light elements and shallow core holes. Reaction equation for Auger effect after inner shell ionization is shown in equation 32, where e_A describes the Auger electron. [34,36]

$$AB + e \rightarrow A^+ + B^+ + e_s + e_e + e_A \tag{32}$$

Electron impact may cause also excitations on clusters. When the excited state relaxes the cluster can decompose into different fragments. In addition to previously presented processes electron impact on clusters may also cause vibrations and rotations [34].

Fragmentation of clusters is not fully understood phenomena. The study of D. Bonhommeau et al. [37] determines the fragmentation dynamics of small argon clusters caused by electron impact ionization. The study shows that the most abundant ionic fragments of argon are Ar^+ and Ar_2^+ when the cluster size $n < 6$. Trimer fragments Ar_3^+ appear the first time at cluster size of $n = 5$.

3 Measurements

This thesis focuses on the study of argon, xenon and mixed argon-water clusters via mass spectroscopy measurements and ion-ion coincidence measurements. Size properties of the clusters were studied as a function of ionization energy but also as a function on expansion pressure. With xenon clusters traditional mass spectroscopy measurements were on focus. For argon and argon-water clusters both mass spectroscopy and coincidence spectra were measured. Measurements were carried out using a time-of-flight spectrometer.

In mass spectroscopy studies with the time-of-flight spectrometer, mass-to-charge ratio (m/q) of ions is measured. Ions with different masses and charges have different flight times. The heavier the ion the longer the measured flight time is. From the different flight times the mass-to-charge ratios of the ions can be determined. [38]

In ion-ion coincidence studies two or more charged fragments in dissociation process are detected. In this thesis triple coincidences are studied. In triple coincidences the original cluster is fragmented in three or more parts but only three ions are detected. Due the coincidence measurements it is possible to determine the fragments that originated from a certain cluster. [39]

3.1 Measurement configuration

Clusters were produced in adiabatic expansion through a conical nozzle into the cluster chamber. The length of the used nozzle is 5 mm, full opening angle is 40° and the diameter of the nozzle is $20\mu m$. During the measurements the temperature of the nozzle was circa $25°C$. The nozzle is attached to an electrical manipulator to align the nozzle and the cluster beam towards the skimmer and interaction region. Nozzle is shown in figure 8. A skimmer separates cluster chamber from a main chamber to maintain the pressure differences between the chambers. Due to adiabatic expansion the cluster chamber is in a higher pressure compared to the main chamber. Due to the spectrometer, it is important that the vacuum in the main chamber is stable and low. It is ideal to keep the pressure under $10^{-5}mbar$. In addition, skimmer is used to let through only the cluster rich beam.

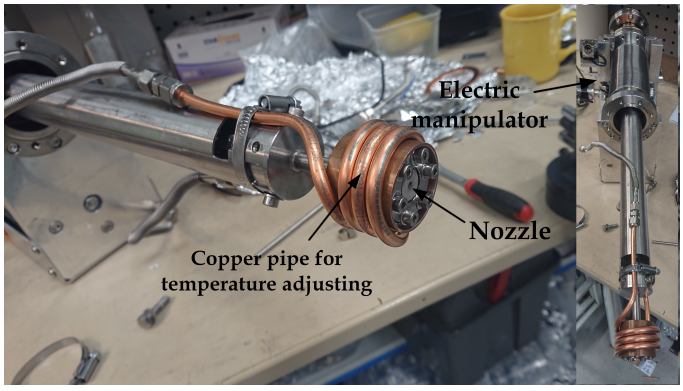

Figure 8: Picture of the cluster source used in the experiments. The parts of the cluster source are marked in the figure. The copper pipe in the figure is for adjusting the temperature of the nozzle during the measurements. However, in these measurements there was no need for temperature adjustment.

Electron gun is aligned so that the interaction region, the intersection point of electron and cluster beam, is in the middle of the extraction region of the time-of-flight spectrometer. The cluster and electron beams are at 90° angle with respect to each other. The electric field in the interaction region causes the positively charged ions to fly to the detector through the time-of-flight spectrometer. In mixed argon-water measurements a water container was added before the nozzle. Water evaporates from the container and mixes with the argon gas that was used as a carrier gas. The schematic picture of the measurement configurations is presented in figure 9.

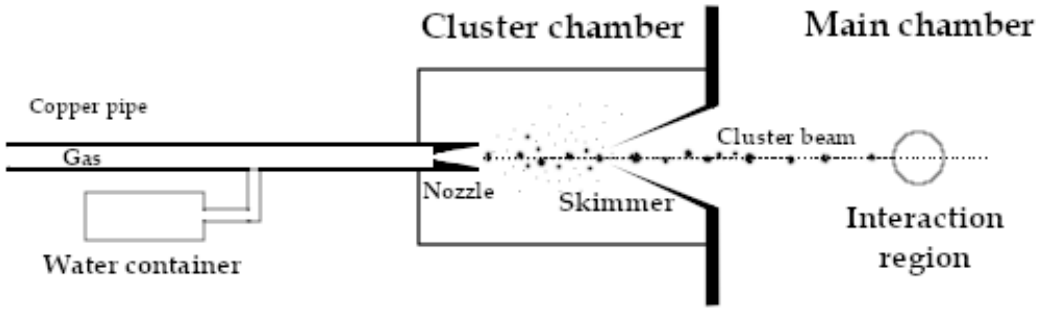

Figure 9: Measurement configuration used in this study. The water container is used only in the water-argon measurements.

3.2 Electron gun

In cluster ionization SPECS electron gun EQ 22/35 was used. The filament of the electron gun is heated to eject electrons. Ejected electrons are accelerated by a high voltage (HV) between the filament and an anode. By adjusting the voltage, the kinetic energy of the electrons in the beam can be determined. Detailed technical information of the used electron gun can be found in [40] and [41].

3.3 Time-of-flight spectrometer

The used mass spectrometer is time-of-flight spectrometer built in University of Oulu. The model of the spectrometer is Wiley-McLaren time of flight spectrometer presented in detail in [42].

3.3.1 Structure of spectrometer

A time-of-flight spectrometer consists of an extraction region, an acceleration region, and a drift region. At the end of the spectrometer there is a position sensitive detector. Due to the position sensitive detector, the momenta of the ions can be determined via this spectrometer. [43]

In the extraction region the electron beam interacts with the cluster beam. Extraction region consists of a repeller plate and an attractor mesh. The repeller plate has a hole in

the middle for cluster beam which is parallel to the spectrometer axis. The potential in the outer repeller plate is positive while the inner grid is in ground potential. The potentials are selected to create an electric field that causes positive ions to fly through the analyzer towards the detector. From the extraction region ions fly to the acceleration region. In the acceleration region ions are further accelerated into several keV. Such a high kinetic energy is necessary to ions to be properly imaged in the detector. In addition, the keV energy of ions is required for MCP to form a signal. [43]

Acceleration region consists of a single HV-circuit. In the circular aluminum rings are connected serially with resistors between composing a cylindrical tube. The aluminum rings functioning as electrodes together with the resistors of several MΩ form a potential chain, which forms a strong homogenous electric field inside the rings. Insulators are placed between the aluminum rings to prevent any electric contact. The length of the acceleration region is approximately 94 mm. [43]

From the acceleration region ions fly through the drift tube towards the detector. The purpose of the drift tube is to lengthen the time of flight to achieve a reasonable resolution. The drift tube is in a constant potential. Therefore, there is no electric field in the tube and ions can fly freely through it. The length of the drift region is approximately 664.5 mm. When the ions fly into the drift tube, they fly through an electrostatic lens element that is used for focusing. The lens element consists of an aluminum ring in high voltage. This causes a phenomenon that can be used to focus the ions towards the detector. Electrostatic lens is a significant tool especially for angle resolved experiments. [43]

3.3.2 Theoretical flight times

The whole flight time of an ion can be described as a sum of the times the ion spends in different regions of the spectrometer. Equation 33 describes the total flight time of the measured ion T, where T_{ER} is the time the ion is in extraction region, T_{AR} is the time the ion spends in the acceleration region, and T_{DR} is the time the ion is in the drift tube. [43]

$$T = T_{ER} + T_{AR} + T_{DR} \tag{33}$$

The ions that are going to be measured are created in the extraction region. The length of the whole extraction region is L_{ER}. The distance to the inner grid from the place of fragmentation is described as s. In electron bombardment ions get initial kinetic energy E_0 which affects the final flight times. In addition, the direction of the movement after the bombardment is must be taken to account. The angle between the detector and the initial velocity of the ion after fragmentation is described as θ_0. Using kinematics, Newton's second law $\Sigma\mathbf{F} = m\mathbf{a}$, Coulomb's force $\mathbf{F} = q\mathbf{E}$, and kinetic energy $E = \frac{1}{2}mv^2$ the total flight time of equation 33 can be calculated from the geometry and potential settings of the spectrometer, and initial kinetic energy and emission angle of the ion with a mass m and charge q. $\mathbf{F}$ is the force the ion experiences, $\mathbf{a}$ is the acceleration, $\mathbf{E}$ is the strength of the electric field, and $\mathbf{v}$ is the velocity. Now the flight time in extraction region is described in equation 34. [43]

$$T_{ER} = \frac{\sqrt{2m}}{q\|\overrightarrow{\mathrm{E_{ER}}}\|}\left(\sqrt{E_0 cos^2\theta_0 + q\|\overrightarrow{\mathrm{E_{ER}}}\|s} \pm \sqrt{E_0 cos^2\theta_0}\right) \tag{34}$$

The flight time in acceleration region is presented in equation 35.

$$T_{AR} = \frac{\sqrt{2m}}{q\|\overrightarrow{\mathrm{E_{AR}}}\|}(\sqrt{E_{TOT\|}} - \sqrt{E_0 cos^2\theta_0 + q\|\overrightarrow{\mathrm{E_{ER}}}\|s}) \tag{35}$$

The flight time in drift tube is presented in equation 36.

$$T_{DR} = \sqrt{\frac{m}{2E_{TOT\|}}}L_{DR} \tag{36}$$

In equations 34, 35 and 36, E_{TOT} is the total energy the ion gains in the spectrometer. E_{ER} and E_{AR} are the gained energies in extraction and acceleration regions. E_z is the initial energy parallel to electric fields in the spectrometer. [43]

$$E_{TOT} = E_Z + E_{ER} + E_{AR} = E_0 cos^2\theta_0 + q\|\overrightarrow{\mathrm{E_{ER}}}\| + q\|\overrightarrow{\mathrm{E_{AR}}}\|L_{AR} \tag{37}$$

Finally, the total flight time of the ion can be written as is equation 38.

$$\begin{aligned} T = &\left(\frac{\sqrt{2m}}{q\|\overrightarrow{\mathrm{E_{ER}}}\|}(\sqrt{E_0 cos^2\theta_0 + q\|\overrightarrow{\mathrm{E_{ER}}}\|s} \pm \sqrt{E_0 cos^2\theta_0})\right) \\ &+ \left(\frac{\sqrt{2m}}{q\|\overrightarrow{\mathrm{E_{AR}}}\|}(\sqrt{E_{TOT}} - \sqrt{E_0 cos^2\theta_0 + q\|\overrightarrow{\mathrm{E_{ER}}}\|s})\right) + \left(\sqrt{\frac{m}{2E_{TOT}}}L_{DR}\right) \end{aligned} \tag{38}$$

An approximation can be made for the equation 38. For mass spectroscopy data analysis, the equation presented below is sufficient for assigning the peaks from the mass spectra. In equation 39 T^m is the approximate time of flight for ions fragmented into different angles, A and C are experimentally determined constants. [43]

$$T^m = A\sqrt{\frac{m}{q}} + C \tag{39}$$

Constants A and C can be determined by using the flight times, charges, and masses of two known peaks deduced from the spectra. Then the constants A and C can be determined from the formed equation pair. [43]

3.3.3 Detector

The detector used in measurements is a HEX75 MCP/DLA-detector by RoentDek. To detect a single particle, microchannel plates (MCP) are used. Microchannel plates are made of highly resistive material with small microchannels going through the plate. When the measured ion collides to the inner wall of a microchannel, an electron is released from the wall. Due the electric field applied the electrons are accelerated and therefore cause more ionizations on their way through the MCP. Behind the MCP an electron cascade arrives to the delay line anode. [44]

A delay line anode (DLA) is the part of the detector for positional analysis. DLA is constructed from planar copper wires set on the top of each other at different angles. Crossing copper wires form a plane to detect the positions of the ions. When the electron avalanche collides to a delay line it creates an electric signal. The place of the impact is determined by measuring the time difference between signal's arrival times in both ends of the wire. The XY-position is determined from the intersection of the two different delay

lines. The detector used in this thesis consists of three delay lines. The third one is used to improve reliability of the results. Details of the used detector can be found from *MCP Delay Line Detector Manual* [44]. [43, 44]

3.3.4 Operation of the spectrometer

The used time-of-flight spectrometer has two function modes that can be applied for different kind of purposes: a constant field mode and a pulsed field mode. In this thesis the constant field mode was used in coincidence measurements while the pulsed field mode was used in traditional mass spectroscopy measurements. [43]

In pulsed field mode the voltage in the extraction region is pulsed with a high voltage pulser. Pulsed field mode was required in these experiments to determine the start of flight times of the ions. The end of the flight times is determined when the ion collide to the detector. Pulsed field in the extraction region enables a constant beam of electrons for the ionization. [43]

In the constant field mode, all the voltages in the time-of-flight spectrometer were kept constant. When the electron beam and the voltages in the spectrometer are constant the start time for flight times cannot be detected. In constant field mode the spectrometer measures the differences between the flight times of the fragments but does not determine absolute time-of-flights. Ions with different m/q have different flight times and the ion pairs can be assigned by measuring the flight time separation. [43]

3.3.5 Alignment

In each measurement the nozzle was aligned by using the electric manipulator and measuring the pressure in the main chamber. In addition, the count rate in the detector was used in alignment. When the maximum of the pressure was found in the main chamber then the nozzle was in the best possible place with respect to the skimmer. When the nozzle is aligned with respect to the skimmer, the maximum amount of clusters are getting into the main chamber which causes the pressure to grow.

The electron gun is to be aligned for each used energy separately. In electron gun alignment, the maximum amount of counts in the detector was used as a measure of alignment.

4 Data analysis and results

The measured mass spectra are analyzed by assigning the peaks. The absolute peak areas are determined and used to calculate relative abundancies between separate peaks. Detailed information of the measurements and used spectrometer is presented in chapter 3.

4.1 Xenon clusters

Xenon clusters were studied via three different measurement series. One series was measured as a function of expansion pressure and two of the series as a function of ionization energy with different expansion pressures. All the spectra were measured in the pulsed field mode.

4.1.1 Pressure dependency

The first series was measured as a function of expansion pressure while the electron energy for ionization is kept constant at 4000 eV. Pressure values in the measurements were 2.0, 3.0, 4.0, 5.0, 6.0, 7.0, 8.0, and 9.0 bar. Theoretical sizes for the clusters with different expansion pressures are calculated according to the model derived by U. Buck and R. Krohne [30] presented in section 2.5. Theoretically calculated cluster sizes are presented in the Table 4.

Table 4. Mean xenon cluster sizes as a function of pressure according to U. Buck and R. Krohne model

Pressure	2.0 bar	3.0 bar	4.0 bar	5.0 bar	6.0 bar	7.0 bar	8.0 bar	9.0 bar
Cluster size	15	29	46	67	90	160	220	290

In the calculated cluster sizes, there is a relatively large gap in the sizes between pressure 6.0 and 7.0 bar. This is due the fact that the calculation formula changes. According to model the cluster size increases more steeply at higher pressures.

The whole xenon cluster spectra for each expansion pressure are presented in the figure 10. As can be seen from the figure 10, the structure of the spectra is bimodal. Different parts of the spectra A, B and C are labeled in the figure. Figure 11 shows the differences in dimer, trimer, 4-mer, 5-mer, and 6-mer peaks between different spectra more closely, and part C of the spectra is shown in figure 12. A size distribution of spectral part A is presented in detail in figure 13.

Part A of the spectra represents the small fragments originated from the clusters. Flight times for the largest fragments in part A are around 50×10^3ns. For pressures 5.0 to 9.0 bar peaks up to 13-atom cluster can be recognized from the spectra. For pressures 2.0, 3.0, and 4.0 bar larger fragments can be recognized up to 25, 20, and 17 atoms as can be seen from the figure 13. The lower the expansion pressure the larger fragments are seen in the spectra in part A. The trend may be due the changes in initial cluster sizes. At smaller pressures there are only small clusters to be ionized in the cluster beam. At higher pressures the cluster beam may include clusters over 290 atoms. In smaller clusters the whole range of the sizes in the cluster beam is seen whereas at higher pressures the part A shows only the small fragments dissociated from the larger initial cluster. In higher pressures the 13-atom fragment may be the largest fragment that is possible to dissociate and detect from

the initial cluster. At lower pressures the fragment sizes over 13 atoms are probably from clusters that are singly ionized but are not fragmented in the process. The beginning of part A is presented more closely in figure 11.

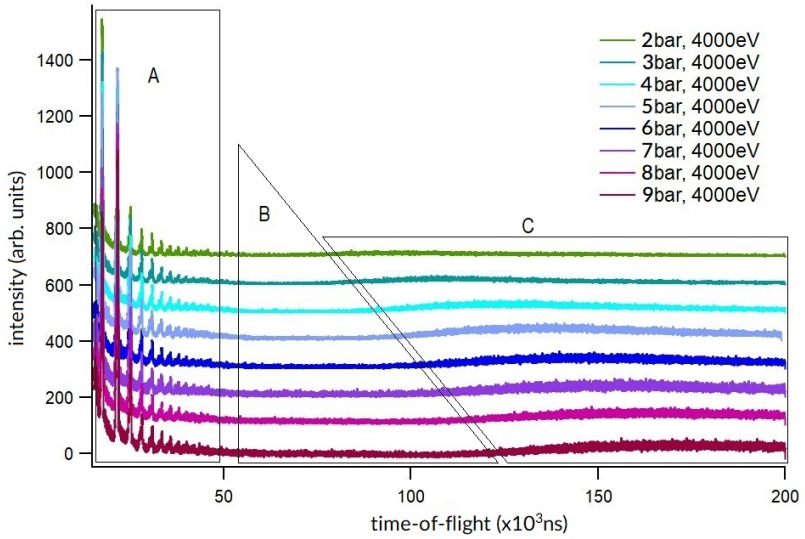

Figure 10: Time-of-flight spectra of xenon clusters. All the measured xenon spectra are scaled with respect to the dimer peak. Different parts of the spectra are labeled in A, B and C.

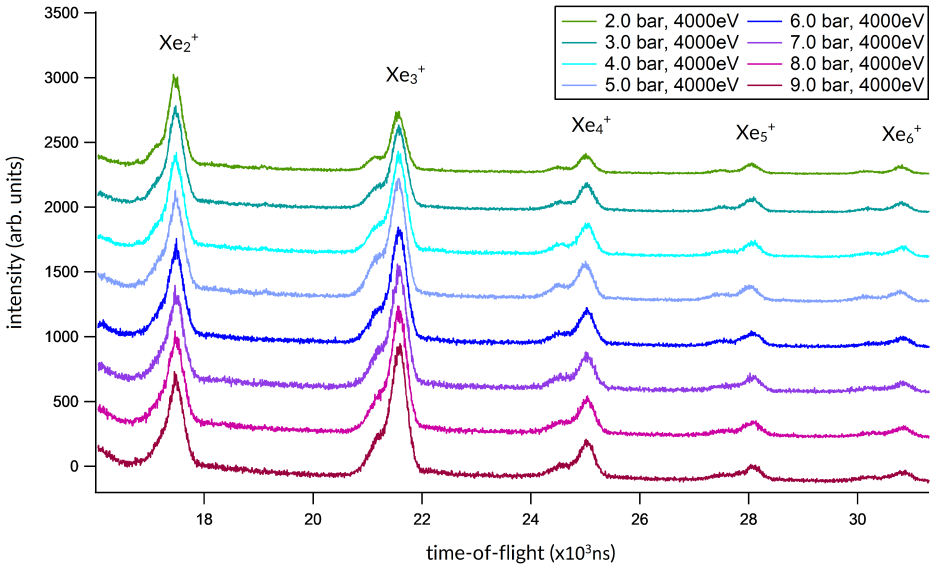

Figure 11: Relative changes between dimer, trimer, 4-mer, 5-mer, and 6-mer peaks at different expansion pressures.

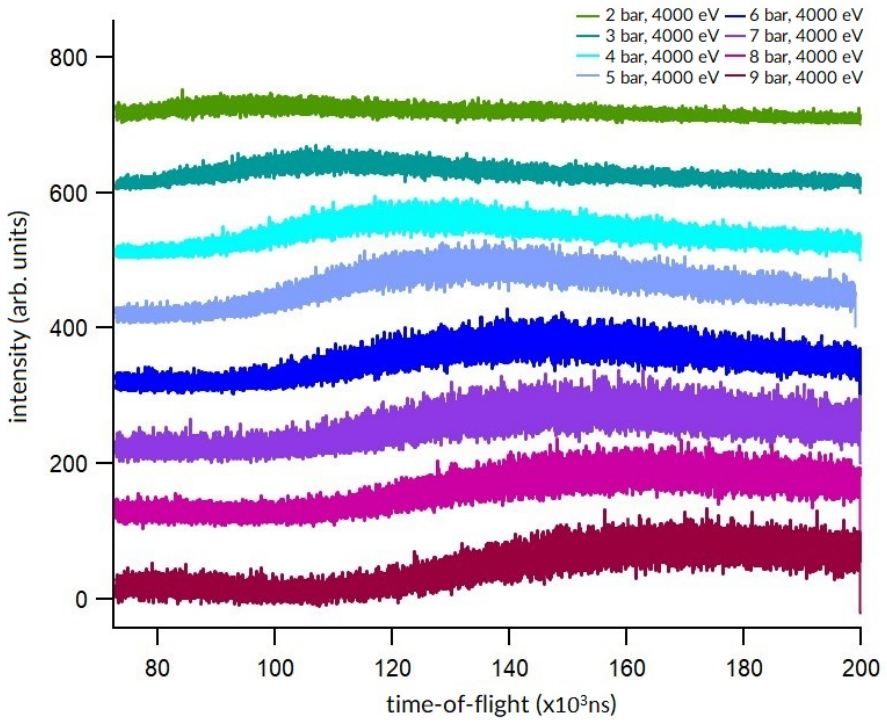

Figure 12: The structure of the spectra at higher flight times. Spectra shown above corresponds to part C presented in figure 10.

From the figure 11 the changes in relative abundancies between dimer Xe_2^+ and trimer Xe_3^+ peak intensities can be seen as the expansion pressure changes. The lower the expansion pressure the bigger the dimer peak is with respect to the trimer peak. In fact, dimer peak is larger than trimer peak only in the spectra measured using the pressure 2.0 and 3.0 bar. For higher pressures trimer peaks are bigger than dimer peaks. This same feature can be seen even more clearly from the figure 13. In addition, as the fragment size increases the intensity of the peak decreases as can be seen from both the figures 11 and 13.

According to the size models, high expansion pressure corresponds to the higher cluster size [30]. Therefore, the chart 13 suggests that the larger the initial clusters are the higher the relative abundancies with respect to dimer peak are for a given fragment. This can be seen from the peaks Xe_3^+, Xe_4^+ and Xe_8^+, in which always the peak corresponding to the highest pressure has the highest relative intensity. In other words, for lower pressures the relative contribution from dimers is relatively higher. However, this is not absolute. In peaks Xe_5^+, Xe_9^+, Xe_{10}^+, Xe_{11}^+, and Xe_{12}^+ the relative maximum corresponds pressures 5.0 and 6.0 bars. The inconsistencies to the trend may be due the certain initial cluster size and the fragmentation process. Perhaps the structures at 5.0 bar and 6.0 bar pressures are favorable for dissociating into 5-, 9-, 10-, 11-, and 12-atom fragments. However, the more probable reason for the inconsistencies may be the inaccuracies in the fitting.

As the expansion pressure grows the size of the formed clusters should grow according to the size models presented in chapter 2.5 [30]. This is the case also in the measured spectra here as can be seen from the figures 10 and 13. The change in dimer-trimer relation as a

function of expansion pressure suggests that the cluster size indeed grows as a function of pressure.

Part B in the spectra shown in figure 10 describes the low intensity part. From part B clear cluster peaks could not be separated. The length of the B part depends clearly on the expansion pressure and therefore the cluster size. The length of the B part increases as the expansion pressure increases. A wide feature at the end of the spectra is labeled as C in the figure 10. From this spectral part individual peaks cannot be recognized. However, there are several features that change as a function of pressure.

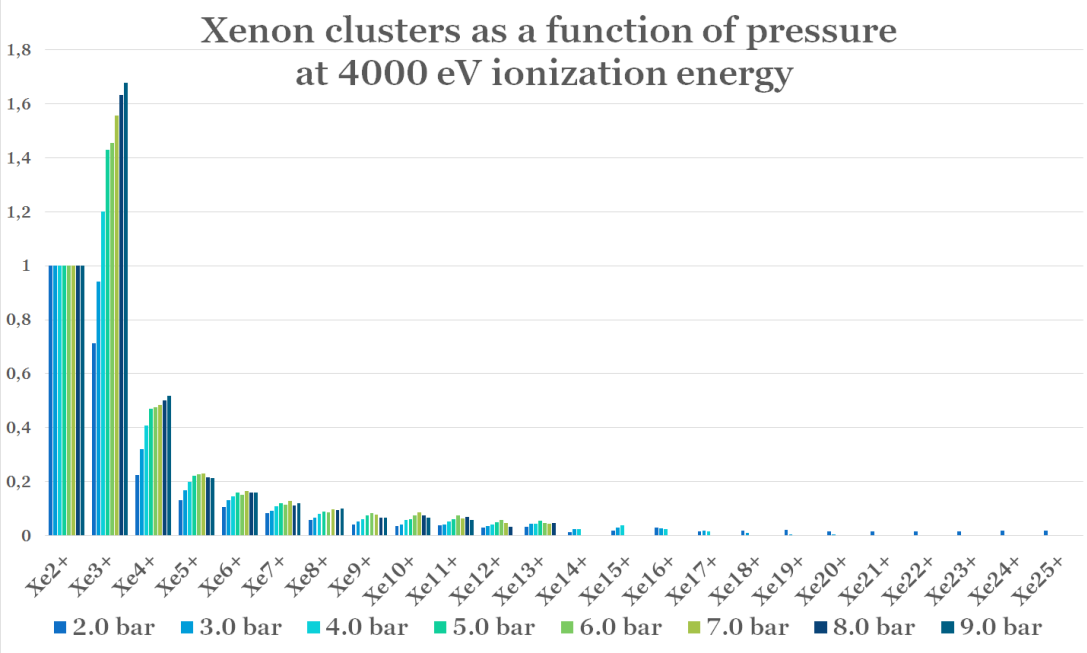

Figure 13: A chart describing relative areas of the fitted peaks from the original cluster spectra. All spectra are scaled respect to the dimer. For pressures 2.0 and 3.0 bars, the dimer peak is the highest, while for pressures 4.0 to 9.0 bar the trimer peak has the highest intensity. As the expansion pressure increases more abundant a given fragment is with respect to the dimer.

As the expansion pressure increases the intensity of the wide feature increases. In addition, the feature is wider at higher expansion pressures, thus the ends of the wide features are not seen completely for the pressures 3.0 to 9.0 bar. As the expansion pressure decreases the intensity maximum for the peak is found at shorter flight times. In figure 12 the changes in the C part of the xenon spectra can be seen more clearly.

The bimodal structure in the spectra is quite interesting. Therefore, the next calculation is derived to ensure the maximum fragment sizes that are possible to detect in the xenon measurements in question. The positive pulse length in extraction region was $5.5\mu s$ and the voltage 455 V. The maximum sized cluster fragment that can leave the extraction region in $5.5\mu s$, and reach the detector, can be calculated using equation 34. Approximations such as to set initial kinetic energy at zero are made. Now the calculation for maximum fragment

size that reaches the acceleration region is presented below. Relation $E_{ER} = q\|\overrightarrow{\mathrm{E_{ER}}}\|L_{ER} = qV_{ER}$ is used in calculations, where V_{ER} is the potential across the extraction region and L_{ER} the length of the extraction region. [43]

$$m = \frac{T_{ER}^2 q V_{ER}}{2sL_{ER}} = \frac{(5.5\mu s)^2 \cdot 1.602 \times 10^{-19} C \cdot 455V}{2 \cdot 0.008m \cdot 0.016m} = 8.613 \times 10^{-24} kg \tag{40}$$

The result above corresponds to fragment Xe_{40}^+, so the length of the pulse in the extraction region does limit the possible larger fragments to arrive to the detector. After the positive pulse a $201\mu s$ and $120V$ negative pulse is applied. Since the voltage of the negative pulse is lower compared to the positive pulse, some ions may get through the extraction region during the negative pulse. These ions may be seen at longer flight times and therefore cause the bimodal structure seen in part C. The wide feature in part C can also be some equipment related artefact.

4.1.2 Energy dependency

Two measurement series were measured as a function of ionization energy with two different pressures. At 6.0 bar pressure spectra using 5000, 600, 180, and 120 eV ionization energies were measured. At 1.5 bar pressure measurements were done using the ionization energies of 5000, 4000, 800, 180, and 120 eV. At 6.0 bar pressure the theoretical cluster size is 90 atoms and at 1.5 bar spectra the theoretical size is 9 atoms according to U. Buck and R Krohne [30]. Measurement series for both pressures are presented in whole in the figures 14 and 17.

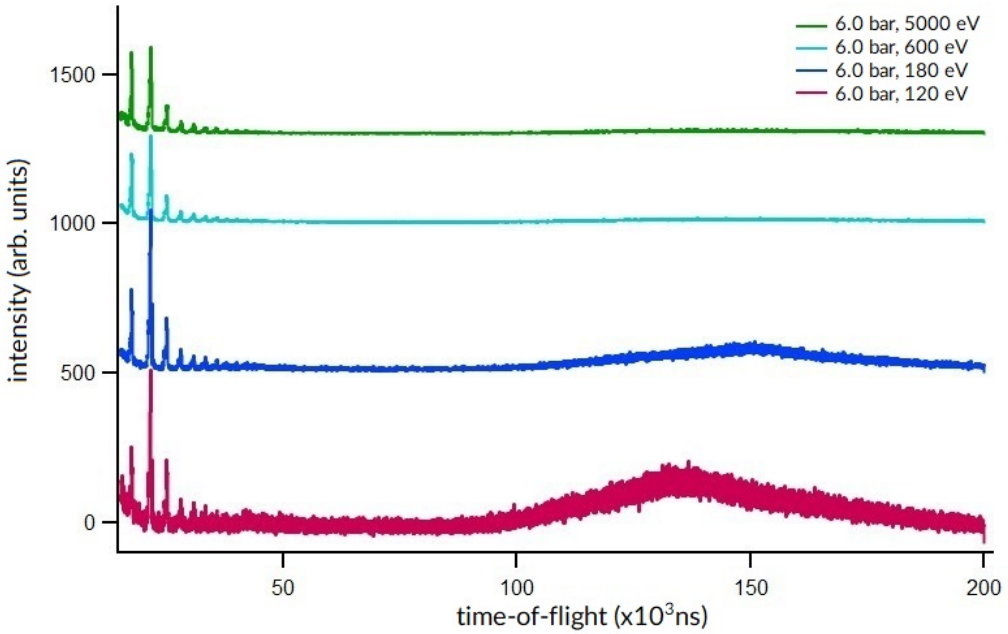

Figure 14: Time of flight spectra of xenon clusters at ionization pressure 6 bar. In figure 14, the whole spectra are presented. The structure of the spectra is bimodal.

The structure of the spectra in figure 14 is bimodal. As was stated in section 4.1.1 the wide feature in the spectra is not a correct cluster related result. The spectra are relatively similar on flight times under $50 \times 10^3 ns$.

In figure 15 dimer, trimer and 4-mer peaks are examined more closely. Peaks are scaled to the dimer peak. Spectra measured using 5000 and 600 eV ionization energy are very similar and differ from the spectra of 180 and 120 eV energies. This is a consequence of the ionization threshold energies in xenon atom. Significant ionization thresholds for xenon atoms respect to chosen ionization energies are for $2p_{3/2}$ shell 4786 eV, $4s$ shell 213.2 eV, $4p_{1/2}$ 146.7 eV and $4d_{3/2}$ 69.5 eV [35,45]. In the study of A. N. Arseniev [46] xenon clusters are studied in a supersonic beam under electron ionization. According to A. N. Arseniev et al. there are no bimodal structure in the xenon spectra. In their study the peak intensity in the mass spectra decreases as the cluster size increases. [46]

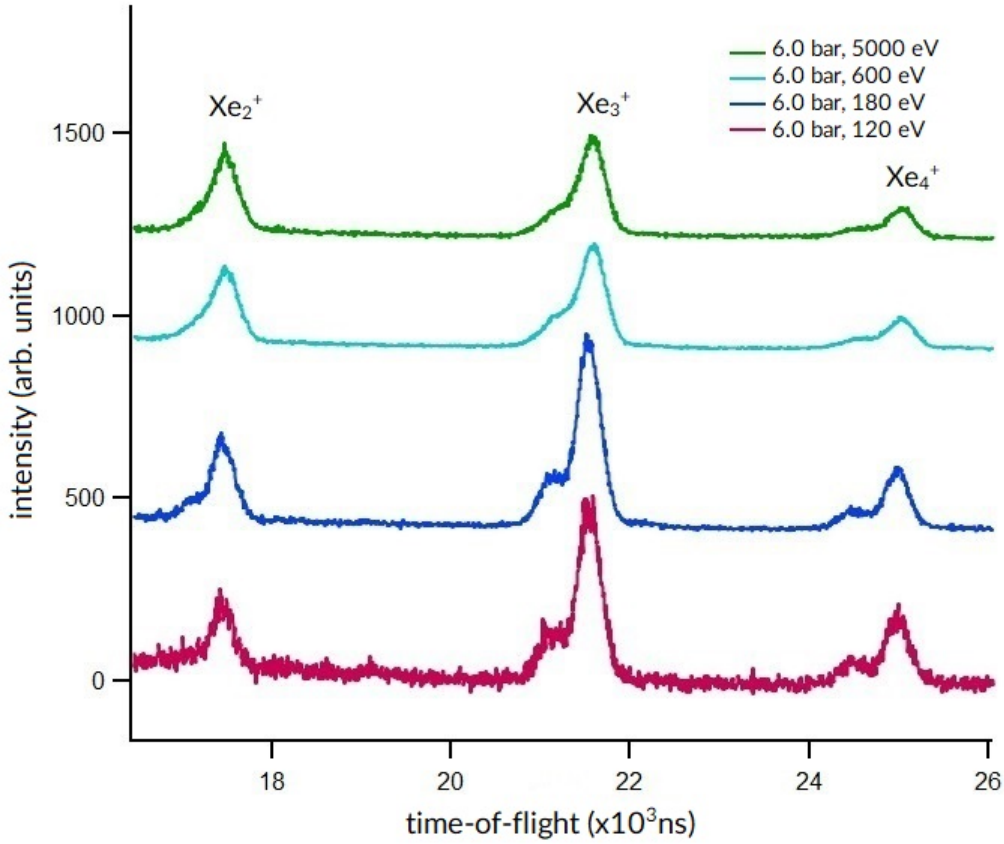

Figure 15: Time-of-flight spectra of xenon clusters at expansion pressure of 6.0 bar concentrating on the details of Xe_2^+, Xe_3^+ and Xe_4^+ peaks from the spectra presented in whole in figure 14.

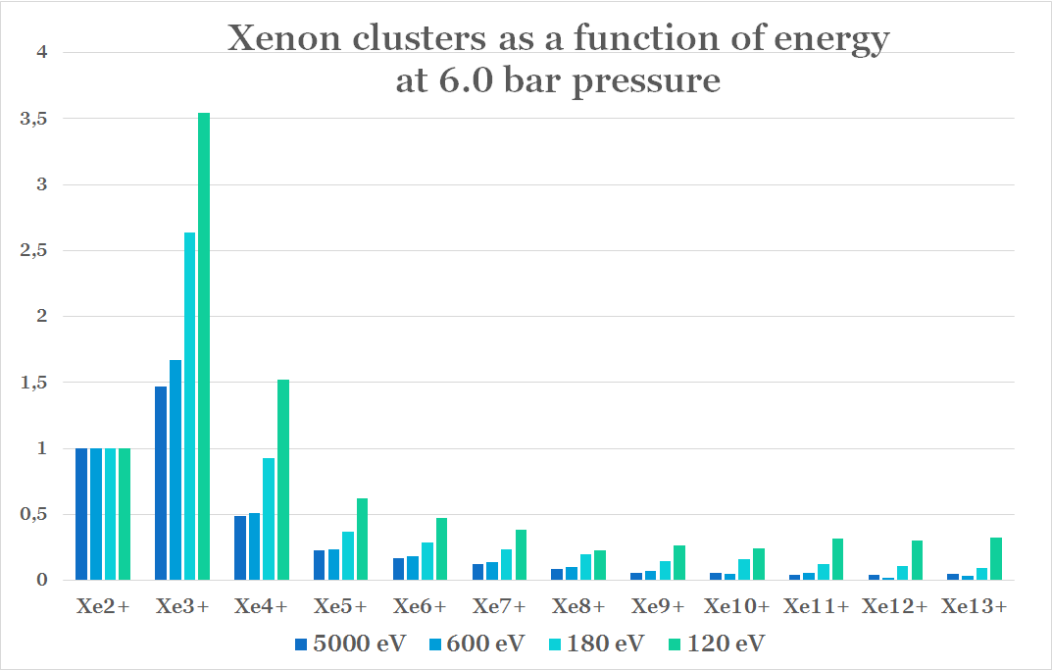

Figure 16: A chart describing the measured relative intensities of the cluster peaks from the spectra 14. Peaks are scaled to dimer peak. Within a given fragment, the relative peak intensities increase as the ionization energy decreases. However, there is exceptions to the trend in 10-mer, 12-mer and 13-mer peaks, where the intensities from 5000 eV spectra are higher than the intensities from 600 eV spectra. In addition, the peak intensities decrease as the fragment size increases.

In every spectrum, a dimer peak is smaller than a trimer peak. At small energies 180 and 120 eV the relative difference between the dimer and trimer peaks is bigger than at higher energies. At 180 and 120 eV spectra the 4-mer peak is relatively higher than in 5000 and 600 eV spectra. Also, the double peak differentiates more strongly in the lower ionization energy spectra. The relations between dimer, trimer and 4-mer peaks are shown also in figure 16.

For higher ionization energies the intensity of the wide feature is lower as is shown in figure 14. The intensity maximum in 120 eV spectra is in lower flight time than the intensity maximum in 180 eV spectra. In figure 16 the measured peak areas of the spectra 14 are shown. In each spectra the trimer peak is the highest peak as was seen also from the figure 15. In 120 eV spectra also 4-mer peak is larger than the dimer peak. Apart from the dimer peak, the peak area decreases as the fragment size increases. However, some small inconsistencies can be seen from 8-mer, 9-mer and 10-mer peaks. The inconsistencies are that small that they may be due the fitting error.

The trend in 5000 and 600 eV spectra is very similar even though the difference in ionization energy is relatively large. The differences in peak intensities between 180 and 120 eV spectra are relatively larger even if the ionization energy difference is smaller. The smaller the ionization energy the larger the relative abundancies are for a given fragment. At higher ionization energies, there are relatively more smaller fragments. Presumably,

the lower ionization energy causes less fragmentation, while higher ionization energy causes clusters to fragment into smaller fragments.

Figure 17 shows the spectra measured at 1.5 bar pressure. The structure of the spectra is bimodal. At flight times under $50 \times 10^3 ns$ strong and narrow cluster fragment peaks are seen when for longer flight times a wide feature is measured as in the spectra presented before. Compared to series measured at 6.0 bar pressure, at 1.5 bar pressure the series is more uniform.

In figure 18 dimer, trimer and 4-mer peaks of the spectra 17 are shown in detail. In each spectra the dimer peak is the highest peak. The high intensity of the dimer peak could be due the fact that in 1.5 bar pressure the formed clusters are very small [30]. If the formed clusters are small, the fragments caused by electron impact are also small. The intensity difference between dimer and trimer peak decreases as the ionization energy decreases. For 4-mer peaks the same trend can be recognized.

In figure 19 the peak intensities of the spectra, shown in figure 17, are presented in detail. As was already seen from the figure 18 the highest peak in every pressure is the dimer peak. As the size of the fragment increases the peak intensity decreases. However, the 14-mer and 15-mer peaks are exceptions for that trend. These may be due the fitting errors since the error is relatively small. In addition, from the figure 19 can be seen that the relative abundancy increases as the ionization energy decreases for a given fragment. Although the spectra measured at 800 eV ionization energy is not in line to other results. This may be due a measurement error.

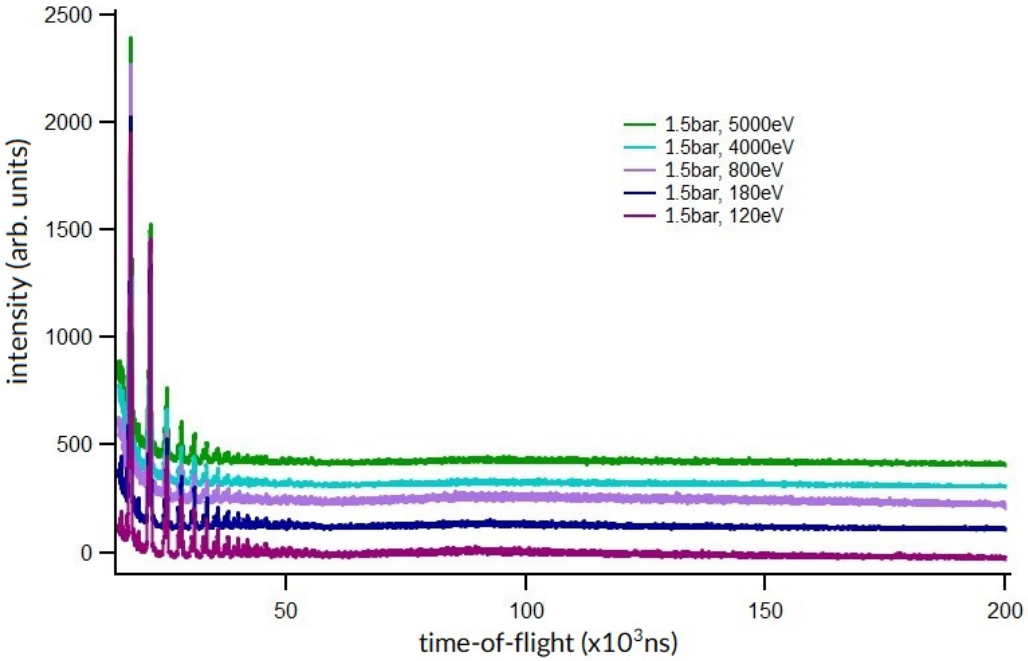

Figure 17: The whole measurement series of xenon at 1.5 bar pressure is shown. The structure of the spectra is bimodal.

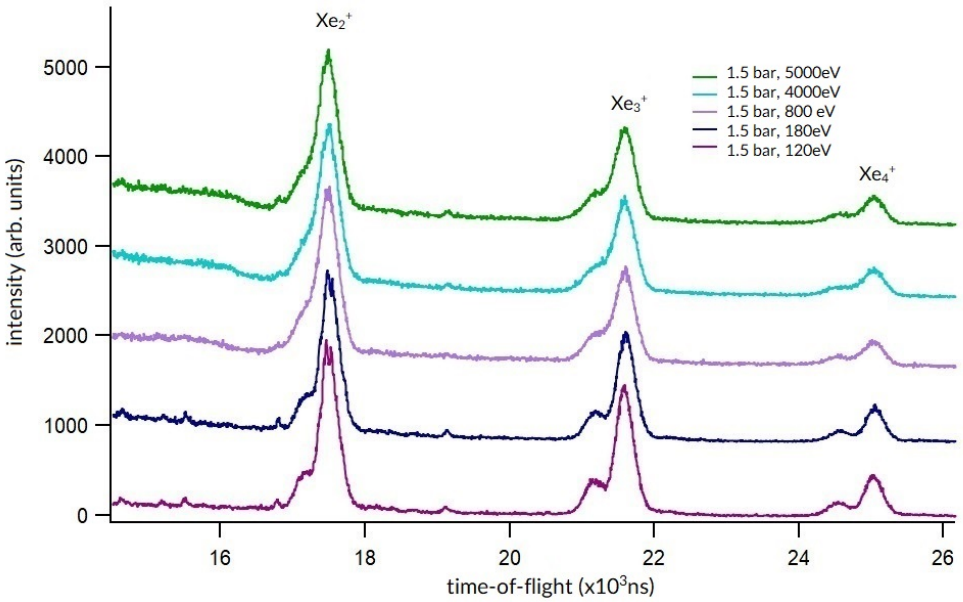

Figure 18: Dimer, trimer, and 4-mer peaks of the spectra presented in figure 17 are shown in detail. The peaks are scaled to dimer peak. As the ionization energy decreases the double peak effect gets stronger. For higher ionization energies the relative difference between dimer and trimer peak is bigger.

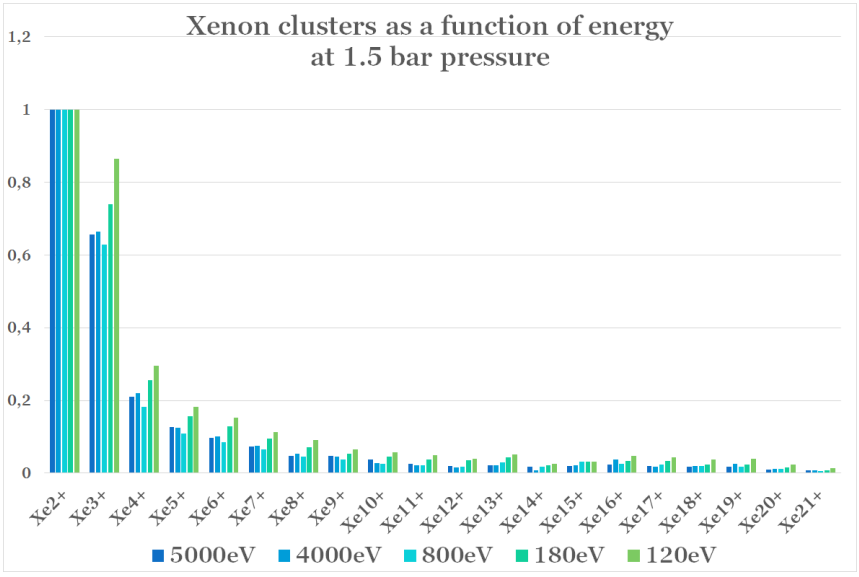

Figure 19: A chart to describe the relative abundancies calculated from the spectra 17 for a given fragments. The abundancies are scaled with respect to the dimer peak, which is set to 1.

4.1.3 Double peaks in xenon spectra

In the xenon cluster spectra, a clear double peak structure can be seen as in figures 11, 15 and 18. The double peak structure is clearer for larger fragments. In the dimer peak the double peaks overlap strongly. Also, for lower ionization energies the double peak structure is stronger as can be seen from figures 15 and 18.

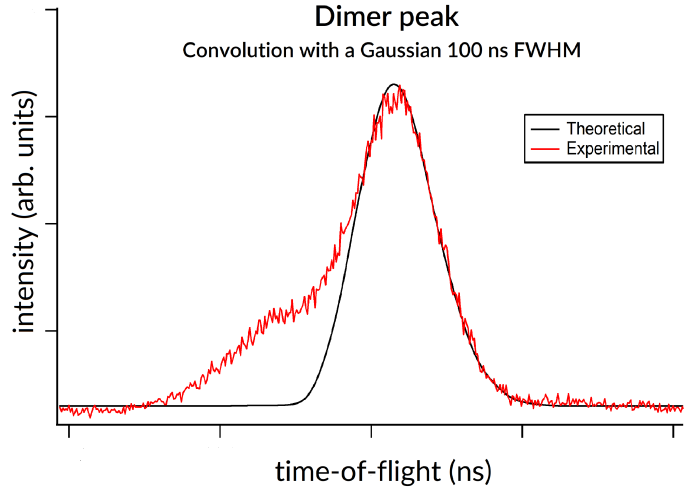

(a)

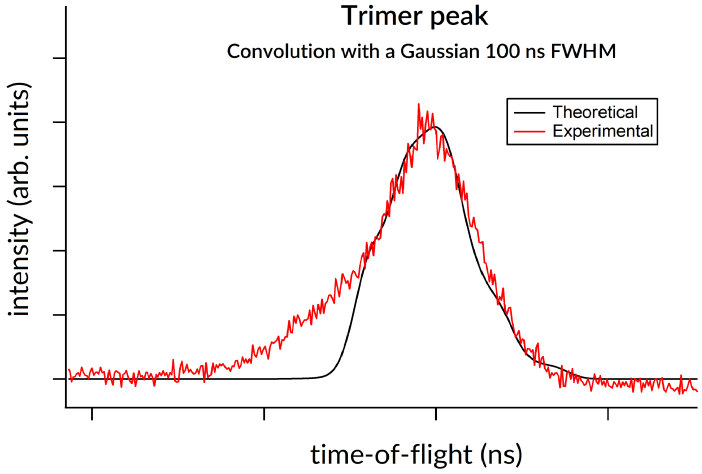

(b)

Figure 20: Theoretically calculated peaks to simulate the isotope distribution in xenon clusters compared to experimentally measured peak. In figure 20a the theoretical and experimental dimer peaks are presented when figure 20b describes similarly the theoretical and experimental trimer peaks.

The double peak structure could be explained by the large amount of xenon isotopes. Therefore, a theoretical isotope distribution was calculated to dimer and trimer peaks using the relative probabilities and masses for each 9 isotopes of xenon [45]. In the model every possible isotope combination was formed, and their masses calculated. Also, probabilities for each combination were calculated using the natural abundances given in literature [45]. Using the masses of the isotopes theoretical flight times were calculated using the formula 39. Via theoretical flight times and cluster abundance probabilities, a theoretical peak was formed for xenon dimer and trimer as convolution with a Gaussian 100 ns FWHM. The resolution of the spectrometer determines the used width 100 ns FWHM in calculations. Theoretical results are presented in the figures 20a and 20b.

From both figures 20a and 20b it can be seen that the shape of the peak does not correspond to experimental shapes of dimer and trimer peaks. The theoretical and experimental peaks are plotted in same figure for comparison. Therefore, it is possible that the double peak structure cannot be explained by xenon isotopes.

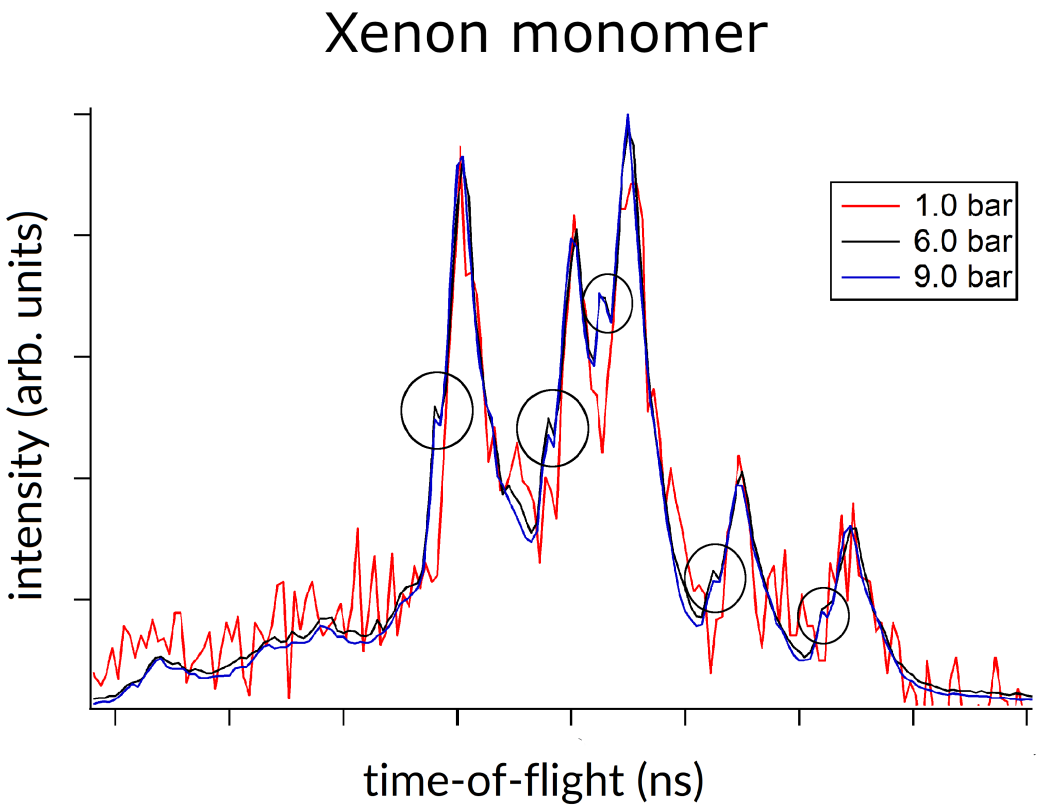

Figure 21: The double peak comparison in xenon monomer at three different pressures. Spectra measured at 6.0 and 9.0 bar pressure have clusters, while the spectra measured at 1.0 bar pressure does not have clusters. The differences in double peak structure in the spectra are pointed out in circles.

It is important to solve whether the double peak structure is at all cluster related phenomena. It is possible is that the double peak structure is just some artefact caused by measurement equipment. In figure 21 a singly charged xenon monomers Xe^+ at different expansion pressures are shown. The spectra measured at 6.0 bar and 9.0 bar pressure include clusters when the spectra of 1.0 bar pressure have no clusters. The spectra for xenon monomer at pressures 6.0 and 9.0 bar are similar and the double peak structure is possible to detect also from the monomer peak. The spectra measured at 1.0 bar pressure differs from the other two, because the double peak structure cannot be seen. This result could indicate that after all the double peak structure is some cluster related feature. However, anything sure cannot be said since the statistics in 1.0 bar spectra is worse compared to 6.0 and 9.0 bar spectra which may naturally affect to the results. The possible cluster related double peak structure could be a cause of the differences in the fragmentation processes. Possibly the fragmentation process may affect to the initial energies of the fragments that can be seen in a double peak structure in the spectra.

4.2 Argon clusters

For argon, four mass spectroscopy measurement series were measured. Two of them were measured as a function of expansion pressure at constant ionization energy when the other two were measured as a function of ionization energy at constant expansion pressure. In addition, triple ion coincidence measurements were measured for argon at two different expansion pressures. In comparison to xenon cluster spectra a bimodal structure is not seen from argon spectra.

Theoretically calculated cluster sizes for argon clusters at different pressures used in measurements are presented in Table 5. Sizes are calculated using the model derived by U. Buck and R Krohne [30].

Table 5. Mean argon cluster sizes as a function of pressure according to U. Buck and R. Krohne

Pressure	3.0 bar	4.0 bar	4.4 bar	5.0 bar	6.0 bar	6.6 bar	6.8 bar
Cluster size	13	23	28	38	58	73	79

For argon the maximum fragment size that can be properly measured can be calculated in a same way as for xenon clusters. The positive pulse length in extraction region was $4.5\mu s$ and the voltage 349 V during the argon cluster measurements.

$$m = \frac{T_{ER}^2 q V_{ER}}{2 s L_{ER}} = \frac{(4.5\mu s)^2 \cdot 1.602 \times 10^{-19} C \cdot 349 V}{2 \cdot 0.008 m \cdot 0.016 m} = 4.423 \times 10^{-24} kg \qquad (41)$$

The result above corresponds to fragment Ar_{66}^+. The result means that the length of the positive pulse limits the measurements of only the largest of fragments.

4.2.1 Pressure dependency

Pressure dependency in argon clusters was studied using 3.0, 4.0, 5.0, 6.0, and 6.8 bar expansion pressures. One series was measured at constant ionization energy of 4000 eV and the second series was measured at constant ionization energy of 20 eV.

Spectra showing pressure dependency at 4000 eV ionization energy is presented in figure 22. The spectra measured in different pressures are relatively similar. Only the spectra of

3.0 bar pressure differs significantly from the other. However, the largest difference is found in the shape of the background. In spectra of 3.0 bar pressure the background rises as the flight times decreases. In addition, some background peaks are seen only from the 3.0 bar spectra.

In figure 23 the peak intensities are presented with scaling to the dimer peak. Small differences can be seen between the spectra of different pressures due to data fitting. In the figure 23 the fragment size increases as the peak intensity decreases. The decrease of peak intensity between dimer and trimer peaks and trimer and 4-mer peak is very steep. However, the decrease of peak intensities from 5-mer peak to 24-mer peak is gentle. 15-mer peak and 20-mer peaks are relatively lower to neighbor peaks. The largest peak in every spectrum is the dimer peak.

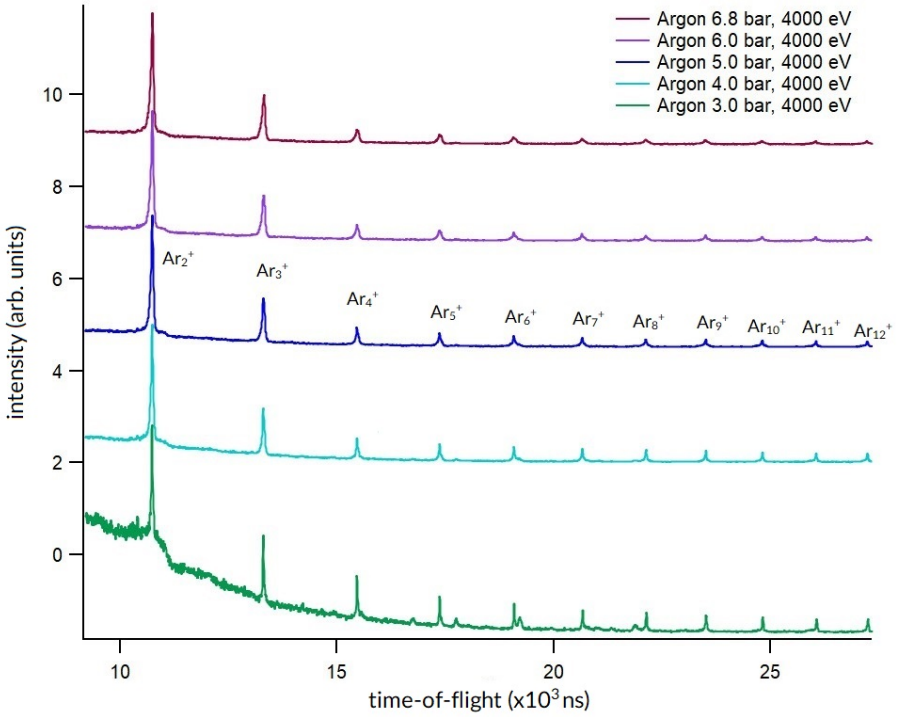

Figure 22: Argon clusters measured as function of expansion pressure at constant ionization energy of 4000 eV. The peaks are scaled to the dimer peak. The differences between 6.8 bar to 4.0 bar spectra are so small that they cannot be detected straight from the spectra. Relative peak intensities are presented in figure 23 for more accurate review.

As was already seen from the figure 22, the 3.0 bar spectrum differs from the other spectra. The same feature is seen also from the chart 23. The peak intensities in 3.0 bar spectra are relatively more intense compared to other pressures. All in all, as the expansion pressure increases the relative peak abundancies with respect to the dimer decrease for a given fragment. Interestingly this does not apply to trimer peak. The peak intensities of trimer peak in different pressures are almost equal in every pressure.

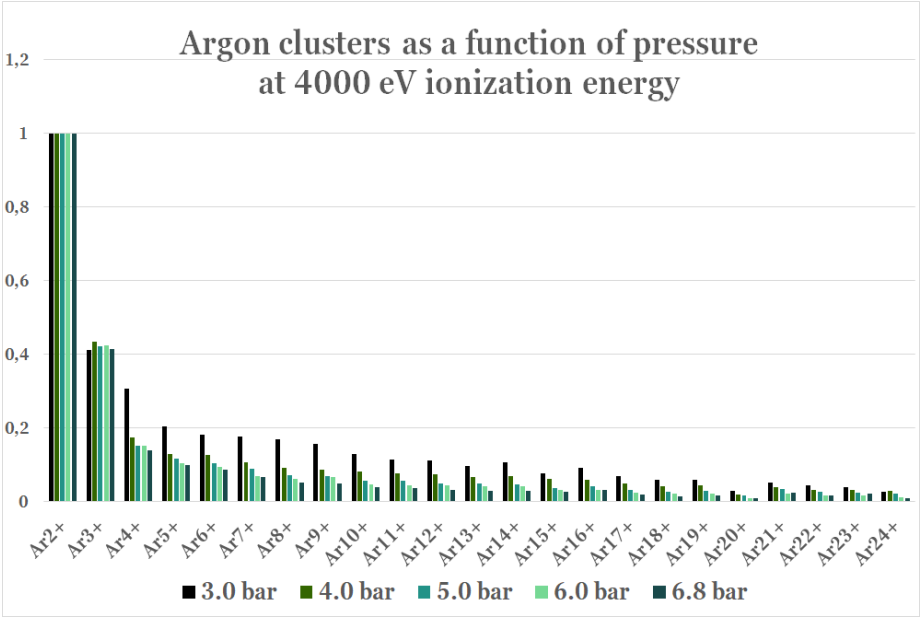

Figure 23: Relative abundancies of argon cluster fragments of original spectra 22.

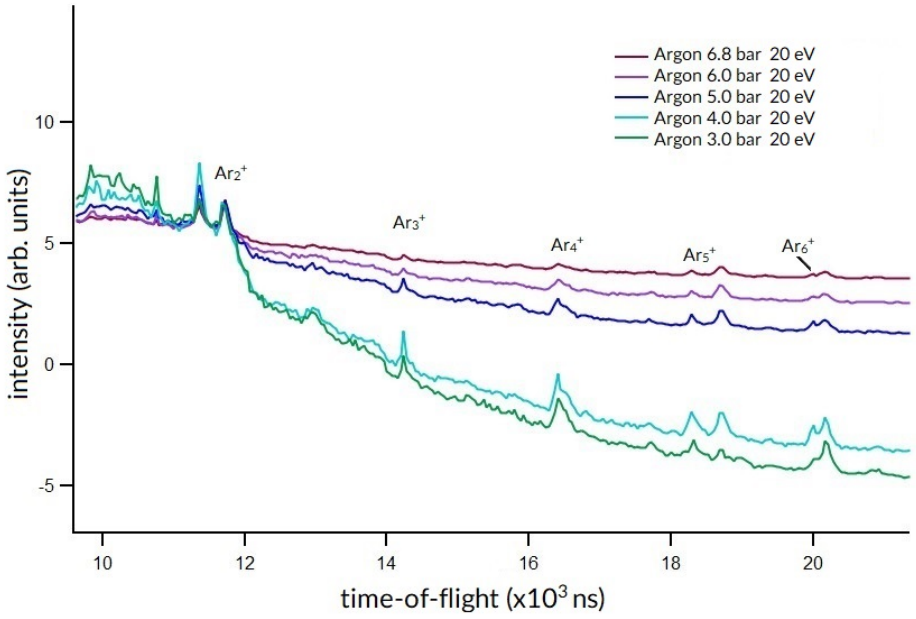

Figure 24: The spectra of argon clusters measured as a function of expansion pressure at constant ionization energy of 20 eV. The spectra are scaled to dimer peak. Spectra 3.0 and 4.0 bar are quite like each other when the spectra 5.0, 6.0, and 6.8 bar remind of each other. These same results can be seen also in the calculated chart presented in the figure 25.

The figure 24 presents the original spectra of the measurements as a function of pressure at constant ionization energy of 20 eV. The comparison between spectra of different pressures is rather difficult due the large differences between backgrounds. In addition, the peaks in every spectrum are very low. Spectra measured using expansion pressures 3.0 and 4.0 bar are relatively uniform when the spectra measured at pressures 5.0, 6.0, and 6.8 bar are similar. The largest differences between lower- and higher-pressure spectra are in the shape of the background and peak intensities. In pressures 3.0 and 4.0 bars the peak intensities and the changes in background are more intense compared to higher pressures.

Peak areas of the spectra 24 are shown in figure 25. The chart shows the relative peak areas. For easier comparison, the peaks are scaled to dimer peak. In every pressure the dimer peak is the highest peak. So as the size of the fragment increases the peak intensity decreases. Although there are many exceptions to that trend: 4-mer peak is higher than trimer peak, 10-mer peak is small compared to neighbor peaks, and 21-mer peak is higher compared to neighbor peaks. In addition, the calculations confirm the same feature that was already seen from the spectra 24. The 3.0 and 4.0 bar results are uniform and differ from the spectra measured at pressures 5.0, 6.0, and 6.8 bar. In addition, the peak abundancy decreases as a function of a increasing pressure for a given fragment.

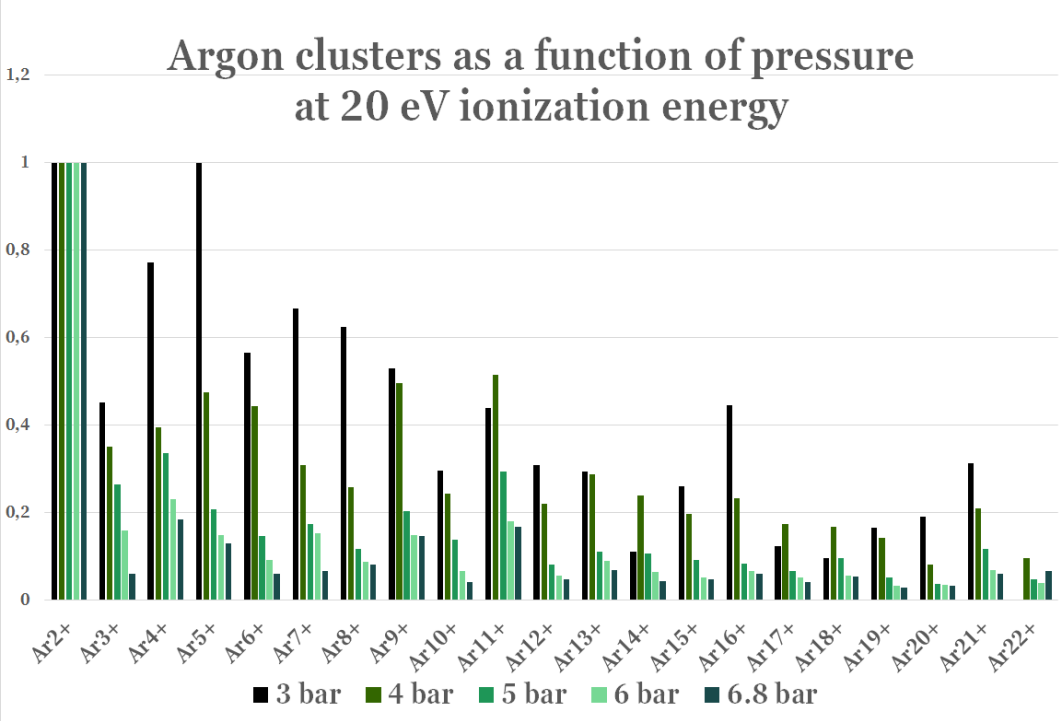

Figure 25: Relative abundances of argon cluster fragments as a function of a pressure at constant ionization energy of 20 eV.

The trends that can be found from spectra of 4000 and 20 eV are similar. In both series the peak intensity decreases as the fragment size increases. However, there is a lot more inconsistency in the results of 20 eV spectra compared to the results of 4000 eV spectra.

The irregular results measured at 20 eV ionization energy suggest that the electron gun does not necessarily work properly at low energies. In addition, as the expansion pressure increases the more abundant a given fragment is with respect to the dimer peak. This result can be interpreted to mean that either larger clusters produce smaller fragments, or the large fragments are neutral or negatively charged and therefore are not seen in the spectra. According to size model by U. Buck and R. Krohne [30] the cluster size increases as a function of expansion pressure as was stated before. Therefore, the presumption is that as the initial cluster size increases the fragment size should increase too. However, for argon the result is exactly opposite.

4.2.2 Energy dependency

The ionization energy dependency in argon clusters was measured at two different expansion pressures of 4.0 and 6.8 bar. For 6.8 bar pressure the used ionization energies were 300, 200, and 20 eV, when for 4.0 bar pressure 300, 200, 70, and 20 eV spectra were measured.

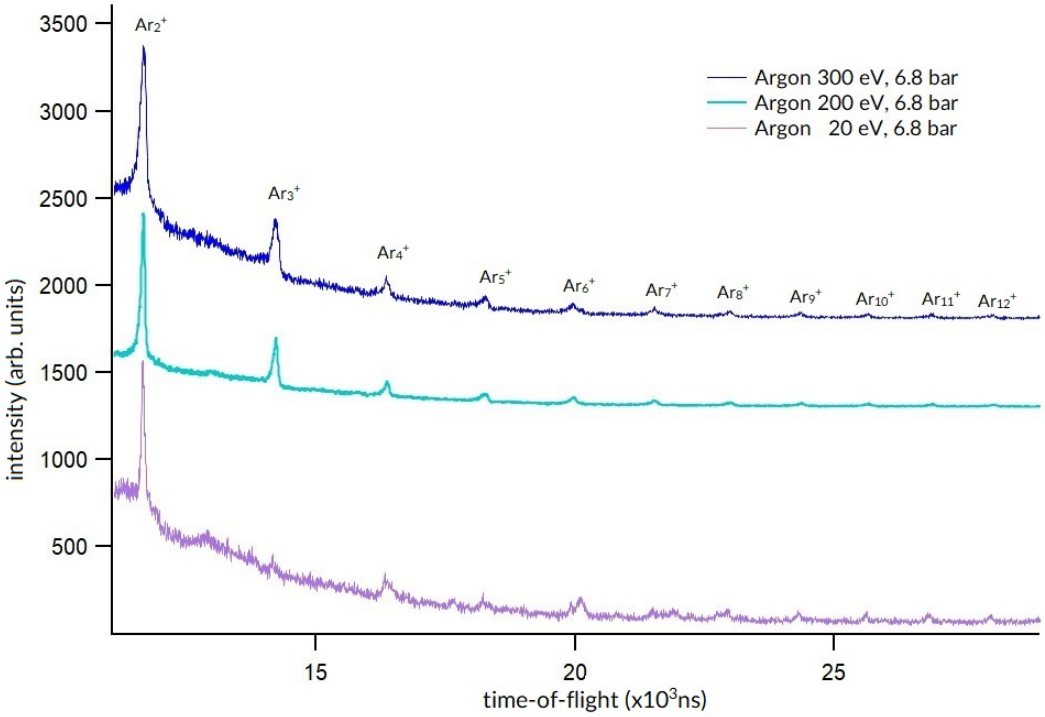

Figure 26: Argon cluster measurements as a function of ionization energy. The peaks are scaled to dimer peak. Spectra of 20 eV has smaller trimer peak compared to 300 and 200 eV spectra. In every spectrum there are differences in the background.

In figure 27 the original spectra measured at 6.8 bar pressure are presented. The spectra measured using 300 and 200 eV are more similar in comparison to spectra measured at ionization energy of 20 eV. The spectrum of 20 eV lacks almost completely the trimer peak when the spectra of 300 and 200 eV the trimer peak is the second highest. In addition, there

is a difference in the shape of the backgrounds. In 20 eV spectra the background descends the deepest. The flattest background is in the spectra of 200 eV. From 20 eV spectra clear background peaks can be seen.

The chart in figure 28 describes the peak intensities of the original spectra shown in figure 27. Peak areas in 300 and 200 eV spectra are very similar but differ from 20 eV spectra. For a given fragment, as the ionization energy increases the relative abundancies decrease with respect to dimer peak. However, there is quite many peaks where the area from 200 eV spectra is lower compared to 300 eV peak. In addition, in trimer and 5-mer peaks the 20 eV -peak is the lowest. In every spectrum in chart 28 the dimer peak is the highest peak. The fragment size increases as the peak area decreases. However, there are many irregularities to that trend. The lowest peak in 20 eV spectrum is 20-mer peak. 13-mer peak is also high in comparison to neighbor peaks when the 10-mer peak is relatively low. In the 200 eV spectra the peak height decreases without irregularities. In 300 eV spectra there is irregularities to be seen is 5-mer, 6-mer, 7-mer and 8-mer peaks. Also 20-mer peak at 300 eV is high compared to 20-mer peak at 200 eV peak.

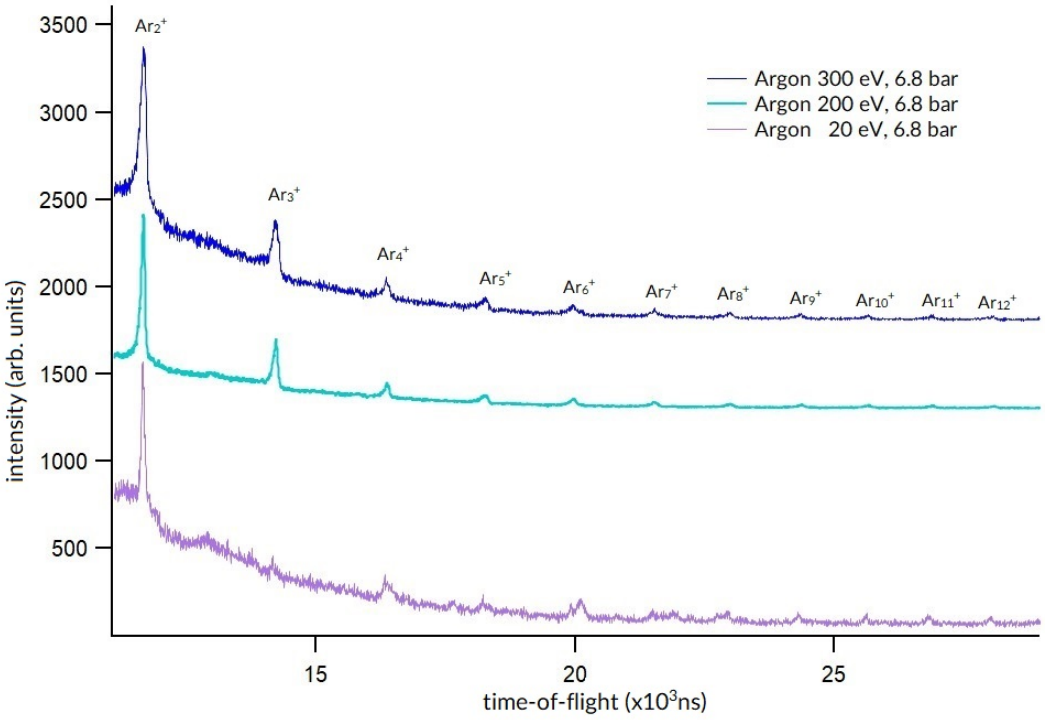

Figure 27: Argon cluster measurements as a function of ionization energy. The peaks are scaled to dimer peak. Spectra of 20 eV has smaller trimer peak compared to 300 and 200 eV spectra. In every spectrum there are differences in the background.

In figure 29 the original spectra of the measurements at constant expansion pressure of 4.0 bar is presented. Spectra measured using ionization energy of 300 and 200 eV are very similar when the spectra measured at ionization energy of 70 and 20 eV have the same

shape. As in the spectra measured at 6.8 bar expansion pressure presented in figure 27 the same background shape can be seen in the spectra measured using 4.0 bar expansion pressure. The background decreases steeper in energies 20 and 70 eV. The background in higher ionization energies 200 and 300 eV is flatter. However, the background in 300 eV spectra is stronger compared to 200 eV spectra. These are the same features that were found also from the spectra measured at 6.8 bar pressure.

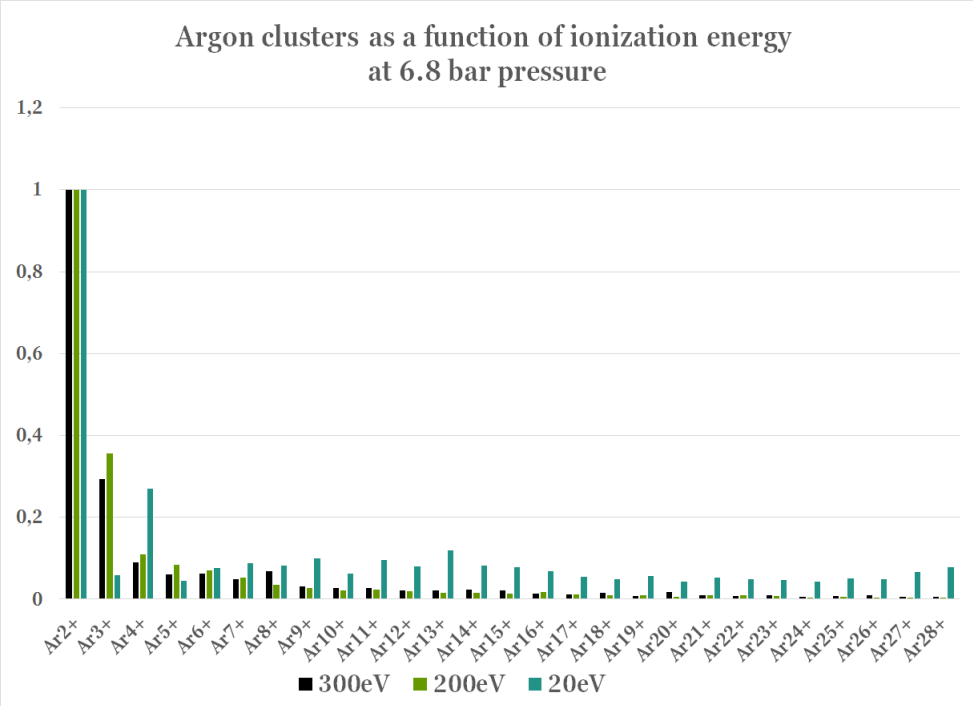

Figure 28: A chart describing the peak intensities of argon clusters at 6.8 bar pressure as a function of ionization energy.

A chart in figure 30 presents in detail the peak intensities of the spectra presented in figure 29. The results in the chart 30 confirm the similarities between 20 and 70 eV spectra and the similarities between the 200 and 300 eV spectra. In chart 30 for a given fragment the peak intensity increases as the ionization energy decreases. Also, the peak area decreases as the fragment size increases. These are the same phenomena that was found also in the chart 28. For both 6.8 and 4.0 bar pressures the trimer peak is lower than 4-mer peak at energies 20 and 70 eV. At energies 200 and 300 eV the decrease in the peak height as a function of increasing cluster size is consistent. In energies 20 and 70 eV there is irregularities for decreasing peak heights. In 70 eV spectrum there are inconsistencies in trimer, 5-mer, 6-mer, 7-mer, 8-mer, 9-mer, 10-mer, 11-mer and 12-mer peaks. The same peaks in 20 eV spectrum are irregular. In every energy the lowest peak is the 20-mer peak.

The results in measurements using 6.8 and 4.0 bar expansion pressures are very coherent. The largest difference between the measurements is the relation between the dimer peak to other peaks. Clearly in the results presented in figure 29 and 30 the relative height of dimer peak is lower compared to the relative height of the results presented in figures 27 and 28.

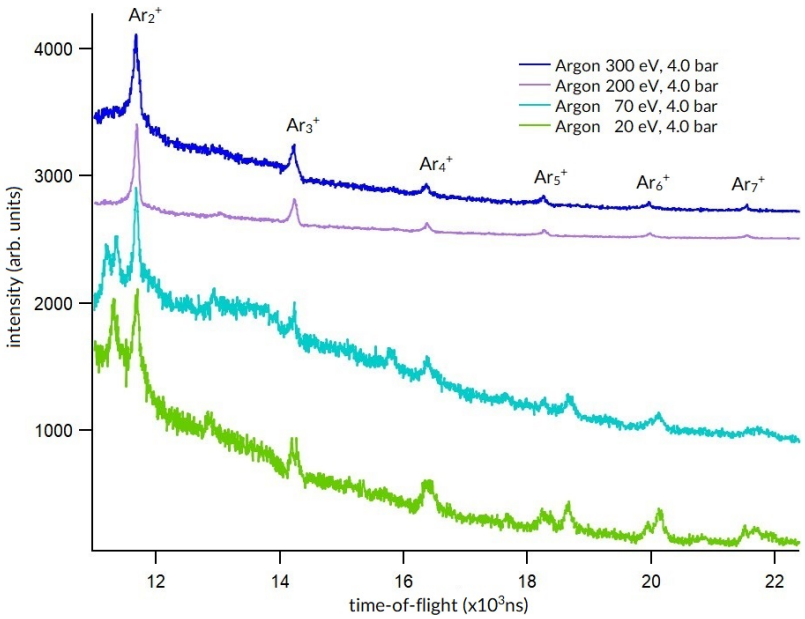

Figure 29: Argon clusters measured as a function of ionization energy at constant 4.0 bar pressure.

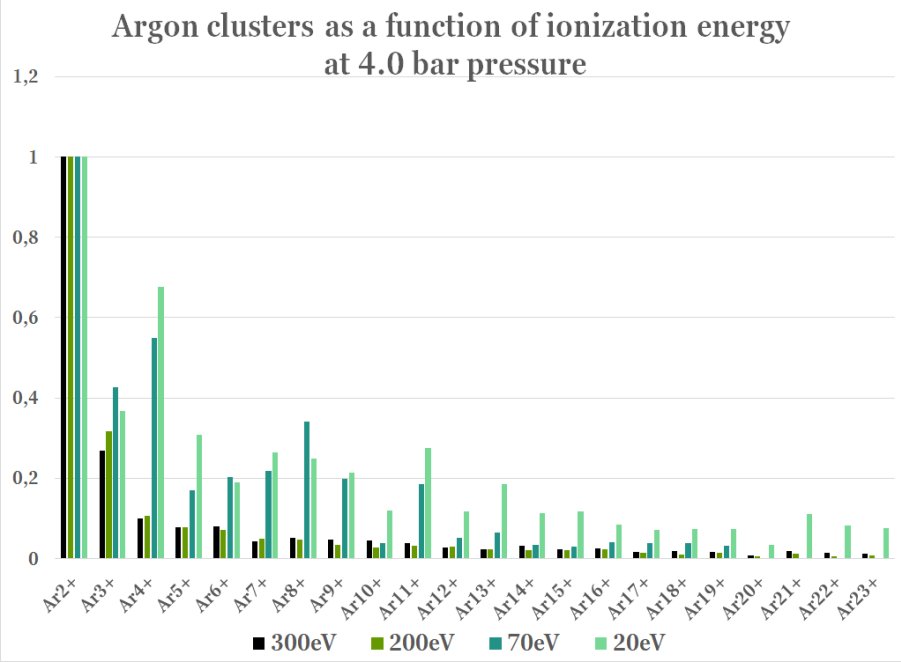

Figure 30: A chart of the calculated peak intensities of argon clusters at 4.0 bar pressure as a function of ionization energy.

4.3 Coincidence measurements

In coincidence measurements for argon clusters the fragments of same ionization process are detected. In figures 31 and 32 the measured coincidence maps are shown. Both spectra are measured using 4000 eV electron impact ionization at different pressures of 4.4 bar and 6.6 bar. The coincidence map measured at 6.6 bar is presented in figure 32 and for 4.4 bar in figure 31. The intensity of the peak (the number of counts) is described in color. The higher the intensity the more red the peak is. The lowest intensity is marked with dark blue. The scale is logarithmic.

In both maps there are several different peak series. These series are found at constant flight time separation of the first and second fragment but increasing flight time separation of the second and third peak. The peaks are recognized and marked in the coincidence maps 31 and 32. In the 4.4 bar spectra the lower number of counts is due the shorter measurement time.

In figure 31 seven different series are found. In y-axis there are three different series of form $Ar^+Ar^+Ar^+_{N_{1y}}$, $Ar_2^+Ar_2^+Ar^+_{N_{2y}}$ and $Ar_3^+Ar_3^+Ar^+_{N_{3y}}$, where $N_{1y} = 2, 3, 4, ...$, $N_{2y} = 3, 4, 5, ...$ and $N_{3y} = 4, 5, 6, ...$ From x-axis three different series of form $Ar^{+2}Ar^+_{N_{1x}}Ar^+_{N_{1x}}$, $Ar_2^+Ar^+_{N_{2x}}Ar^+_{N_{2x}}$ and $Ar^+Ar^+_{N_{3x}}Ar^+_{N_{3x}}$ are found. In the series $N_{1x} = 1, 2, 3, ...$, $N_{2x} = 3, 4, 5, ...$ and $N_{3x} = 2, 3, 4, ...$ The series found in the map continue outside. However, the intensity of the peaks outside the map is relatively low. The most intensive peaks in the y-axis are $Ar_2^+Ar_2^+Ar_3^+$, $Ar^+Ar_2^+Ar_2^+$ and $Ar^+Ar_3^+Ar_3^+$. In the x-axis the most intense peaks are $Ar^{+2}Ar^+Ar^+$, $Ar_2^+Ar_3^+Ar_3^+$ and $Ar^+Ar_2^+Ar_2^+$. The most intense peak in off-axis is $Ar^+Ar_2^+Ar_3^+$. In addition, there are four peak series in which the first ion is doubly charged argon monomer Ar^{2+}.

In figure 32 there are three different series in y-axis. These series are of form $Ar^+Ar^+Ar^+_{M_{1y}}$, $Ar_2^+Ar_2^+Ar^+_{M_{2y}}$ and $Ar_3^+Ar_3^+Ar^+_{M_{3y}}$, where $M_{1y} = 2, 3, 4, ...$, $M_{2y} = 3, 4, 5, ...$ and $M_{3y} = 4, 5, 6, ...$. In the x-axis there are three series of form $Ar^{+2}Ar^+_{M_{1x}}Ar^+_{M_{1x}}$, $Ar_2^+Ar^+_{M_{2x}}Ar^+_{M_{2x}}$ and $Ar^+Ar^+_{M_{3x}}Ar^+_{M_{3x}}$, where $M_{1x} = 1, 2, 3, ...$, $M_{2x} = 3, 4, 5, ...$ and $M_{3x} = 2, 3, 4, ...$. These are the same series that were found in coincidence map 31. The differences between the peaks are in the intensities. In spectra 32 the series are more intense and therefore more peaks of the series can be recognized. This is due the difference in the number of counts in display. The most intensive peaks in coincidence map 32 are $Ar_2^+Ar_2^+Ar_3^+$, $Ar^+Ar_2^+Ar_2^+$ and $Ar^+Ar_3^+Ar_3^+$, $Ar^{+2}Ar^+Ar^+$, $Ar_2^+Ar_3^+Ar_3^+$ and $Ar^+Ar_2^+Ar_2^+$. The most intense peak in off-axis is $Ar^+Ar_2^+Ar_3^+$. The most intensive peaks in maps of 31 and 32 are the peaks formed of four to six atoms such as peaks $Ar^+Ar^+Ar_2^+$, $Ar^+Ar_2^+Ar_3^+$ and $Ar^+Ar_2^+Ar_2^+$. In addition, in both spectra the most intensive peak is the corner peak at zero flight time separation. When the flight time separation between first and second ion and second and third ion is zero, all the ions measured are identical.

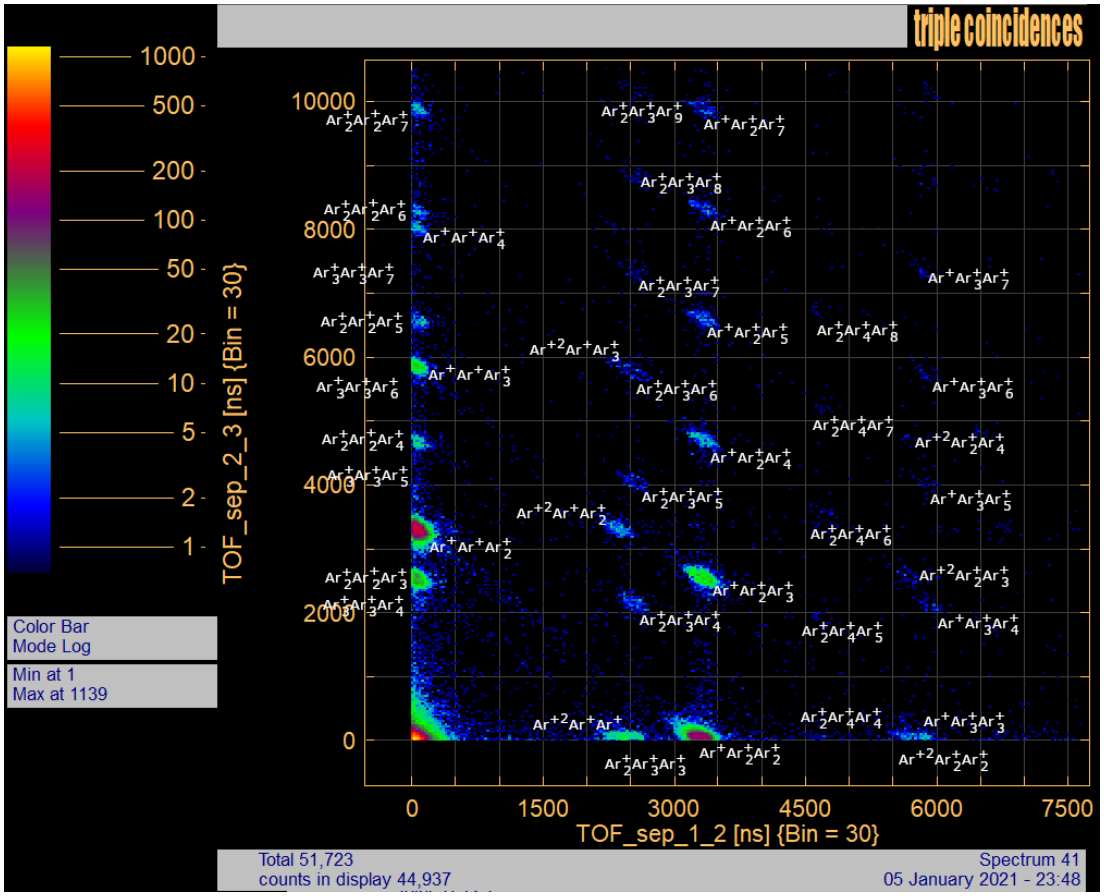

Figure 31: Coincidence map of argon clusters measured at 4.4 bar expansion pressure at 4000 eV ionization energy. Theoretical average cluster size for argon cluster at 4.4 bar expansion pressure is 28 atoms. Due to the constant field mode the flight times are relative flight times. In x-axis the flight time separation of the first and second ion is detected. The flight time separation in y-axis is presented between the second and third fragment. In the x-axis the separation of second and third fragment is zero, which means that the second and third fragment detected are identical. Correspondingly in y-axis the first and the second fragment are identical and therefore the flight time separation is zero.

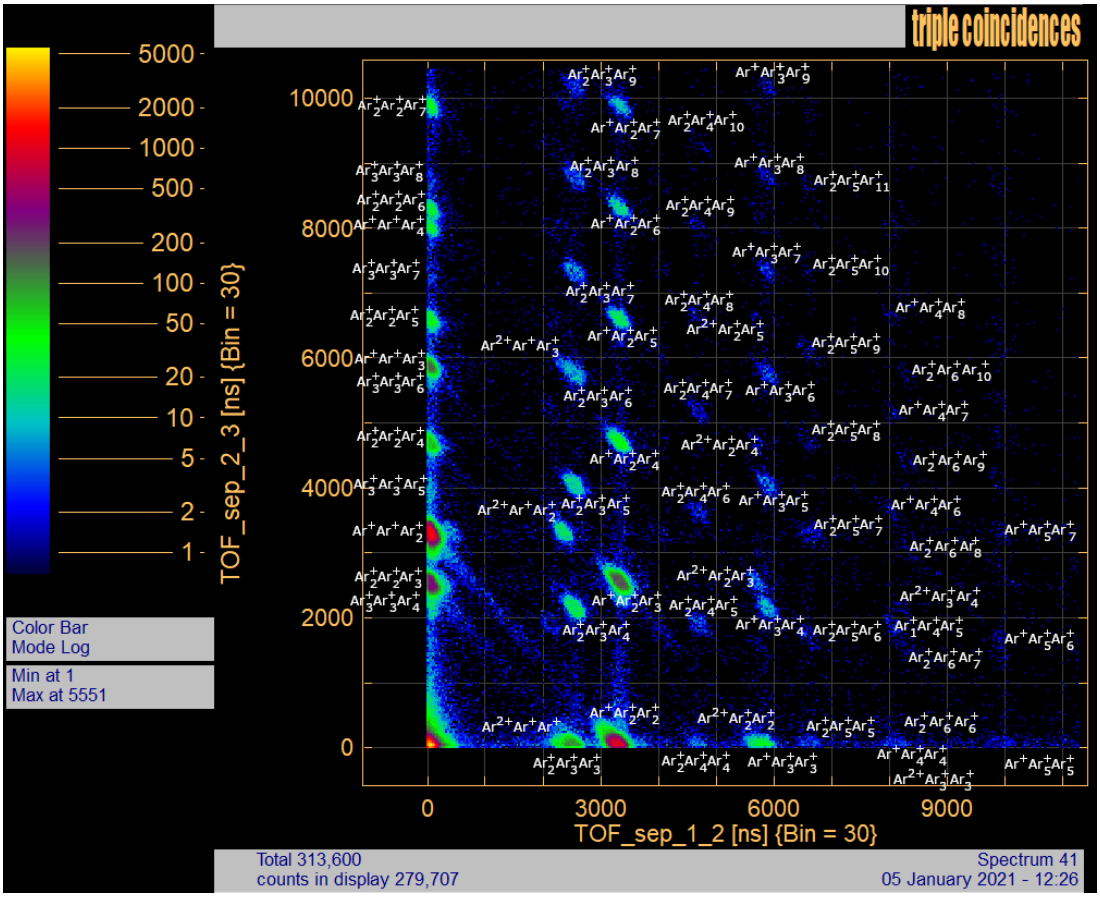

Figure 32: Coincidence map of argon clusters measured at 6.6 bar expansion pressure at 4000 eV ionization energy. Theoretically calculated cluster size for argon clusters at 6.6 bar pressure is 73 atoms.

4.4 Mixed argon-water cluster experiment

Mixed argon-water measurements were measured as a function of expansion pressure at constant ionization energy of 4000 eV. The change of the spectra was measured at 3.2, 4.0, 5.0, and 6.0 bar pressures. From the spectra, in addition to mixed argon-water clusters, also pure argon clusters and protonated water clusters were recognized. Also, dimer and trimer peaks of pure water clusters were found. However, these peaks were minor and are therefore not studied more closely in this thesis. The original spectra of mixed argon-water experiments are shown in figures 33 and 34.

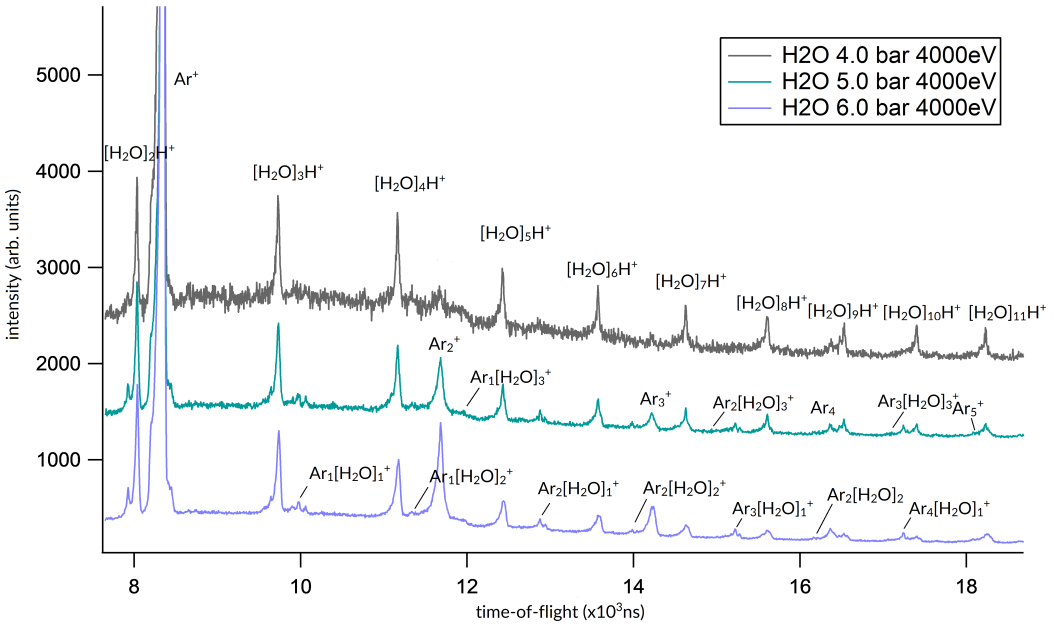

Figure 33: The spectra of mixed argon-water experiments at 4000 eV ionization energy. The peaks are scaled to $[H_2O]_2H^+$ peak. The 3.2 bar spectrum is presented independently due the clarity of the results. Argon, protonated water and mixed peaks $Ar_N[H_2O]_1^+$ $Ar_N[H_2O]_2^+$ are marked into the spectra.

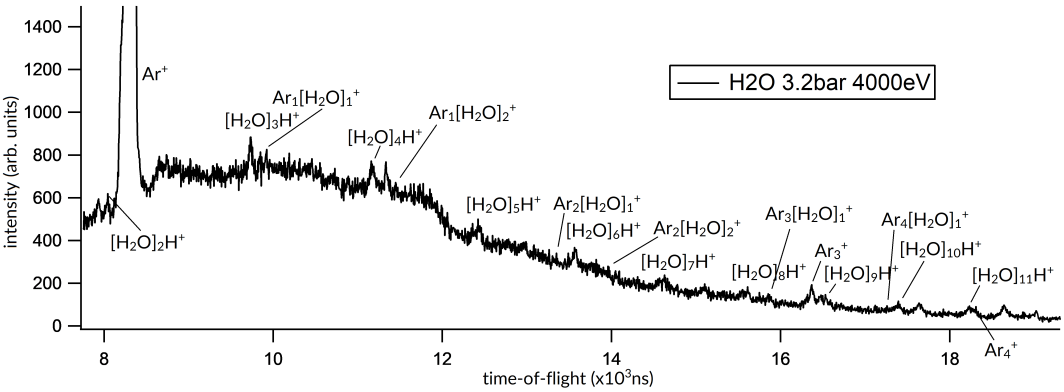

Figure 34: The spectra of mixed argon-water cluster measured at 3.2 bar pressure. Peaks are marked to the figure. The mixed argon-water cluster peaks at this pressure are quite questionable. More statistics should be measured to derive more certain results.

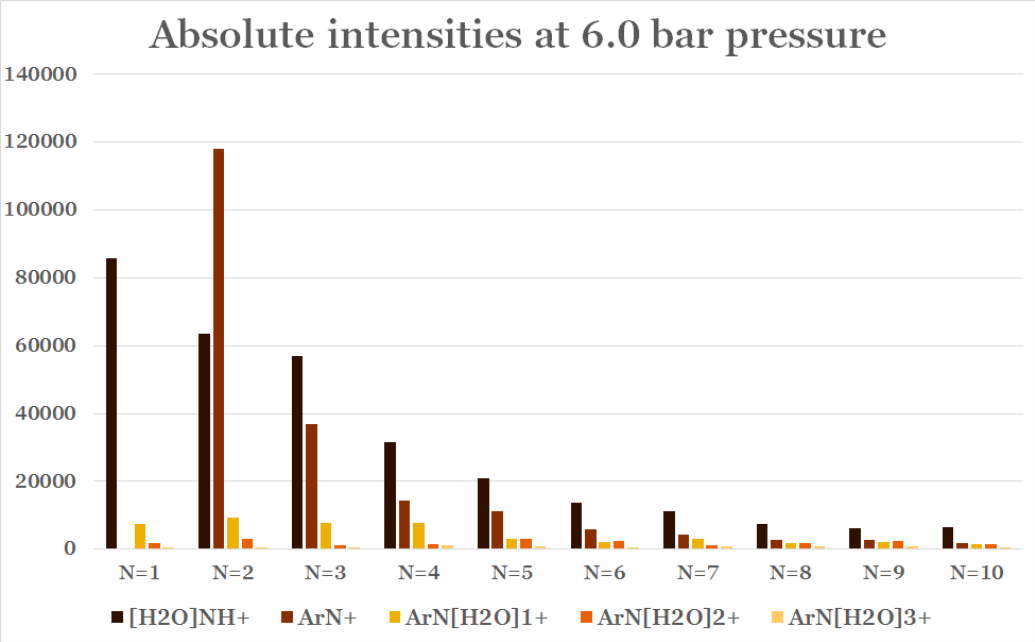

Figure 35: Differences between absolute peak intensities at 6.0 bar pressure in protonated argon-water experiments.

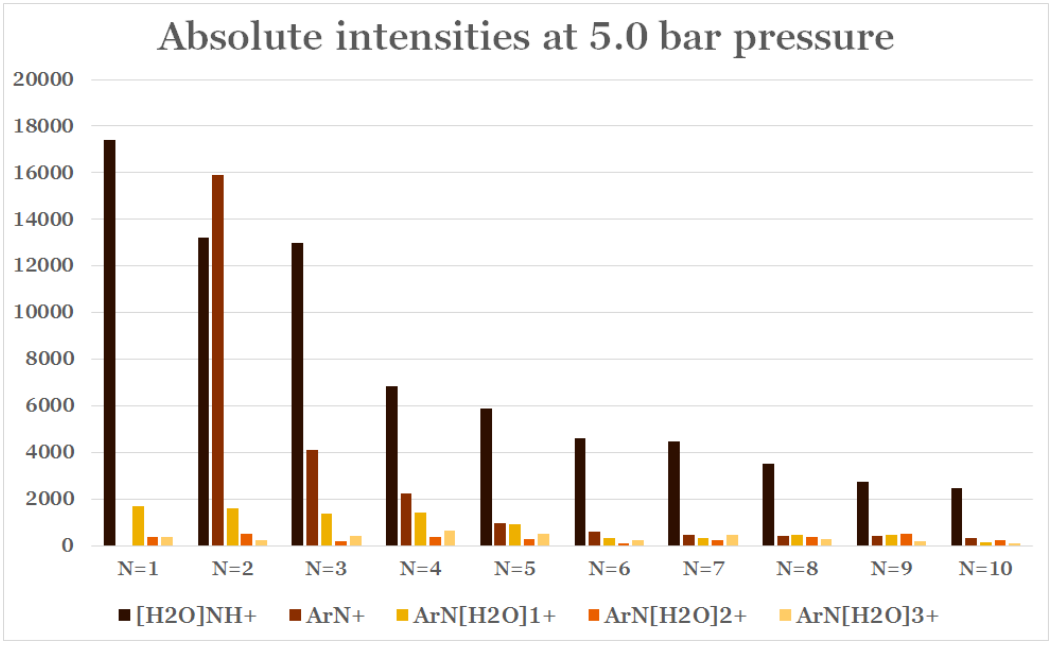

Figure 36: Differences between absolute peak intensities at 5.0 bar pressure in protonated argon-water experiments.

Some of the peaks in longer flight times in the spectra were superimposed which naturally complicated the data analysis. Therefore, there may be some errors in the analysis. Especially the analysis of the mixed argon-water peaks was not unambiguous, and interpretations were made. The mixed argon-water cluster analysis was left out at the pressure of 3.2 bar due the poor statistics. However, the statistics was good enough for argon and protonated water cluster analysis. In addition to mass spectroscopy measurements, also triple ion coincidence spectra were measured for mixed argon-water clusters. The used ionization energy was 4000 eV and the expansion pressure of argon gas 6.6 bar.

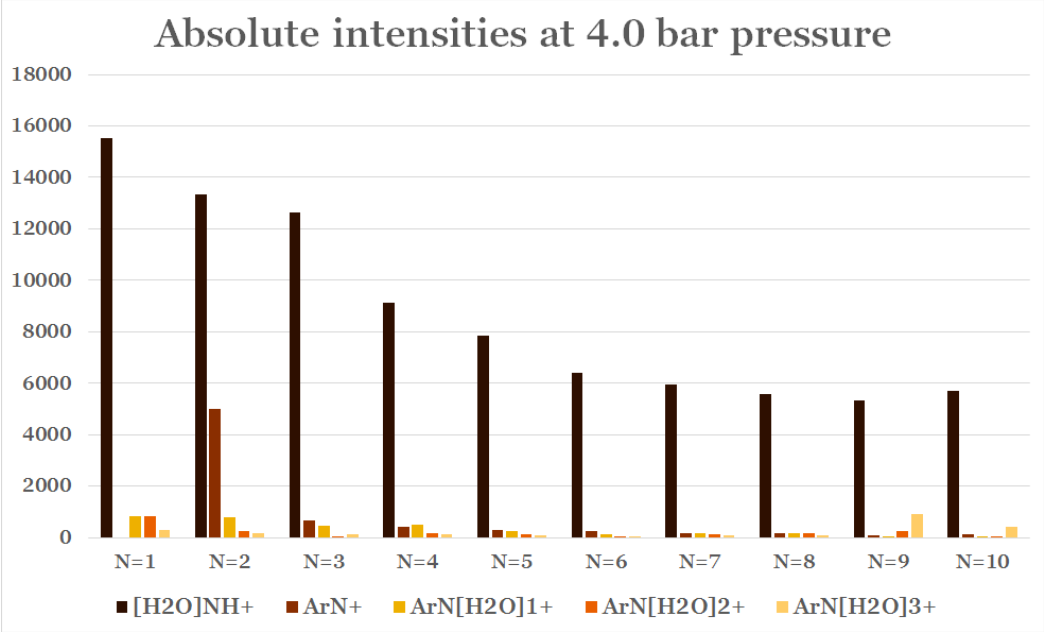

Figure 37: Differences between absolute peak intensities at 4.0 bar pressure in protonated argon-water experiments.

In figures 35, 36, and 37 the differences between different fragments at certain pressure are presented. The trend in all spectra is the same: as the fragment size (N) increases the intensity decreases. For a given fragment the protonated water cluster peaks are the most intense in spite the dimer peak (N=2), where the argon fragment is the most intense at 6.0 and 5.0 bar pressures. The intensities of mixed fragments of $Ar_N[H_2O]_1^+$, $Ar_N[H_2O]_2^+$, and $Ar_N[H_2O]_3^+$ are much lower compared to protonated water and argon fragments. Mainly for a given fragment the $Ar_N[H_2O]_1^+$ is the most intense and $Ar_N[H_2O]_3^+$ the least intensive peak of mixed fragments.

Argon monomer is left out from the results due the fact that the monomer peak does not straightforwardly correspond to the cluster originated fragments. A part of the monomer peak is from the individual argon gas atoms.

4.5 Argon clusters in mixed experiment

Relative argon cluster peaks from mixed argon-water experiments are presented in figures 38a and 38b. In 4.0, 5.0, and 6.0 bar pressures the dimer peak is the highest peak as can be seen from the chart 38a. In chart 38b at 3.2 bar pressure the 4-mer peak is the highest peak. In the spectra measured at 3.2 bar pressure dimer and trimer peaks are missing. From the spectra only 4-mer, 5-mer, 6-mer, 7-mer, and 8-mer peaks are seen. At 3.2 bar pressure there is not much argon clusters formed. The lack of dimer and trimer peaks could be due some ionization or fragmentation related phenomena.

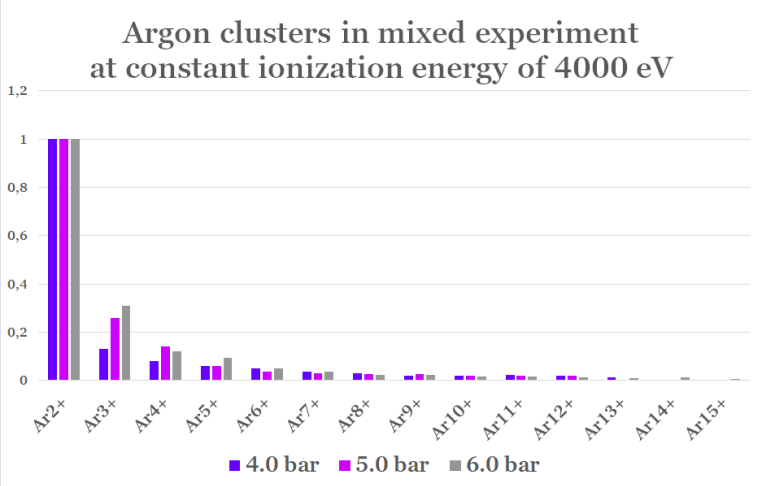

(a)

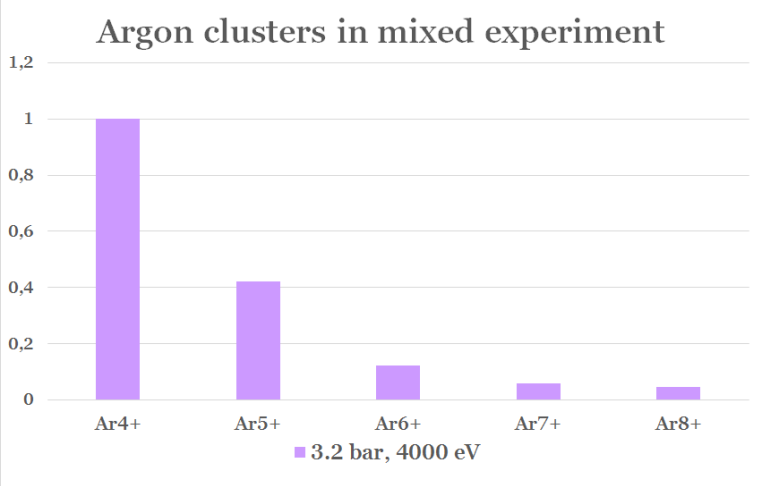

(b)

Figure 38: Argon cluster peak relations presented from mixed argon-water experiments. The results of 3.2 bar spectra are presented in separate chart due the lack of dimer and trimer peaks.

In both charts 38a and 38b the peak area decreases as the fragment size increases. In addition, from chart 38a can be seen that as the pressure increases the relative abundancy increases for a given fragment. Although there is a lot of variations to that trend so it may not be the correct interpretation. For more accurate results more statistics should be gathered.

4.5.1 Protonated water clusters

The protonated water clusters from mixed argon water experiments are presented in figure 39. At 4.0, 5.0, and 6.0 pressures the dimer peak is the highest peak when in 3.2 bar pressure the trimer peak is the highest. However, in every measured spectrum the peak intensity decreases as a function of fragment size. In addition, as the expansion pressure increases the relative abundancy for a given fragment decreases with respect to dimer peak.

From the chart can be seen that trimer, 4-mer and 5-mer peaks in 3.2 bar spectra are significantly higher compared to peaks of other pressures. In addition, 19-mer, 24-mer and 28-mer peaks at 3.2 bar pressure are high compared to the higher pressures. For protonated water clusters the magic numbers are N=21 and N=28. In chart 39 these peaks do not differentiate from the spectra apart from the 28-mer peak at 3.2 bar pressure.

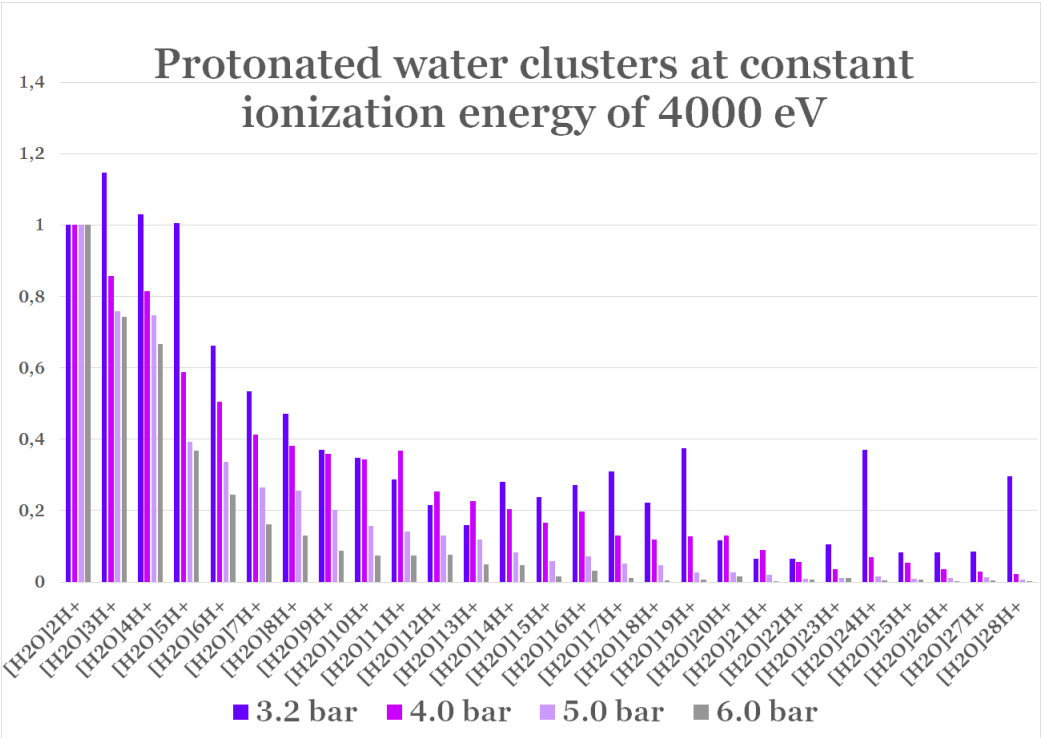

Figure 39: A chart to describe the size distribution in protonated water clusters. In the chart the fragment sizes are presented respect to dimer peak. Used ionization energy in experiments was 4000 eV.

Theoretical cluster sizes for water clusters corresponding the different pressures used in cluster formation are shown in Table 6. The calculations are based on the model derived by C. Bobbert et al. [23] presented in section 2.5.2. The theoretical results cannot be straightforwardly applied to results derived in this thesis. Here not only protonated water clusters were seen, but also argon clusters and mixed argon-water clusters. The presence of argon in the experiments may affect the results. The size model is derived without carrier gas and only expanding the water vapor through the nozzle. However, the size model could give indicative results for the initial sizes of water clusters.

Table 6. Water cluster sizes as a function of pressure

Expansion pressure	3.2 bar	4.0 bar	5.0 bar	6.0 bar
Mean cluster size	279	425	648	913

As can be seen from the Table 6 the theoretically calculated cluster sizes for water clusters are much larger as the theoretically calculated cluster sizes for argon clusters, presented in Table 5, at same pressures.

4.5.2 Mixed clusters

Charts presented in figures 40, 41 and 42 describe the mixed argon-water clusters of form $Ar_N[H_2O]_1^+$, $Ar_N[H_2O]_2^+$ and $Ar_N[H_2O]_3^+$, where N is the number of argon atoms in the fragment. $Ar_N[H_2O]_1^+$ clusters are shown in figure 40. From the chart can be seen that the peak intensity decreases as the size of the fragment increases. Also, for a given fragment, the relative abundancy with respect to dimer peak decreases as the expansion pressure decreases. Therefore, the fragment size increases as a function of increasing initial cluster size.

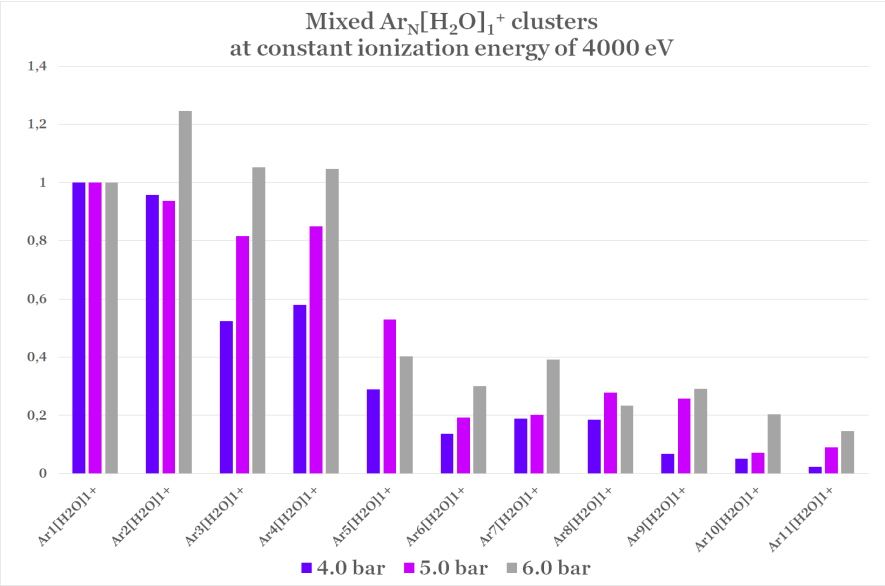

Figure 40: Relative cluster intensities of mixed argon-water clusters of form $Ar_N[H_2O]_1^+$. In peaks $Ar_2[H_2O]_1^+$, $Ar_5[H_2O]_1^+$, and $Ar_8[H_2O]_1^+$ exceptions to the trend can be seen.

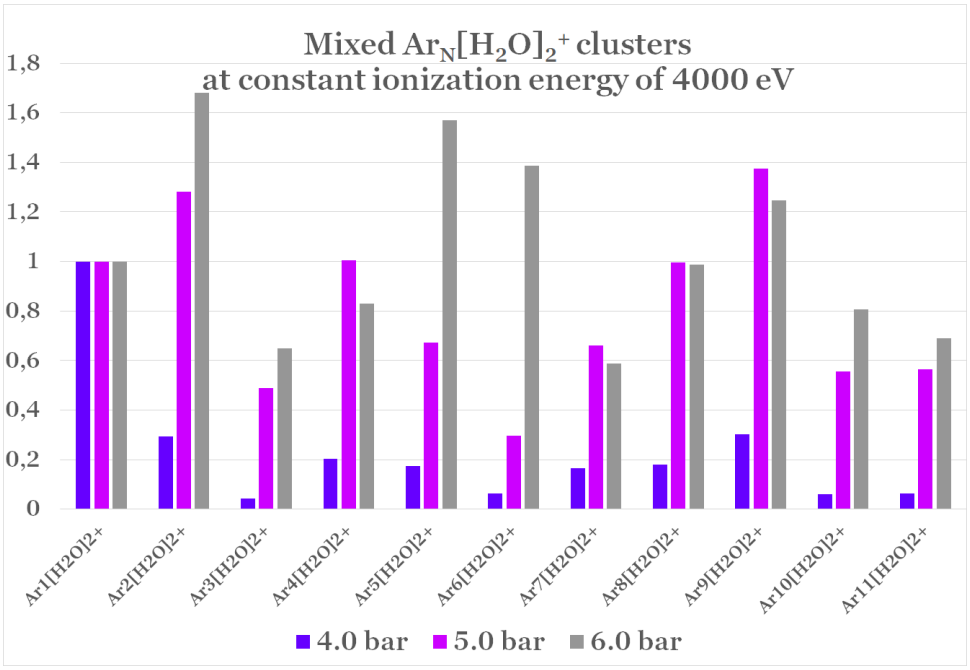

Figure 41: Relative cluster areas of mixed argon-water clusters of form $Ar_N[H_2O]_2^+$ is shown. From the chart inconsistencies for the main trend can be found from $Ar_4[H_2O]_2^+$, $Ar_7[H_2O]_2^+$, $Ar_8[H_2O]_2^+$ and $Ar_9[H_2O]_2^+$ peaks.

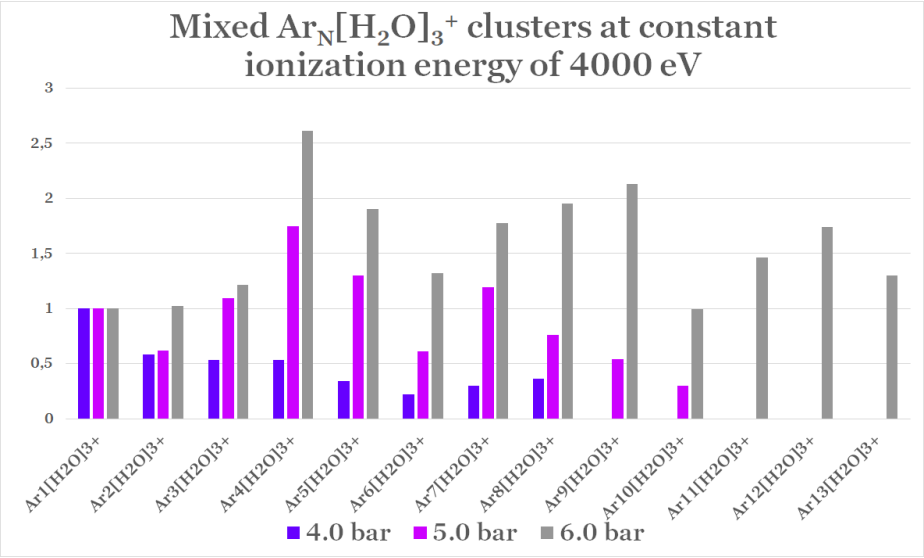

Figure 42: Relative cluster intensities of mixed argon-water clusters of form $Ar_N[H_2O]_3^+$ are shown.

In figure 41 the relative abundancy increases for a given fragment as the expansion pressure increases. The peak intensity varies as a function of increasing fragment size. For 6.0 bar and 5.0 bar spectra the $Ar_2[H_2O]_2^+$ is the highest peak when the highest peak at 4.0 bar pressure is $Ar_1[H_2O]_2^+$ peak. At 6.0 bar pressure there are 4 peaks that are higher than the monomer peak. (Here the monomer peak indicates to the number of argon atoms in a certain fragment.) For 5.0 bar pressure there are two peaks that are higher than the dimer peak.

Figure 42 presents the clusters of form $Ar_N[H_2O]_3^+$. The relative abundancy for a given fragment increases as the expansion pressure increases. This is the same result that was found also for $Ar_N[H_2O]_1^+$ and $Ar_N[H_2O]_2^+$ clusters. The fragment size varies as a function of increasing fragment size. At the spectra of 4.0 bar pressure the monomer peak is the highest peak, when for spectra of 5.0 and 6.0 bar the $Ar_4[H_2O]_3^+$ peak is the highest. At 6.0 bar spectra only the $Ar_{10}[H_2O]_3^+$ is lower than the dimer peak. At 5.0 bar pressure the peaks of $Ar_4[H_2O]_3^+$, $Ar_5[H_2O]_3^+$ and $Ar_7[H_2O]_3^+$ are higher than the monomer peak.

The results presented in the charts 40, 41, and 42 are very tangled. This may be due the small absolute peak intensities and therefore the statistics may be too low for proper results.

4.5.3 Coincidence measurements of mixed argon-water clusters

The results from ion-ion coincidence measurements at 6.6 bar pressure are presented in figures 43-49. The peaks found and recognized from the spectra are labeled. As in mass spectroscopy measurements of protonated argon-water clusters pure argon, protonated water and mixed argon-water fragments are seen.

In figure 43 the pure argon peaks are shown. The argon peak series found in coincidence map 43 are also the series found from pure argon coincidence maps presented in figures 31 and 32. From figures 44 and 45 mainly peaks formed from protonated water clusters are shown. In addition, there are series in which a single argon trimer or dimer and two protonated water fragments are detected in coincidence. In figure 46 protonated water cluster series and mixed protonated water-argon cluster series are found. In addition, a series caused by H_3O^+ ion and protonated water fragments is seen. Also, one series caused by H_3O^+ ion, one protonated water fragment and argon fragment is found.

The coincidence spectra shown in figure 47 presents the series of form $H_2O^+Ar^+K$ and $H_3O^+Ar^+K$, where K is either argon fragment or protonated water fragment. In addition, one series with the base forming from oxygen ion and protonated water fragment $O^+[H_2O]_2H^+L$ is seen, where L is protonated water fragment. The coincidence map 48 shows two peak series with the bases of form $[H_2O]^+[H_2O]_4H^+M$ and $[H_2O]_H^+[H_2O]_4H^+M$, where M is protonated water fragment. The difference between the series is in the first ion. At lower relative flight time the first ion is water dimer, when at higher relative flight time the first ion to reach the detector is protonated water dimer.

In figure 49 four different hydrogen ions H^+ based measurement series is presented. In each series in figure H^+ ion is the first ion, when the second ion at increasing relative flight time is O^+, OH^+, H_2O^+ or H_3O^+. The third ion is an argon fragment in each series.

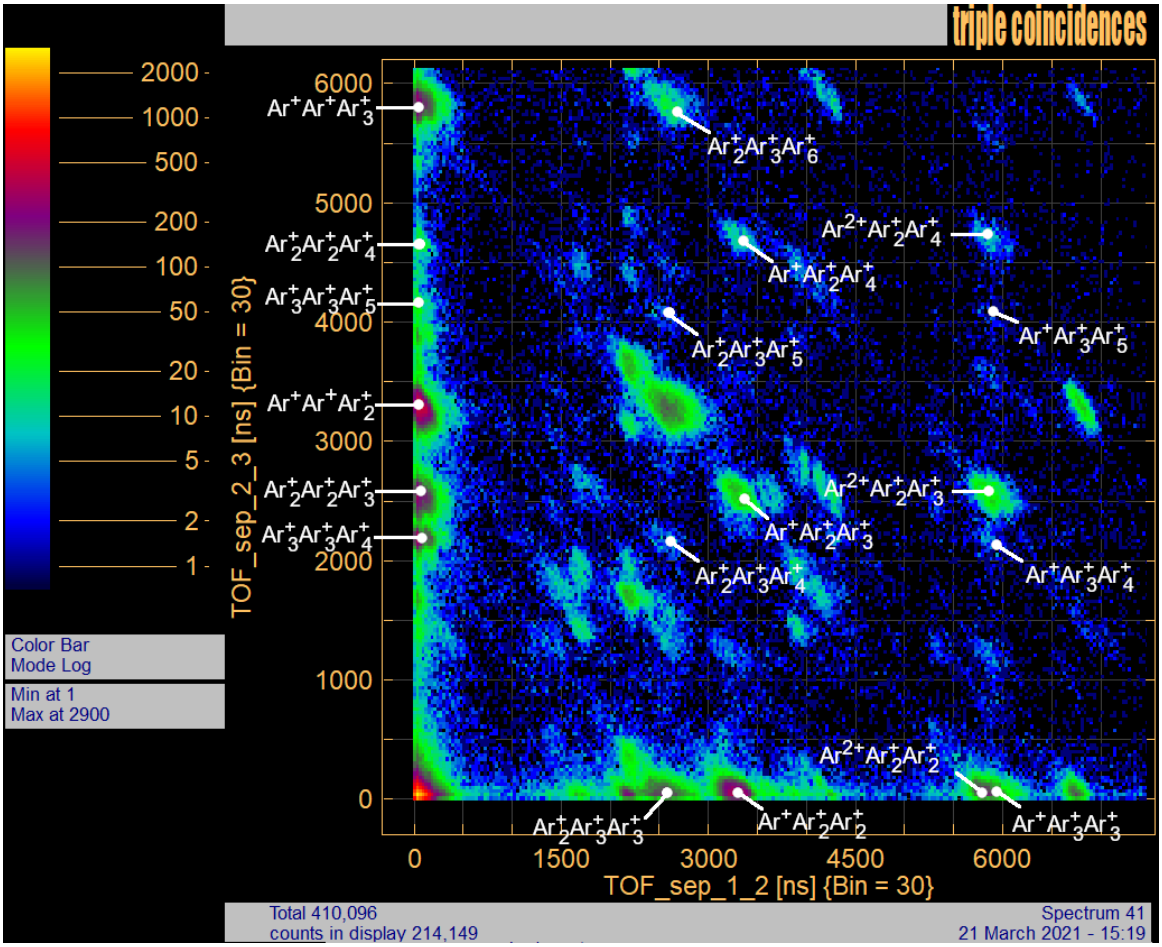

Figure 43: Coincidence map of pure argon fragments in mixed argon-water measurements.

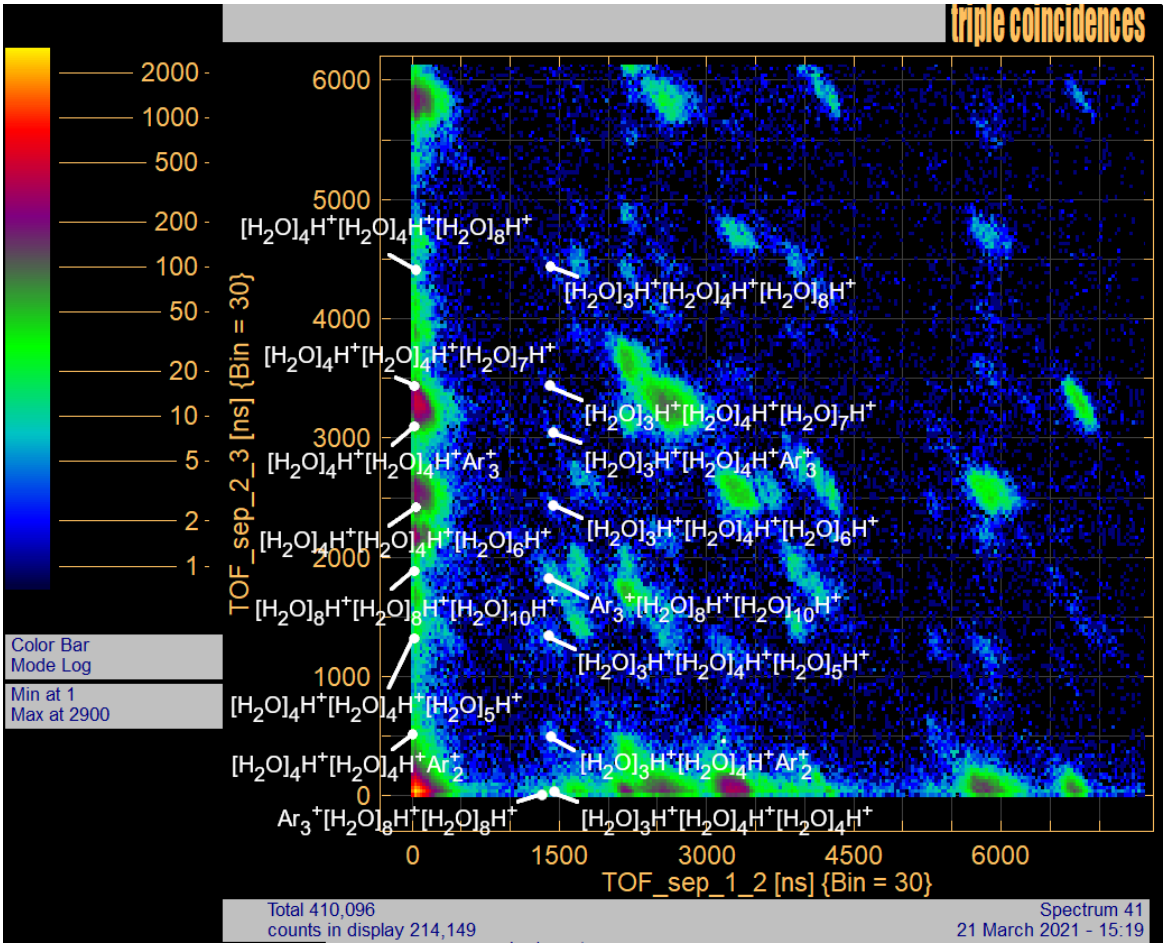

Figure 44: Coincidence map of protonated water fragments and protonated argon-water fragments in mixed argon-water measurements.

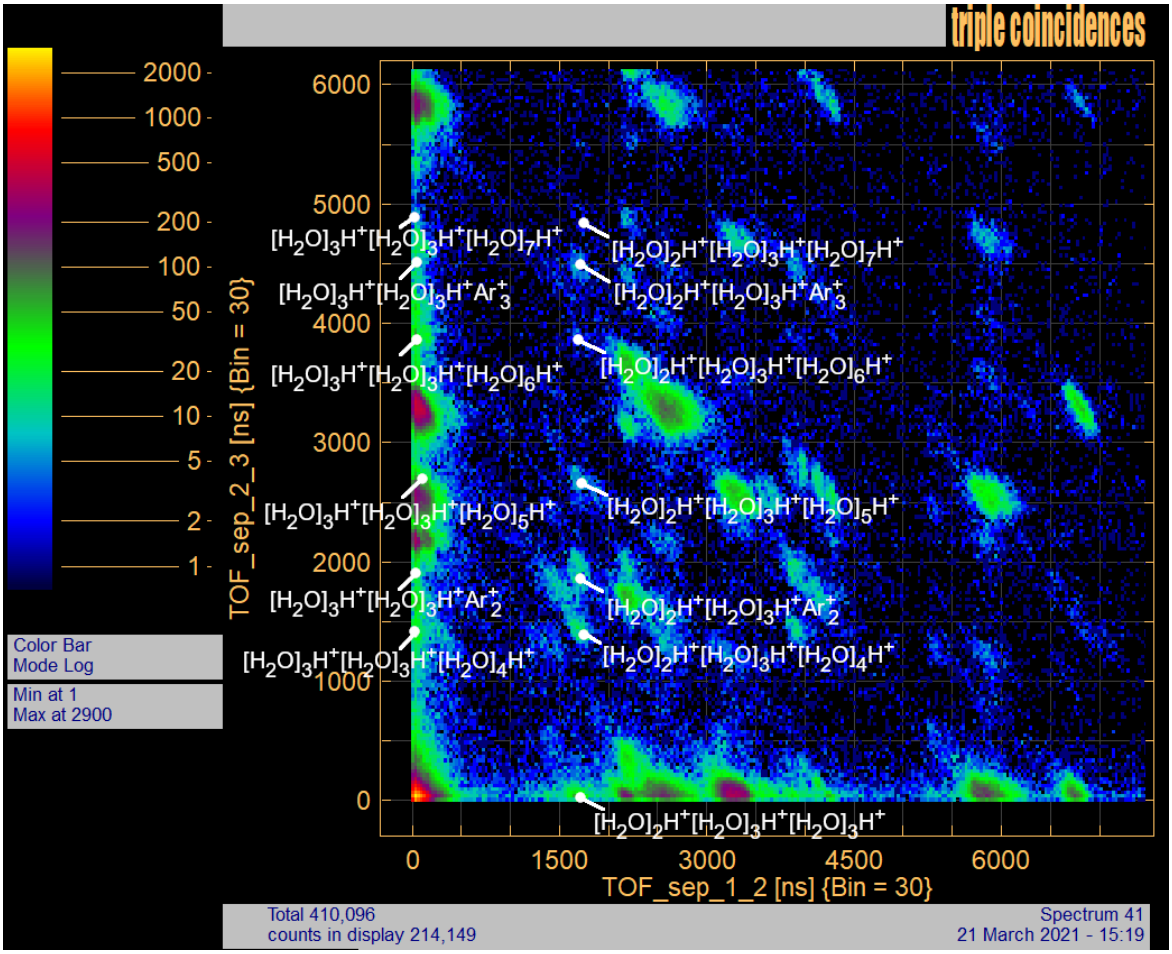

Figure 45: Coincidence map of protonated water fragments and mixed protonated argon-water fragments in mixed argon-water measurements.

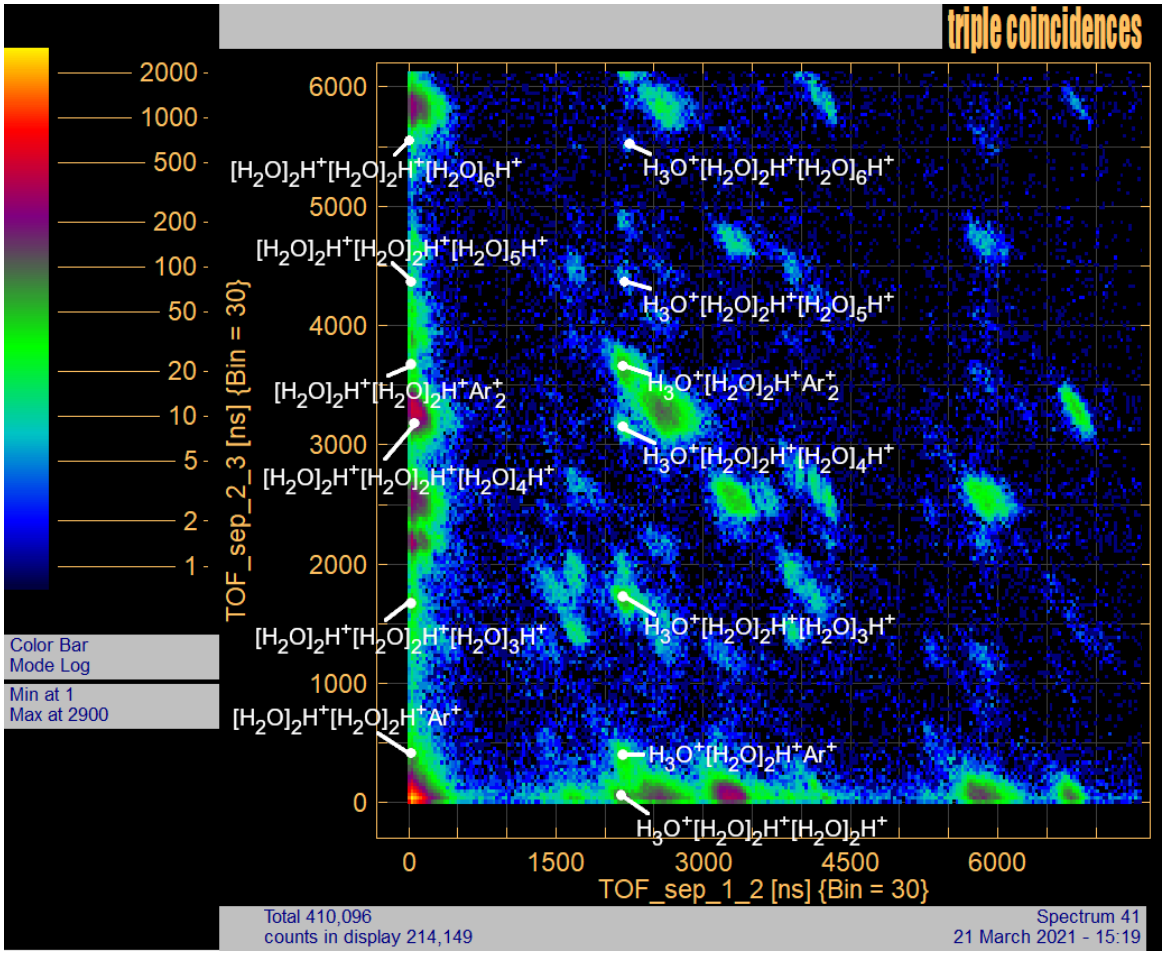

Figure 46: Coincidence map of protonated water fragments and protonated argon-water fragments in mixed argon-water measurements.

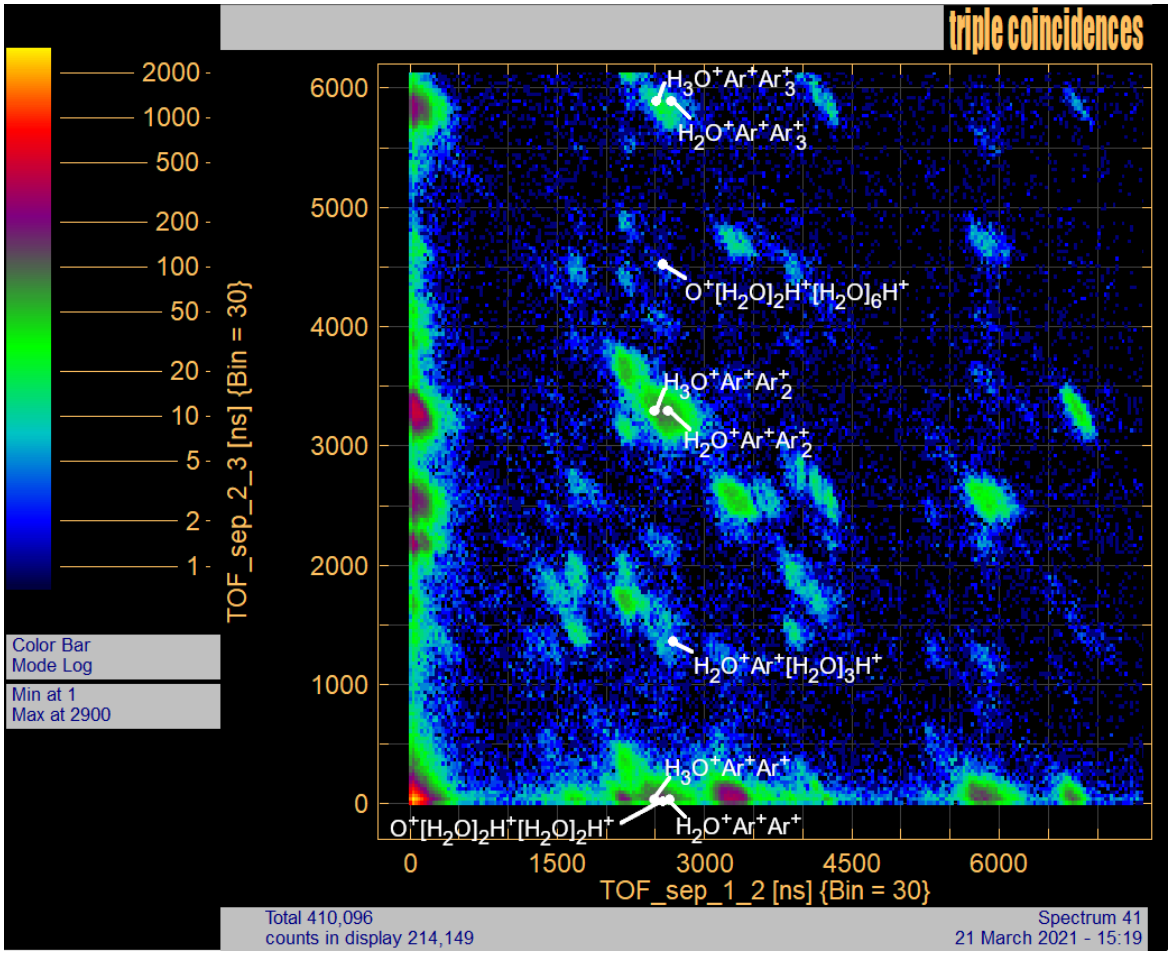

Figure 47: Coincidence map of mixed protonated water-argon fragments in mixed argon-water measurements.

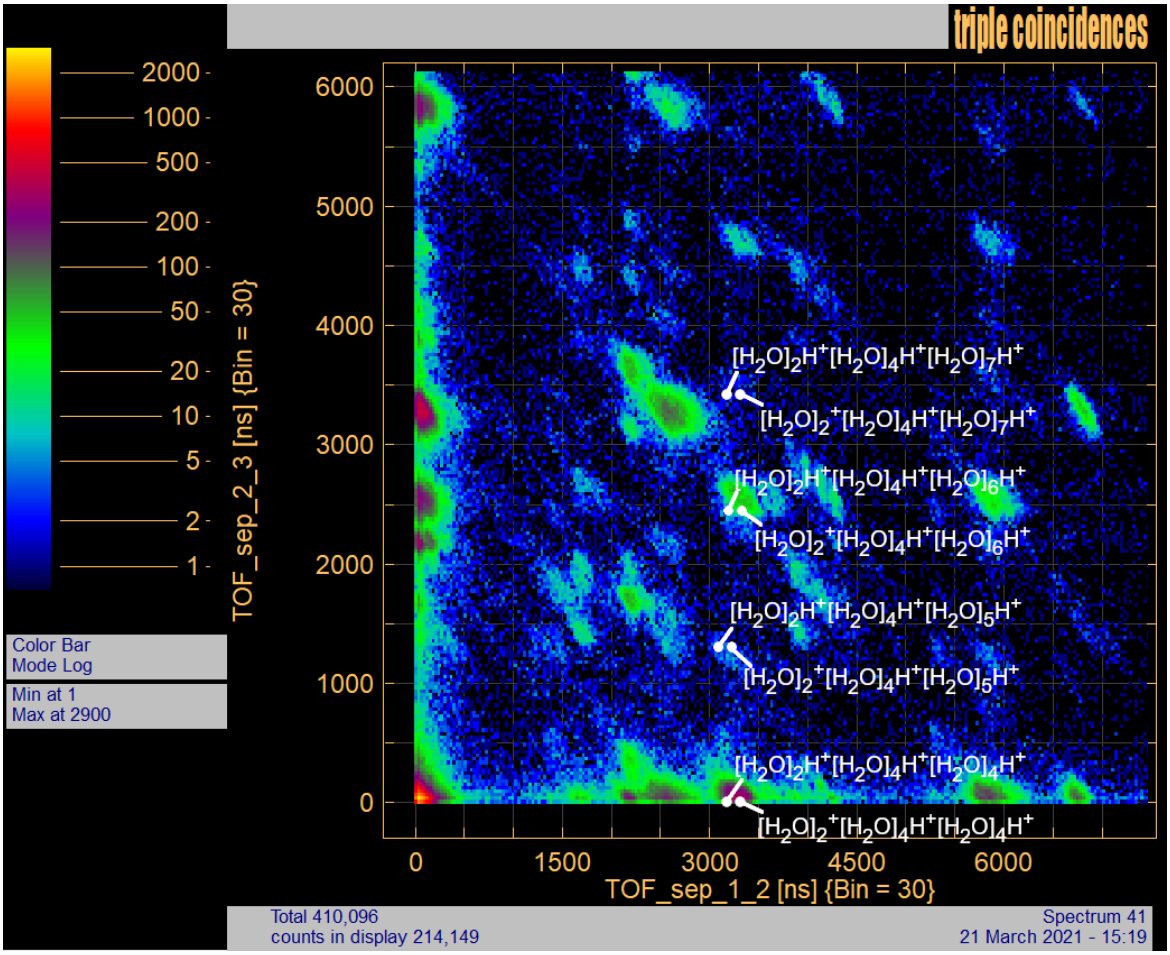

Figure 48: Coincidence map of protonated water fragments and protonated water-water fragments in mixed argon-water measurements.

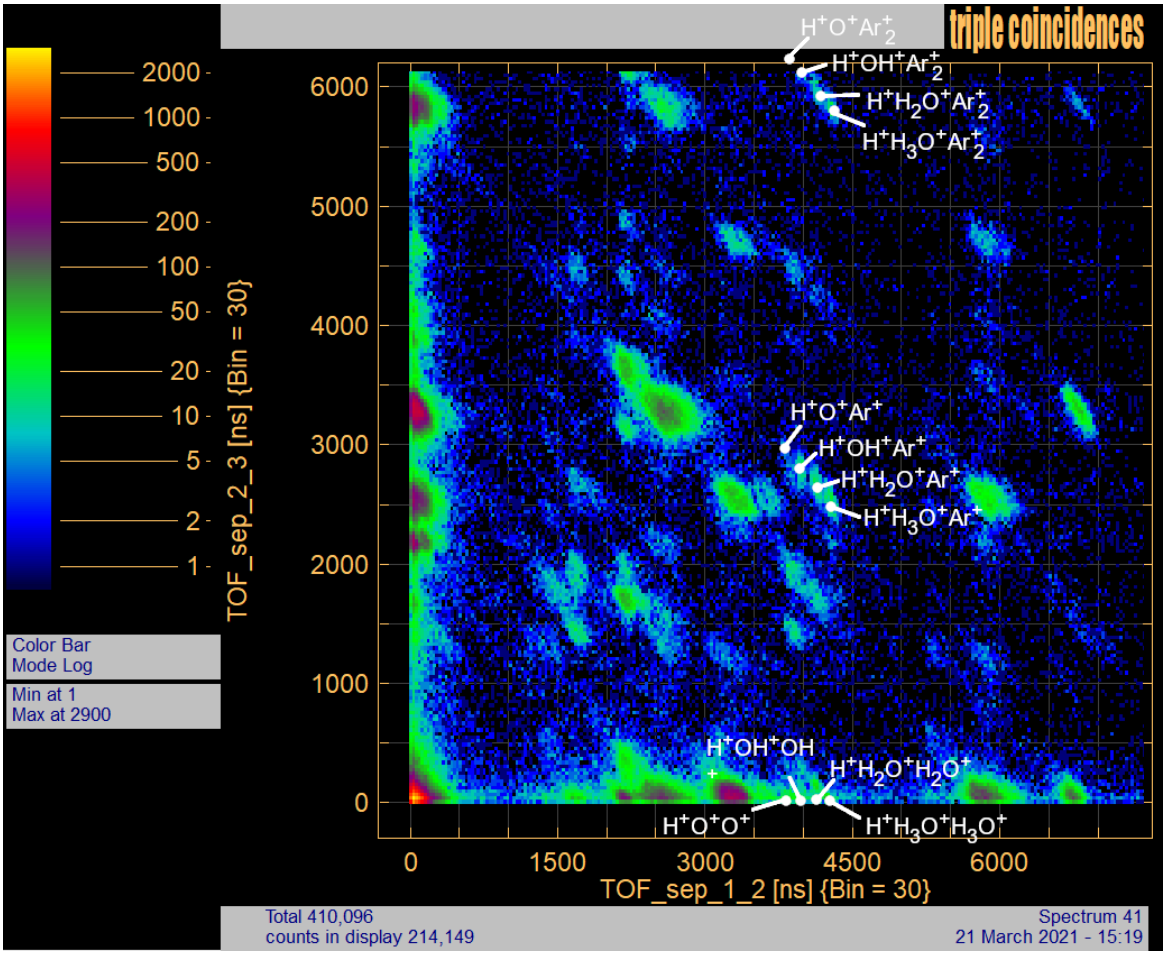

Figure 49: Coincidence map of H^+ ion based fragments in mixed argon-water measurements.

5 Discussion

The presumption for mass spectroscopy measurement is that the higher the expansion pressure the larger the initial clusters are [30]. Therefore, the larger the initial clusters are the larger the fragments should be after ionization. Respectively, with higher ionization energy the fragments should be smaller since they are also created via Coulomb explosion after Auger cascades in addition to direct ionization [46]. Fragmentation processes of clusters are not fully understood and therefore some of the results derived in this thesis cannot be perfectly explained.

5.1 Rare gas clusters

In spectra 50a it can be seen that for a given xenon fragment, the relative abundancy with respect to dimer increases as the initial cluster size i.e. expansion pressure increases. Also, in the measurements as a function of ionization energy the relative abundancy for a given fragments increases as the ionization energy decreases. Both results are in line with the presumptions that were made.

In the study of A. N. Arseniev et al. it was found out that the intensity of peaks changes in relation to ionization energy. For higher ionization energies the number of small fragments increases whereas at low ionization energies the number of small fragments respectively decreases. [46] This is exactly same result as was found here for xenon clusters measured as a function of ionization energy presented in figures 50b and 50c. The results in the spectra of 50b and 50c are in agreement. According to A. N. Arseniev et al. the greater fragmentation at higher energies is due the fragmentation of multiply ionized clusters. The fragmentation of multiply ionized clusters is explained by Coulomb decay in clusters. [46]

In figures 51a and 52b the differences between the energy dependence measurement series at 4.0 bar and 6.8 bar for argon are shown. In both charts some inconsistencies are found. However, the trend of decreasing peak intensity as a function of increasing fragment size can be found in both charts. Also, the as the ionization energy decreases the fragment size increases. In the spectra measured at 4.0 bar pressure there are more variations between the peak intensities than in the spectra measured at 6.8 bar pressure. In addition, in 4.0 bar spectra the dimer peak in relation to other peak intensities is lower compared to peak intensity relations in 6.8 bar spectra. The difference is found especially at 70 eV and 20 eV ionization energies between the two expansion pressures.

The binding energies for different shells in argon atoms are 3205.9 eV for $1s$, 326.3 eV for $2s$, 250.6 eV for $2p_{1/2}$, 248.4 eV for $2p_{3/2}$, 29.3 eV for $3s$, 15.9 eV for $3p_{1/2}$ and 15.7 eV for $3p_{3/2}$ subshell. The spectra measured at 20 eV can only ionize electrons from $3p$ orbitals. In the spectra measured at 4000 eV ionization energy, the ionizations are possible in every shell. However, it is experimentally measured that even though the ionization energy would be high enough for argon K-shell ionization, the probability to that process to occur is low [47].

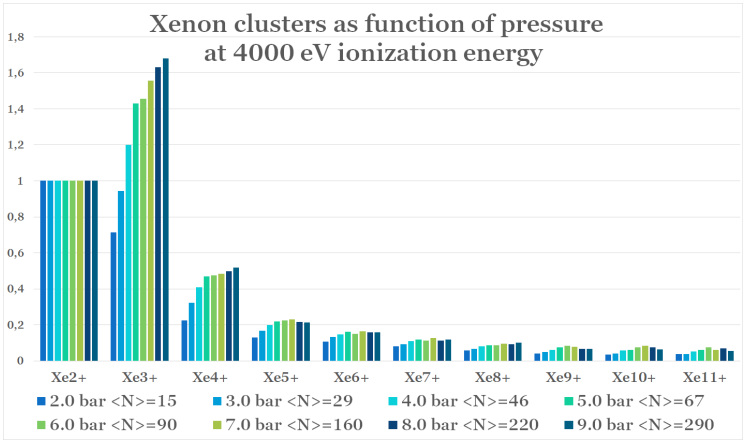

(a)

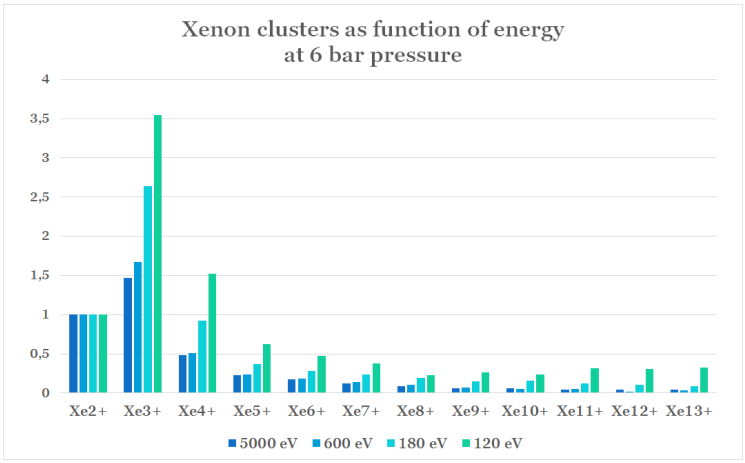

(b)

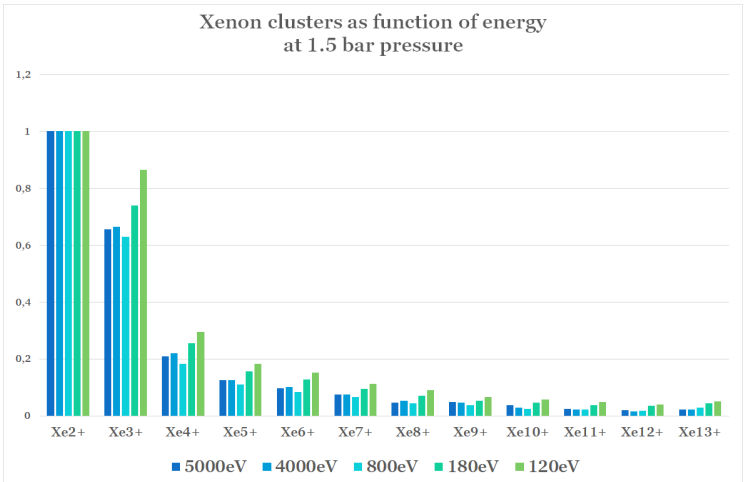

(c)

Figure 50: A summary of mass spectrometry measurements for xenon clusters.

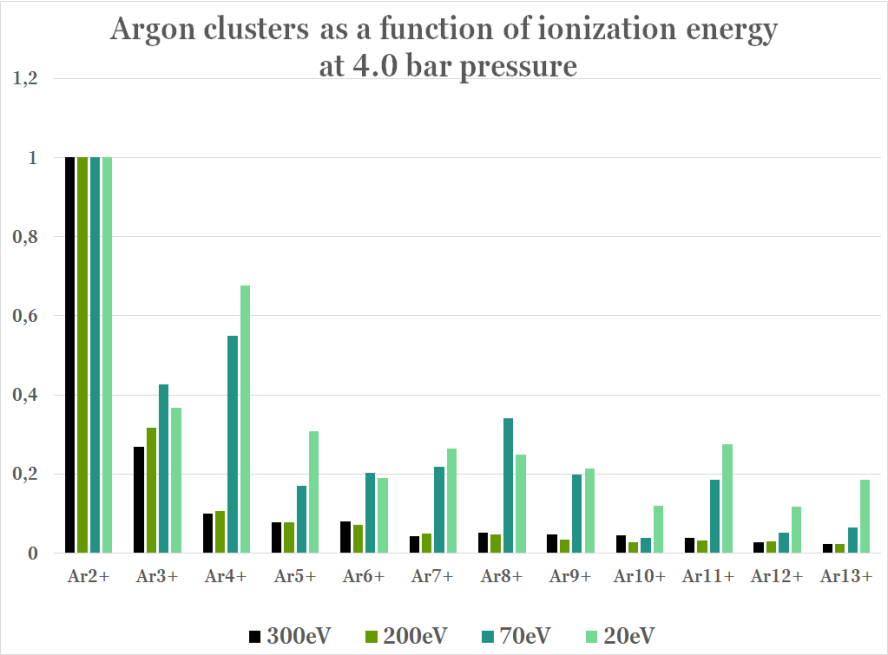

(a)

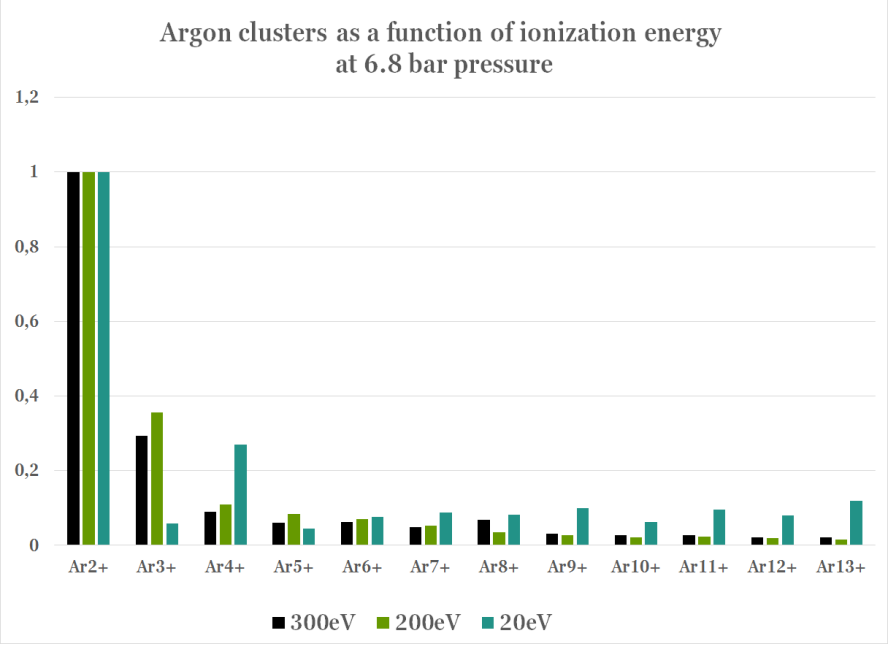

(b)

Figure 51: A summary of mass spectroscopy measurements for argon clusters as a function of ionization energy.

In charts 52a and 52b differences between pressure dependency spectra measured at ionization energies of 20 eV and 4000 eV are shown. In both spectra the relative abundancy for a given fragment decreases as the expansion pressure, i.e. fragment size, increases. In chart 52a the results are more consistent compared to results presented in figure 52b. The peak intensity decreases uniformly as fragment size increases at 4000 eV ionization energy when for 20 eV ionization energy the peak intensity varies as the fragment size increases. However, the trend in 20 eV spectra is also decreasing. The inconsistencies could be a cause of certain ionization paths. Although the more probable reason for variations in the results of 20 eV spectra is that the electron gun does not necessarily work optimally in such low energies. Also, better statistics in 20 eV measurements could sharpen the results. However, the better measurement conditions would not probably change the main trends that were seen from the results. Possibly at 4000 eV ionization energy several fragmentation processes are possible. Perhaps in low ionization energies fewer fragmentation paths are possible, and therefore the peak intensities vary in chart 52b.

In study of M. Gisselbrecht et al. [48] argon clusters are studied as a function of cluster size at ionization energy of 216 eV. The ionization in their study is caused by XUV photons. According to their study for a given fragment the intensity of a fragment decreases as the initial cluster size increases. For every size, the dimer peak is the most intense. The results are interpreted that for small clusters (average cluster size $< N >= 10$ and $< N >= 20$) the measured peaks are due the direct photoionization and fragmentation, as for larger clusters (average cluster size $< N >= 100$ and $< N >= 1000$) the peaks are only due the photofragmentation. In photoionization the ionized clusters do not dissociate into smaller fragments. In photofragmentation the initial cluster ionizes and dissociates into two or more fragments. [48]

The results derived by M. Gisselbrecht et al. are similar compared to results derived in this thesis, although the ionization method is different, so the results are not straightforwardly comparable. However, in the fragmentation and ionization mechanism may have similarities in both cases due the similar results. It is possible that also in electron impact ionization small clusters only ionize without fragmentation as is described in equations 25. Single ionization 25 is possible ionization mechanism for all ionization energies used in these experiments. In larger clusters, the ionization is followed by fragmentation which produces with high probability small fragments such as monomers, dimers and trimers. In this thesis the larger clusters could fragment via processes described in equations 26, 30, 31, 32 and 28.

In equations 26, 30 and 31 the initial cluster is doubly ionized and fragmented into either two charged fragments, or one doubly charged and one neutral fragment. The double ionization is possible with 70 eV or higher ionization energies used in this study. Also, the fragmentation process described in equation 28 is possible, although in this experiment it is impossible to know whether some of the fragments are neutral or negatively charged. However, it could be very probable due the relatively large differences between the size models and fragments detected from the mass spectra.

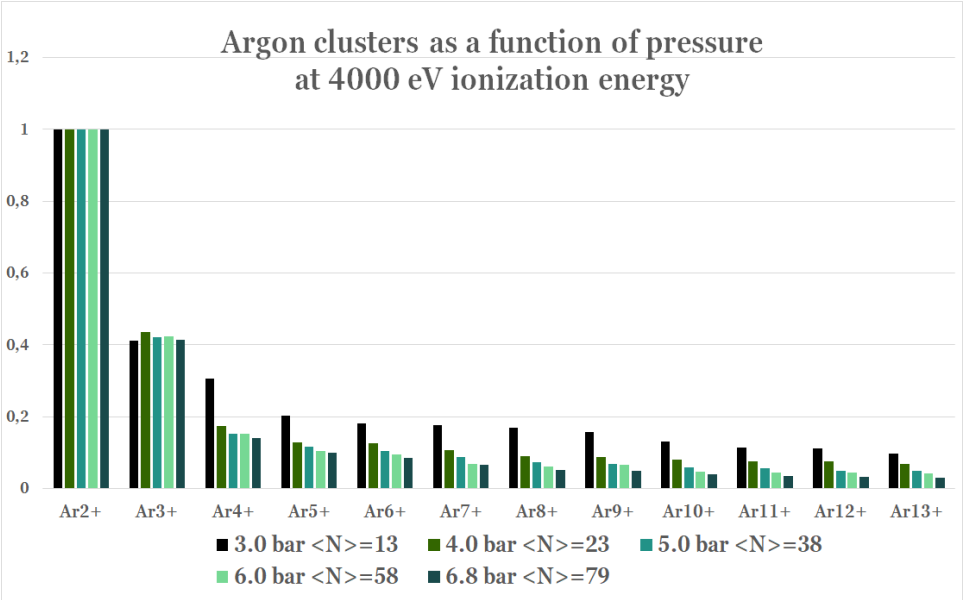

(a)

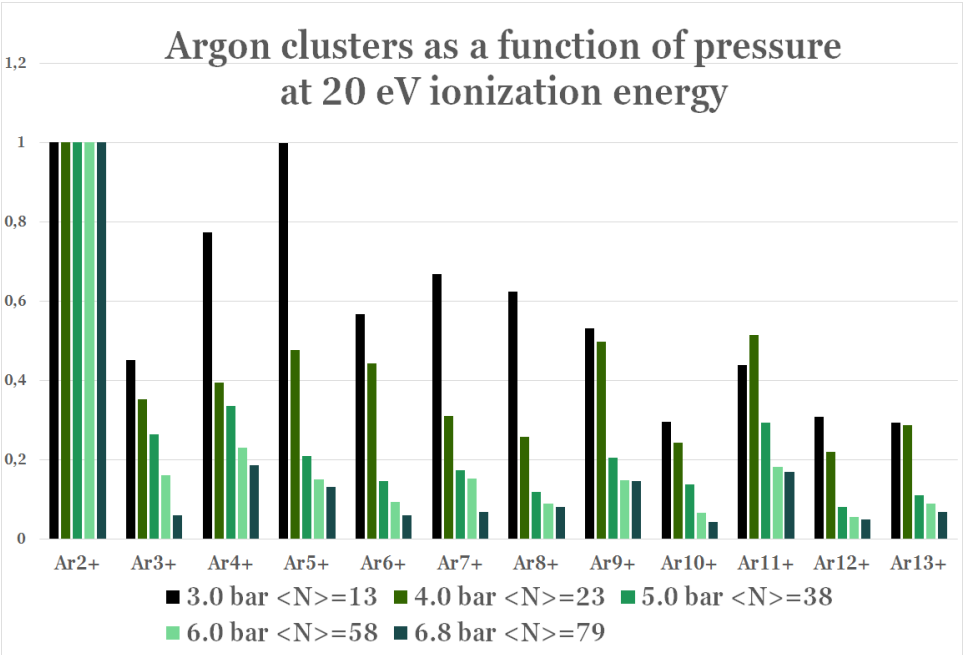

(b)

Figure 52: The comparison between the pressure dependency measurements with ionization energies of 4000 eV and 20 eV. The theoretical cluster sizes according to U. Buck and R. Krohne are marked into the charts.

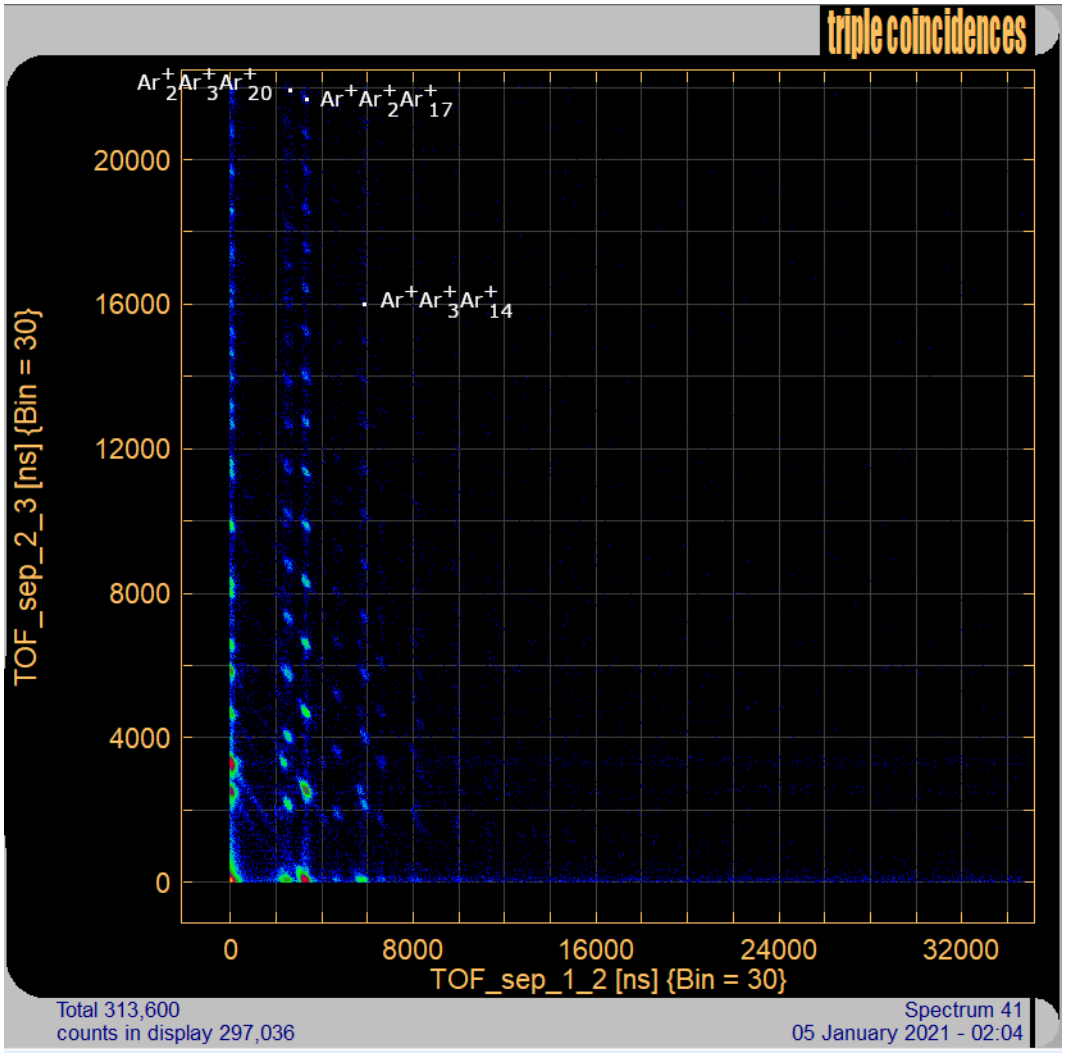

Figure 53: The whole coincidence spectra measured at 6.6 bar pressure. The three largest peaks, in terms of total number of atoms, are marked in the figure. Even though the theoretical cluster size for argon at 6.6 bar pressure is 73 the largest sum of the single peak is 25 atoms.

From the coincidence spectra 31 and 32, it can be seen that in most fragmentation processes a monomer, dimer or trimer ion is produced. Even the largest of fragments in coincidence maps come in coincidence with a small fragment. This is probably the reason why the dimer peak and other small atom number peaks are high apart from the initial cluster size in every mass spectrum shown in this thesis. Also, the peaks recognized from the coincidence maps indicate that in fragmentation process there are also neutral or negatively charged fragments formed. For instance, theoretically calculated cluster size for coincidence measurements at 6.6 bar pressure is 73 atoms, but in the coincidence map there are no peaks in which the sum of the three fragments would achieve 73 atoms. The whole coincidence

map for 6.6 bar pressure is shown in figure 53 where the highest fragment sum of single peak is 25. Although, the series continue outside the map, the number of counts within the peak insignificantly few.

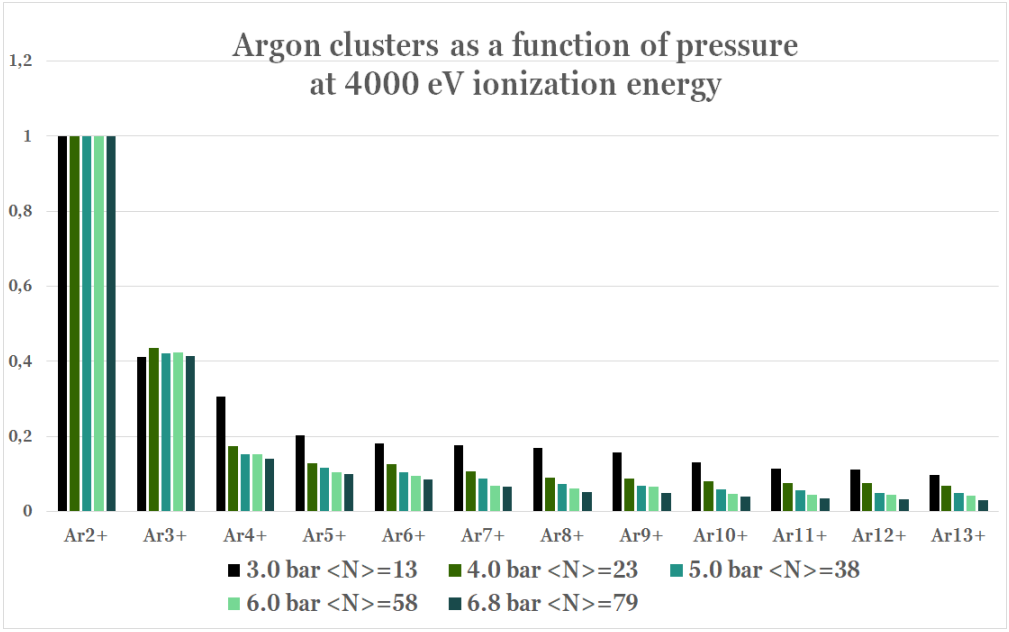

(a)

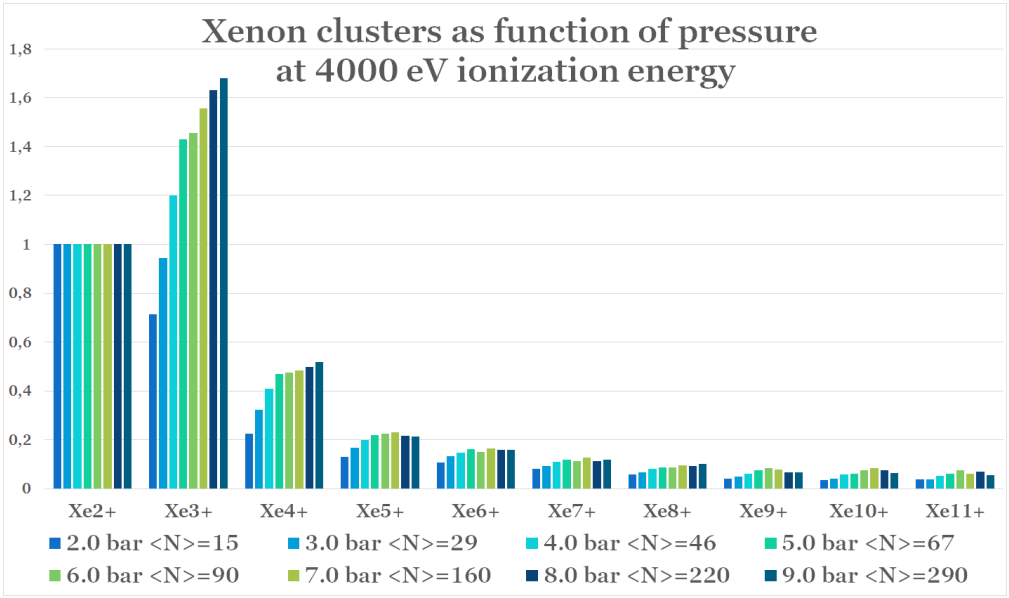

(b)

Figure 54: The differences between argon and xenon measurements as a function of expansion pressure with same ionization energy of 4000 eV.

In figure 54a and 54b there are very interesting differences to be seen between the spectra of argon and xenon measured as a function of a expansion pressure. When for a given xenon fragment, the relative abundancy increases as the expansion pressure increases, for argon the relative abundancy decreases at increasing expansion pressure. The difference between the argon and xenon spectra could be explained by the bonding energies. For neutral xenon dimer the bonding energy is two times higher compared to argon dimer as was stated in section 2.2.3. The bonding energy in dimers indicate the strength of the bonding in larger clusters too. In xenon clusters the bonding is stronger which leads to lighter fragmentation. In argon the weaker bonding energy enables very strong fragmentation. Perhaps in argon the bond strength is that weak that in fragmentation some of the largest fragments dissociate further into smaller fragments. Since the number of atoms increases as the cluster size increases so does the number of small fragments. When the initial cluster size in argon is smaller the relative amount of dissociated small fragments is smaller. In xenon clusters the bond strength could be high enough to keep the large fragments from further dissociation. As can be seen from the coincidence spectra 31 and 32 even the largest of fragments in the spectra come in coincidence with a very small fragment. To understand better the differences between argon and xenon spectra, a further study of krypton and neon clusters would offer more information.

After all, the results that are derived about rare gas clusters in this thesis could be relatively reliable since the results between different measurement series support one another. However, stronger models for fragmentation paths should be derived for comprehensive understanding of the phenomenon. The study of A. N. Arseniev et al. [46] verifies the results of xenon clusters presented in this thesis and respectfully the study of M. Gisselbrecht et al. strengthen the results derived for argon.

To understand better the differences between the results of xenon and argon experiments further research should be made. Triple ion coincidence experiment on xenon clusters could produce interesting data about the fragmentation processes of xenon clusters. Via coincidence measurements on xenon clusters, it would be possible to explain satisfactorily the differences between xenon and argon mass spectra presented in this thesis.

5.2 Mixed cluster experiments

In coincidence measurements for mixed argon-water clusters interesting features about fragmentation can be seen. According to results shown in section 4.5.3 mixed argon-water clusters are mainly fragmented into two fragments of protonated water and one argon fragment. From coincidence map a fragment consisting of water and argon are not found. The result could indicate that mixed clusters are formed from argon part and water part in the expansion. The argon atoms would probably be on the surface of the mixed argon-water cluster. The study of G. E. Douberly et al. [9] presented in section 2.3.2 and in figure 7a supports the deduction. According to G. E. Douberly et al. in small, argon-water clusters the argon atom is bonded always in the surface atom of the water cluster. Although the results of G. E. Douberly et al. are derived for small clusters, the results could apply also for larger cluster sizes. Even though mixed fragments could not be found from coincidence spectra, they were found from the mass spectra. Probably the structure of the mixed fragment is similar to structures presented in figure 7a.

In mass spectra the mixed fragments are singly ionized which could mean that the ionization degree would be +1 for the initial mixed cluster. The lack of mixed fragments in coincidence spectra is due the fact that the original fragments measured in coincidence are

multiply ionized. The ionization and fragmentation process for multiply ionized clusters is shown in equation 27. After the multiple ionization process the ionized cluster dissociates into three or more fragments that were measured in coincidence. The coincidence spectra show how mixed protonated argon-water clusters dissociate into argon and protonated water fragments. The dissociation caused by ionization happens from the weakest part of the cluster, which is the bond between an argon atom and a hydrogen atom of the water molecule. The bond strength between argon and hydrogen is 4.2 meV whereas the dissociation energy in argon dimer is 12 meV and linear water dimer is 0.15 eV [1, 20, 50]. Therefore, also the protonated water and argon fragments presented in figures 55 and 56a originated from the cluster that was initially a mixed argon-water cluster.

Comparison between protonated water clusters, argon clusters and mixed clusters are presented in figures 55, 56a and 56b. As can be seen from the charts for protonated water clusters the relative abundancies for a given fragment decrease as the expansion pressure, i.e. initial cluster size, increases. Interestingly for argon clusters and mixed argon-water clusters produced in mixed experiments the trend is opposite. The relative abundancies of argon and mixed clusters increase as a function of an increasing expansion pressure for a given fragment. Althought, nothing sure about the trend of argon fragments in mixed experiments cannot be said. For pure argon clusters shown in chart 52a for a given fragment the relative abundancies decrease as the expansion pressure increases. The trend in protonated water clusters and pure argon clusters (from rare gas experiments) are similar when the trends between charts 56a and 52a are opposite to one another.

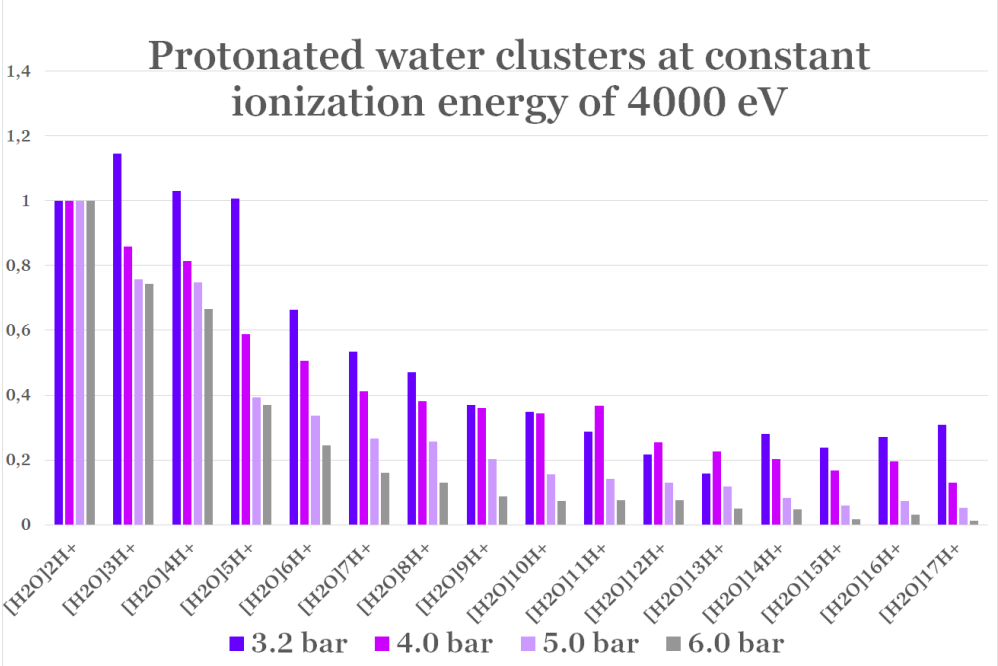

Figure 55: Protonated water clusters

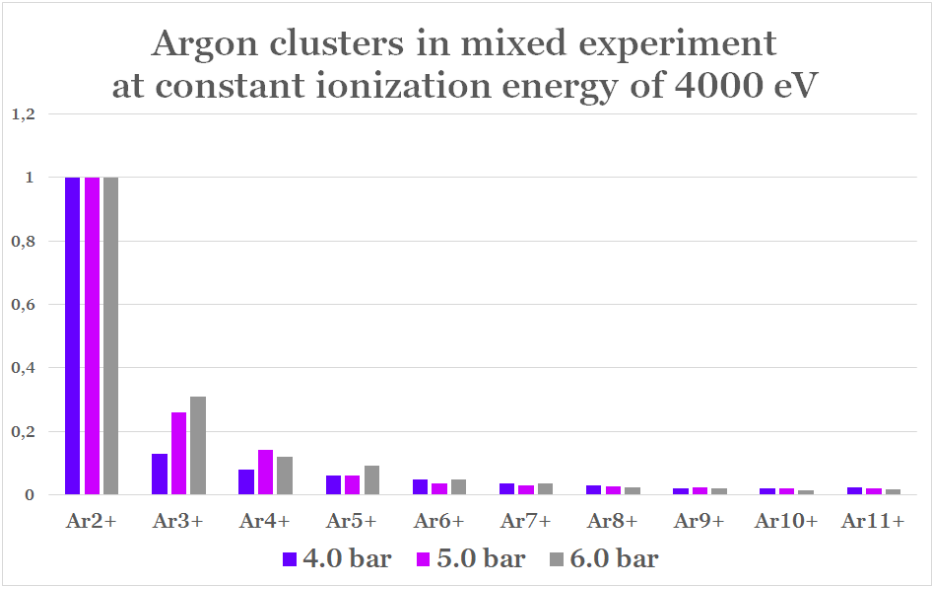

(a)

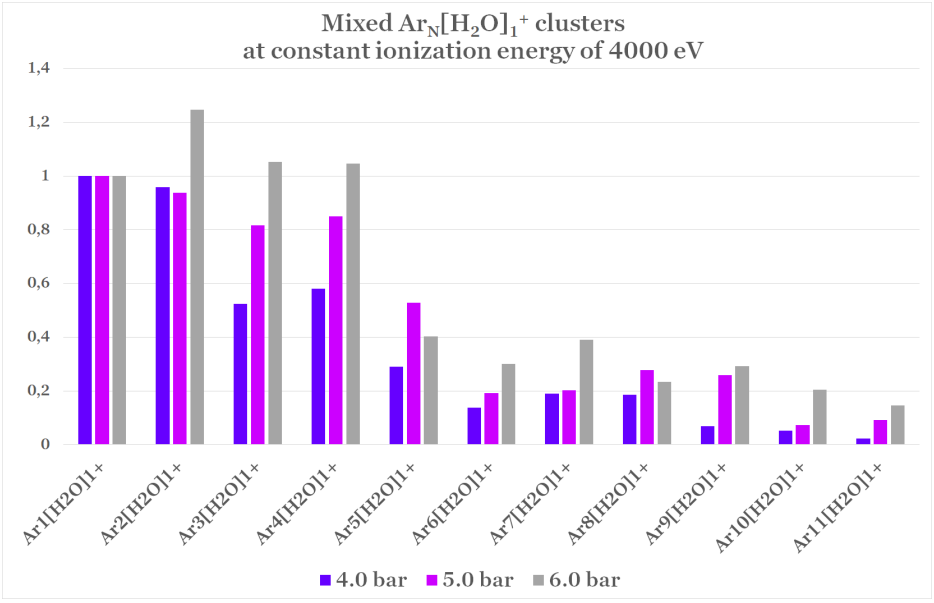

(b)

Figure 56: The summary of argon cluster and mixed argon clusters from mixed argon-water measurements.

The possible explanation for the trend seen in protonated water clusters could be in the fragmentation processes in mixed argon-water clusters. In this speculation two presumptions are made: the fragments measured are from originally mixed cluster, the argon fragments in mixed clusters are located on the surface of the water cluster, and the structure of the cluster

is more permanent for larger sizes. Theoretical calculations of the increasing stability as a function of an increasing cluster size in water clusters are shown for instance in the study of Z. Yang et. al [49]. Here the idea is that in larger clusters water molecules form more stable structures than in smaller clusters. At more permanent structures, the dissociation processes form smaller fragments whereas for smaller and less permanent structures the formed fragments are bigger. This would explain the results presented for protonated water fragments in figure 55.

For larger protonated water clusters it can be seen in figure 7c that the structures are cage-like. The cage-like structures result from the symmetries and the partial charges of the initial water molecules. Single hydrogen atoms can be included into the cage structures. However, single argon atom not to mention argon clusters would probably not be a part of cage structure. In study of K. Suhara et al. [51] protonated methanol-water clusters were studied. In the cluster the water molecules form a cage structure in which the methanol molecule is attached. This is very similar result compared to study of G. E. Douberly et al. The fragments from the coincidence map suggest that the structures in protonated argon-water clusters could be reminiscent to structures presented by K. Suhara et al. and G. E. Douberly et al. Perhaps the geometries of the protonated water clusters and the bond energies between water molecules would prevent the formation of structures in which the argon atoms would be here and there in the water cluster.

From the coincidence maps 43-49 can be seen that most peaks marked in the maps are caused by protonated water fragments, argon fragments or mixture of protonated water fragments and argon fragments. Only four series, shown in the coincidence map 49, are found where the water molecule is dissociated even at 4000 eV ionization energy. The dissociation energy for O-H bond in water molecule is 4.76 eV as was stated in section 2.4. Naturally, the weaker hydrogen bond and van der Waals bond between argon and water molecule break more easily and therefore most of the fragments do not include dissociated parts of water molecule.

Further measurements on protonated argon-water clusters are needed. It would be interesting to see whether the results of mixed fragments would form a uniform trend if there would be more statistics in mass spectroscopy measurements. In addition, triple ion coincidence measurements at different pressures or ionization energies would be an interesting subject for further studies.

6 Conclusions

Interesting results were derived between argon and xenon clusters considering the changes in relative abundancies for a given fragment in measurements as a function of expansion pressure. Via these results a large amount of information about the differences in fragmentation processes between argon and xenon clusters is achieved. The bond strength differences are proposed to explain the opposite spectral features between xenon and argon cluster spectra. However, the explanations are not completely satisfactory. Therefore, further studies are needed to achieve a complete understanding of the studied phenomenon. The measurements as a function of ionization energy for argon and xenon clusters produce relatively expectable results: the fragmentation increases as a function of increasing ionization energy. The derivation for more delicate results was not possible due the problems in electron gun at low energies and lack of necessary statistics.

For mixed argon-water clusters information about the structures and fragmentation processes is derived from the mass and coincidence measurements. In a mixed cluster argon atoms are determined to be on the surface of the cluster. Fragmentation of cluster occurs most probably from the argon-hydrogen bonds. More information about the fragmentation processes of mixed clusters could be derived via more advanc ed data analysis.

References

[1] R. L. Johnston, Atomic and Molecular Clusters, Taylor and Francis, (2005).

[2] J. A. Alonso, Structure and Properties of Atomic Nanoclusters, 2nd Edition, Imperial College Press (2012).

[3] S. Sugano, Microcluster Physics, 1st Edition, Springer-Verlag, (1991).

[4] Q. Zhang, E. Uchaker, S. L. Candelaria, G. Cao, Nanomaterials for energy conversion and storage, Chem. Soc. Rev., Vol. 42, Iss. 7, p. 3127-3171, (2013).

[5] P. W. Atkins, General Chemistry, 5th edition, Scientific American Books, (1989).

[6] C. Kittel, Introduction to Solid State Physics, 7th edition, John Wiley and Sons, Inc., (1996).

[7] H. Haberland, Clusters of atoms and molecules: Theory, Experiments, and Clusters of Atoms, Springer Series in Chemical Physics, Vol. 52, Springer-Verlag, (1994).

[8] B. Bagchi, Water in Biological and Chemical Processes: From Structure and Dynamics to Function, Cambridge University Press, (2013).

[9] G. E. Douberly, R. S. Walters, J. Cui, K. D. Jordan, M. A. Duncan, Infrared Spectroscopy of Small Protonated Water Clusters, $H^+(H_2O)_n, (n = 2-5)$: Isomers, Argon Tagging and Deuteration, J. Phys. Chem. A, Vol. 114, No. 13, pp. 4570-4579, (2010).

[10] G. Rayner-Canham, T. Overton, Descriptive Inorganic Chemistry, W. H. Freeman and Company New York, 5th edition, (2010).

[11] R. D. Thomas et al., The effect of bonding on the fragmentation of small systems, J. Phys.: Conf. Ser. 4 , p. 187-190, (2005).

[12] P. W. Atkins, R. S. Friedman, Molecular Quantum Mechanics, 5th edition, Oxford University Press, (2011).

[13] K. C. Molloy, Group theory for chemists: fundamental theory and applications, Woodhead Publishing, 2nd edition, (2011).

[14] P. Atkins, J. de Paula, J. Keeler, Physical Chemistry, 8th edition, W. H. Freeman and Company, (2006).

[15] R. A. Buckingham, The Classical Equation of State of Gaseus Helium, Neon and Argon, Proceedings of the Royal Society of London, Series A, Mathematical and Physical Sciences, Vol. 168, No. 933, pp. 264-283, (1938).

[16] A. R. Leach, Molecular Modelling: Principles and Applications, 2nd edition, Prentice Hall ,(2001).

[17] C. Y. Ng, D. J. Trevor, B. H. Mahan, Y. T. Lee, Photoionization Study of the Xe2 van der Waals Molecule, J. Chem. Phys., Vol. 65, pp. 4327-4329, (1976).

[18] Pang Xiao Feng, Water Molecular Structure and Properties, World Scientific Publishing Co. Pte. Ldt., (2014).

[19] A. Mukhopadhyay, S. S. Xantheas, R. J. Saykally, The water dimer II: Theoretical investigations, Chemical Physics Letters, Vol. 700, pp. 163-175, (2018).

[20] M. W. Feyereisen Hydrogen Bond Energy of the Water Dimer, J- Phys. Chem, Vol. 100, p. 2993-2997, (1996).

[21] A. Mukhopadhyay, W. T.S. Cole, R. J. Saykally, The water dimer I: Experimental characterization, Chemical Physics Letters, 633, p. 13–26, (2015).

[22] V. N. Popok, Polymer-Based Multifunctional Nanocomposites and Their Applications, Elsevier Science, Chapter 2, p. 35-76, (2019).

[23] C. Bobbert, S. Schütte, C Stainbach, U. Buck, Fragmentation and reliable size distributions of large ammonia and water clusters, Eur. Phys. J. D, Vol. 19, pp. 183-192, (2002).

[24] O. Echt, K. Sattler, E. Recknagel, Magic Numbers for Sphere Packings: Experimental Verification in Free Xenon Clusters, Phys. Rev. Lett., Vol. 47, No. 16, pp. 1121-1124, (1981).

[25] I. A. Harris, R. S. Kidwell, J. A. Northby, Sructure of Charged Argon Clusters Formed in a Free Jet Expansion, Physical Reviw Letters, Vol. 53, No. 25, pp. 2390-2392, (1984).

[26] C. Amano, M. Komuro, Interatomic potential and the sructure of rare gas clusters, Journal of Molecular Structure, Vol. 758, pp. 41-48, (2006).

[27] R. Ludwig, Protonated water clusters: The Third Dimension, ChemPhysChem, Vol. 5, Iss.10, pp. 1495-1497, (2004).

[28] Don L. Bunker, Mechanics of Atomic Recombination Reactions, The Journal of Chemical Physics, Vol. 32, Iss. 4, (1960).

[29] A. A. Turkin, M. V. Dutka, Y. T. Pei, D. I. Vainchtein, J. Th. M. de Hosson, On the evolution of nanocluster size distribution in a nanocluster aggregation source, Journal of Applied Physics, Vol. 111, No. 12, (2012).

[30] U. Buck, R. Krohne, Cluster size determination from diffractive He atom scattering, J. Chem. Phys., Vol. 105, Iss. 13, pp. 5408-5415, (1996).

[31] O. F. Hagena, Condensation in free jets: Comparison of rare gases and metals, Z. Phys. D, Vol. 4, Iss. 3, pp. 291-299, (1987).

[32] O. F. Hagena, Nucleation and growth of clusters in expanding nozzle flows, Surf. Sci., Vol. 106, Iss. 1-3, pp. 101-116, (1981).

[33] C. Dass, Fundamentals of contemporary mass spectrometry, A John Wiley and Sons, Inc., (2007).

[34] T. D. Märk, G. H. Dunn, Electron Impact Ionization; Partial Ionization Cross Sections, 1st edition, Springer-Verlag Wien GmbH, (1985).

[35] Shen, V.K., Siderius, D.W., Krekelberg, W.P., and Hatch, H.W., Eds., NIST Standard Reference Simulation Website, NIST Standard Reference Database Number 173, National Institute of Standards and Technology, Gaithersburg MD, 20899, http://doi.org/10.18434/T4M88Q, (16.06.2021).

[36] P. Willmott, An Introduction to Synchrotron Radiation: Techniques and Applications, John Wiley and Sons, (2011).

[37] D. Bonhommeau, N. Halberstadt, A. Viel, Fragmentation dynamics of argon clusters ($Ar_n, n = 2to11$) following electron-impact ionization: Modelling and comparison with experiment, J. Chem. Phys., Vol. 124, Iss. 18, 184314, (2006).

[38] E. de Hoffmann, J. Charette, V. Stroobant, Mass Spectrometry: principles and applications, John Wiley and Sons, (1996).

[39] U. Becker, D. A. Shirley, VUV and Soft X-Ray Photoionization, Springer Science and Business Media, (1996).

[40] SPECS GmbH - Surface Analysis and Computer Technology, User's manual, Electron source EQ 22/35, Version 1.0, (2004).

[41] SPECS GmbH - Surface Analysis and Computer Technology, User's manual, Power Unit EQ 22/25, Version 1.3, (2008).

[42] W. C. Wiley and I. H. McLaren, Time of flight mass spectrometer with improved resolution, Review of scientific instruments, Vol. 26, No. 12, (1955).

[43] E. Pelimanni, Characterization of an HDA-TOFMS electron-ion coincidence spectrometer, Nano and Molecular Systems Materials Research Unit, University of Oulu, (2017).

[44] MCP Delay Line Detector Manual, RoentDek, (Version 9.22.1003.1).

[45] WebElements™, http://www.webelements.com/, (16.06.2021).

[46] A. N. Arseniev et al., Xenon clusters fragmentation in a supersonic beam under ionization by electrons and photons, J. Phys.: Conf. Ser., 1038, (2018).

[47] X. Llovet, C. J. Powell, F. Salvat, A. Jablonski, Cross Sections for Inner-Shell Ionization by Electron Impact, Journal of Physical and Chemical Reference Data, Vol. 43, (2014).

[48] M. Gisselbrecht et al., Size dependent fragmentation of argon clusters in the soft x-ray ionization regime, J. Chem. Phys., Vol. 128, No. 4, (2008).

[49] Z. Yang, S. Hua, W. Hua, S. Li, Low-Lying Structures and Stabilities of Large Water Clusters: Investigation Based on the Combination of the AMOEBA Potential and Generalized Energy-Based Fragmentation Approach, J. Phys. Chem., Vol. 114, pp. 9253–9261, (2010).

[50] E. P. Parker, J.V.Ortiz, Electron propagator calculations on the discrete spectra of ArH and NeH, Chemical Physics Letters, Vol. 163, Iss. 4-5, pp. 366-370, (1989).

[51] K. Suhara, A. Fujii, K. Mizuse, N. Mikami, J. Kuo, Compatibility between methanol and water in the three-dimensional cage formation of large-sized protonated methanol-water mixed clusters, J. Chem. Phys., Vol. 126, Iss. 19, (2007).